

Jm

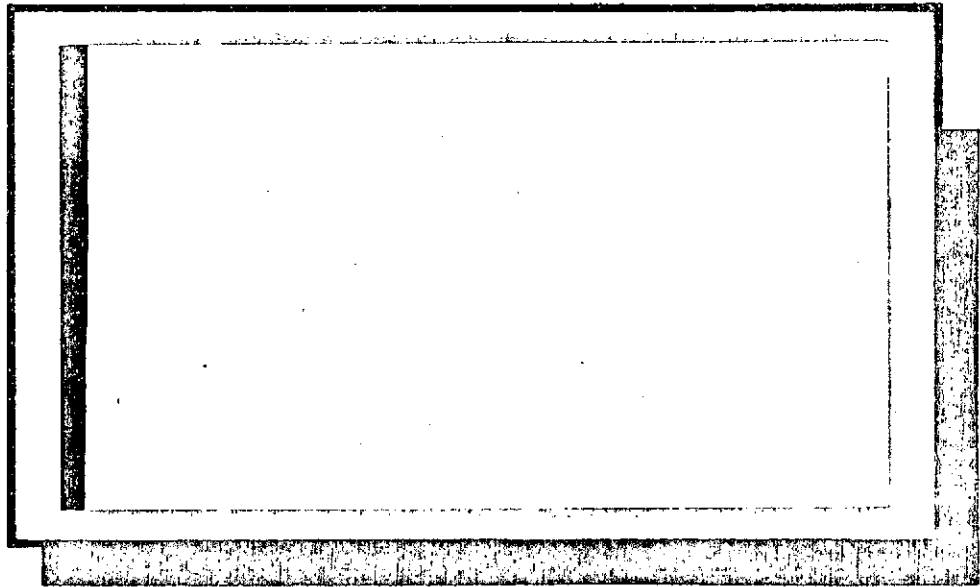
NASA CR-

141724

13
18

(NASA-CR-141724) SURFACE ELECTRICAL PROPERTIES EXPERIMENT Final Report (Massachusetts Inst. of Tech.) 178 p HC \$7.00	N75-21192
C S C L 0 3 B	Unclass 18043

G3/91



CENTER FOR SPACE RESEARCH
 MASSACHUSETTS INSTITUTE OF TECHNOLOGY



Final Report
on the
SURFACE ELECTRICAL PROPERTIES EXPERIMENT
NASA Contract NAS^{g-}_λ-11540

CSR TR-74-1

March 15, 1974

FINAL REPORT
ON
THE SURFACE ELECTRICAL PROPERTIES EXPERIMENT

Contract # NAS-⁹⁻₁11540

To: Johnson Space Center
National Aeronautics and Space Administration
Houston, Texas 77058

From: Center for Space Research
and
Department of Earth and Planetary Sciences
Massachusetts Institute of Technology
Cambridge, Massachusetts 02139


Gene Simmons
Principal Investigator

15 March 1974.

TABLE OF CONTENTS

	Page
SUMMARY	iii
1. Electrical structure at Taurus-Littrow	1-1
2. The Surface Electrical Properties Experiment	2-1
3. Electromagnetic fields due to dipole antennas over stratified anisotropic media	3-1
4. Radio interferometry depth sounding: Part I-Theoretical discussion	4-1
5. Radio interferometry depth sounding: Part II-Experimental results	5-1
6. Interference patterns of a horizontal electric dipole over layered dielectric media	6-1
7. Electromagnetic probing of the Moon	7-1
8. Geophysical subsurface probing with radio-frequency interferometry	8-1
9. Numerical evaluation of electromagnetic field due to dipole antennas in the presence of stratified media	9-1
10. The electromagnetic response of a low-loss, 2 layer, dielectric earth for horizontal electric dipole excitation	10-1
11. Detection of thin layers by radio interferometry	11-1

SUMMARY

The Surface Electrical Properties Experiment (SEP) was flown to the Moon in December 1972 on Apollo 17 and used to explore a portion of the Taurus-Littrow region. SEP used a relatively new technique, termed Radio Frequency Interferometry (RFI). Electromagnetic waves were radiated from two orthogonal, horizontal electric dipole antennas on the surface of the Moon at frequencies of 1, 2, 4, 8, 16, and 32 Mhz.

The field strength of the EM waves was measured as a function of distance with a receiver mounted on the Lunar Roving Vehicle and using three orthogonal, electrically small, loops. The interference pattern produced by the waves that travelled above the Moon's surface and those that travelled below the surface was recorded on magnetic tape. The tape was returned to Earth for analysis and interpretation.

Data were obtained during EVA 2 on the traverse from the SEP-site (near the landing point) towards Station 2 for a distance of about 2 1/2 km. Unfortunately, data were not obtained during the remainder of EVA 2 because the SEP receiver overheated. Neither were data obtained during EVA 3 because a switch was placed in the standby-position rather than the on-position for the early portion of the EVA and the SEP receiver then overheated. Thus our analysis of the electrical structure of the Taurus-Littrow site is restricted to the vicinity of the traverse from the SEP-site to Station 2.

Because the lower frequency waves penetrate deeper into the Moon than the higher frequency waves, we use the 1 MHz interference pattern to infer the electrical properties at depth. We use the 32MHz pattern to estimate the properties near the surface. In one model, the relative dielectric constant increases from a value of $3 \frac{1}{2}$ near the surface to a value of about 6 - 7 at a depth of 100m and then decreases slightly. In another model, a near-surface, sloping interface between material of slightly differing dielectric constant satisfies some of the constraints imposed by the observed data. We have not yet obtained any model that satisfies most of the constraints provided by the large quantity of data for the lunar traverse.

Despite the lack of a model that does satisfy most of the observed data, we believe that the gross electrical features of the Taurus-Littrow site are these: (1) the relative dielectric constant increases with depth (from about $3 \frac{1}{2}$ at the surface to 6 - 7 at depth), (2) the dielectric constant is rather constant over the depth interval of 100 meters to at least $2 \frac{1}{2}$ km, (3) the loss tangent is no larger than 0.05 and possibly as small as 0.002, (4) no significant quantity of water is present within $2 \frac{1}{2}$ km of the Moon's surface at Taurus-Littrow, (5) electromagnetic scattering at frequencies of 1 - 32 MHz is absent at Taurus-Littrow which implies that subsurface "boulders" of dimensions in the range of 10 - 300m and with contrasting dielectric constant, are not present

within 1 - 2 km of the surface.

In this final report, we include several reprints, pre-prints, and an initial draft of the first publication of the SEP results. These documents provide a rather complete account of the details of the theory of the RFI technique, of the terrestrial tests of the technique, and of the present state of our interpretation of the Apollo 17 data.

ELECTRICAL STRUCTURE AT TAURUS-LITTROW

This section is a preliminary draft of the initial manuscript to be submitted to any scientific journal describing the SEP experiment and the scientific results obtained from the experiment. This initial draft, prepared by Strangway, Annan, Redman, Rossiter and Watts, will be modified before submission to a journal. The list and sequence of authors' names have not yet been determined.

(REVISED)

Introduction

The Surface Electrical Properties (SEP) Experiment was flown to the Taurus-Littrow region of the moon on Apollo 17. The experiment used megahertz radio frequencies in order to determine (i) electrical layering at the landing site, (ii) the dielectric properties of the surface material in situ, and (iii) the presence of scattering bodies.

In order to sound into the surface layers a relatively new technique, called radio frequency interferometry (RFI), had been developed for the lunar experiment and had been tested extensively on earth. A transmitter was set out on the lunar surface and a receiver was carried on the Lunar Roving Vehicle. As the Rover moved along its traverse, the received magnetic field strength and the Rover's position with respect to the transmitter were recorded.

At any point on the traverse several waves reach the receiver, and these waves interfere, as shown in Figure 1. The interference pattern is diagnostic both of the physical properties and of the structure of the upper layers. Field strength data for six frequencies and six combinations of receiving and transmitting antenna orientation, along with position, calibration, and temperature information, were recorded on a magnetic tape which was returned to earth.

The basis for the interferometry concept and details of the SEP Experiment have been given elsewhere (Annan, 1973; Rossiter et al., 1973; Simmons et al., 1972; Kong, Tsang, and Simmons, 1974; the SEP Team, 1974). In the present paper we

will outline briefly the basis for our interpretation, present the lunar SEP data, and describe our most recent evaluation of the results.

Background Material

Because radio interferometry is a relatively new technique, most of our background experience with it was built up explicitly for the lunar experiment. This study had three main facets: (i) theoretical evaluation of the EM fields surrounding a dipole antenna over a dielectric medium; (ii) experimental work using an analogue scale model; and, (iii) field work on several different glaciers for full scale experiments.

Although the integral expressions for the EM fields surrounding a dipole over a half-space have been known for some time (e.g. Banõs, 1966), their evaluation for layered media with completely general electrical properties is far from trivial. Straight numerical integration is prohibitively expensive (Tsang, Brown, Kong, and Simmons, 1974). Therefore three complementary approximate methods were used - a geometric optics approach, the theory of normal modes and fast Fourier transform (FFT) techniques. The geometric optics formulation (Annan, 1970, 1973; Kong, 1972; Tsang et al., 1973) is most accurate for "optically thick" layers, and becomes invalid for distances less than about a wavelength. Theoretical cures are most easily calculated with the normal mode formulation for thin layers in which only a few modes propagate. The use of the FFT technique (Tsang, Brown, Kong, and Simmons, 1974) allows us

to calculate theoretical interference patterns for models in which the electrical properties vary continuously with depth.

In order to check these calculations, and to be able to study cases too complex for theoretical treatment, a scale model was constructed in which we used microwave frequencies (Waller, 1973; Annan et al., 1974). The model consisted of a layer of dielectric oil in which a reflecting plate could be set up in many different orientations. A typical suite of model curves for the layered case of a dielectric over a perfect reflector is shown in Figure 2, along with the corresponding theoretical curves. The inaccuracy of the geometric optics solution for thin layers is readily apparent.

Field experience with the RFI technique was gained on trips to the Gorner and Athabasca Glaciers (Rossiter et al., 1973; Strangway et al., 1974), and to the Juneau Icefields, using lunar hardware at various stages of development. Because most of the glaciers were known, from independent work, to approximate plane layered media, we were able to match observed data with curves obtained from the geometric optics formulation for layered media. In the analysis of the glacier field data, we compared, by trial-and-error suites of theoretical curves with field data. Attempts at formal inversion are currently underway (Watts, 1974).

A typical set of field profiles for the glacier tests and their corresponding "best-fit" theoretical curves are shown in Figure 3. No single frequency or component was uniquely indicative of the parameters (dielectric constant, loss tangent,

and depth to reflector). However, if we accepting only parameter sets that give consistent, good (but not perfect) fits for all frequencies, and for both of the maximum-coupled components for which we have theoretical solutions, then we can always find an "acceptable" interpretation.

SEP Operational History

The SEP experiment was done at the Apollo 17 Taurus-Littrow landing site. The transmitting dipole antennas were deployed by the astronaut about 150 meters east of the Lunar Module in a north-south and in an east-west direction (see Figure 4). During EVA-II SEP data are recorded as the Rover moved in a westerly direction away from the SEP transmitter towards Station #2. The traverse as reconstructed from the SEP-LRV navigation data is given in Figure 5.

From the SEP transmitter out to a range of 1.7 km the receiver operated normally. Between the range of 1.7 km and 4.3 km the receiver operated in an acquisition mode, attempting to acquire a synchronization signal from the transmitter. In this mode only partial data is collected. At a range of 4.3 km, because of the low received field strength, the receiver obtained a false resynchronizing pulse, causing an incorrect realignment of the receiver and transmitter timing, and a subsequent loss of field strength data from that point. At Station #2 the receiver was turned off to aid in cooling. The receiver was operating again between Stations #4 and #5; however,

the signal levels were too low to allow a resynchronization with the transmitter. At the beginning of the Station #5 stop the receiver was turned off, and, although the receiver was turned on again at the end of the station stop, because the internal receiver temperature was above a safe limit a thermal switch prevented it from operating for the remainder of EVA-II.

Data were to have been recorded during EVA-III from the SEP transmitter to Station #6 but the astronauts failed to turn on the receiver. Therefore, the data which are used as a basis for this discussion are those taken from the SEP transmitter west to a range of 4.3 km.

SEP Data and Discussion

The configuration of the SEP transmitting and receiving antennas is shown in Figure 6. Electromagnetic waves of six frequencies, 1, 2, 4, 8, 16 and 32 MHz, are transmitted sequentially by two orthogonal horizontal dipole antennas and received by three orthogonal selectrically small, loop antennas, resulting in 36 readings of the field strength during each measurement cycle.

Positional information from the Rover navigation system is recorded as increments and decrements of 1° in bearing, and 100 m in range, and as odometer pulses, each equivalent to a .49 meter change in position for the right-front and left-rear wheels of the Rover.

The Rover traverse derived from SEP data is compared in Table 1 with traverse data produced by the U.S.G.S. (ALGIT, 1974) and with the traverse reconstruction created from the Goddard Very Long Baseline Interferometry Data (I. Salzberg, personal communication, January 1974). The VLBI data have an absolute accuracy of approximately 40 m. The U.S.G.S. traverse is taken from photographic pans made at station stops, and are accurate to approximately 10 m for EP-4, LRV-1, and Station 2, and to about 50 m for LRV-2 and 3.

The three traverses are plotted in Figure 7. The maximum differences are about 500 m at stops LRV-2 and 3. The differences between USGS and VLBI traverses are larger than expected, and later adjustments of the data may improve the agreement among the three sets. For the first 2 km, all three reconstructions are in good agreement.

TABLE 1. COMPARISON OF EVA-II TRAVERSE STOPS FROM USGS, VLBI and SEP-LRV NAVIGATION DATA (See Figure 7).

STATION	RANGE (Km)			BEARING		
	VLBI	USGS	SEP-LRV NAV DATA	VLBI	USGS	SEP-LRV NAV DATA
EP-4	.500	.538	.508	80.4	80	83
LRV-1	2.603	2.603	2.645	80.9	78	82
LRV-2	3.750	3.729	3.811	81.4	86	83
LRV-3	4.248	4.253	4.325	80.2	87	82
HOLE IN THE WALL	5.638		5.683	79.5		81
STN. #2		7.46	7.6		68	71

A set of SEP field strength data is shown in Figure 8. Each

plot contains either the endfire or the broadside components for one frequency, plotted as a function of range, in free-space wavelengths. The data are plotted for a maximum distance of 1.7 km or to 20 free-space wavelengths.

For each frequency, six components are measured. Three components - H_{ϕ} endfire, and H_{θ} and H_z broadside are maximum-coupled for a plane layered geometry, while the other three are minimum-coupled to the transmitted signal. For all six frequencies the maximum-coupled components have an average level from 5 to 15 dB greater than the minimum-coupled components. These results are in direct contrast to our glacial observations. For all our glacier runs the max and min components were approximately equal in level at 16 and 32 MHz (Strangway, et al., 1974). We attributed this rough equality of signal level to the presence of random scatterers (e.g. crevasses) in the ice with dimensions on the order of a wavelength. On this basis then, infer that few scattering bodies are present in the subsurface near the lunar SEP site, with typical sizes of 10 to 300 m and contrasting dielectric properties. Scattering experiments both in the scale model and on glaciers support this conclusion.

Further confirmation is obtained, by an examination of the H_{ϕ} endfire component. This component has a near-surface wave so large that it effectively masks any interference. However, if near-surface scattering is important, this component becomes erratic. As can be seen from Figure 8, this component is relatively smooth at all SEP frequencies. The residual peaks and

nulls correlate well with those in the H_p -broadside component. Therefore we believe that these two components are slightly mixed because the traverse was not completely east-west (i.e. not directly off the end of the endfire antenna).

The other two maximum-coupled components (H_p and H_z broadside) have been the most important for interpretation (see Figure 9). At 16 and 32 MHz the number of peaks and troughs per free space wavelength of range is fairly low, indicating a dielectric constant of about 2 to 5. However, the lower frequencies show somewhat higher beating rates, indicating a dielectric constant of about 6 to 8, and certainly less than 10. These observations imply that the dielectric constant of the near-surface material is lower than that of deeper material. These results are consistent with the dielectric properties of a soil layer over solid rock, as measured on returned samples (e.g. Olhoeft et al., 1973).

The loss tangent is estimated from the sharpness of the peaks and nulls in the two major components and from the average decay of the field strength with distance. Our analysis indicates that the average loss tangent of the sub-surface material to a depth of several hundred meters is less than 0.05 and possibly as low as 0.002. The fact that the higher frequencies have strong signal levels for many tens of wavelengths from the transmitter, while the lower frequencies die out relatively quickly, indicates that the loss tangent of the near surface material is 0.01 or less. These low loss values confirm that no liquid water is present in the outer kilometer of the moon.

Structure is more difficult to determine unambiguously. By comparing the two major components with suites of theoretical curves for a plane two-layer geometry (i.e. dielectric layer over a dielectric half-space), no single set of parameters has been found that gives theoretical curves in satisfactory agreement with the data at all frequencies. Several perturbations from the two-layer model have therefore been suggested.

One possible variation is sketched in Figure 10 (a), showing a thinning layer of soil over rock. The layer is 20 m thick near the SEP site, with dielectric constant of 3 to 4, and thins to 15 m a few hundred meters to the west. The lower material has a dielectric constant of 6 to 7. Results from the Lunar Seismic Profiling Experiment, conducted over the same region, show good agreement with this model (Watkins and Kovach, 1973). The chief basis for this interpretation is the curve for 2 MHz broadside (Figure 9 (b)), which shows little interference out to about 4 wavelengths range, but then has several dramatic peaks. This behaviour suggests that the layer is just thick enough near the transmitter that little energy is transmitted either through the layer or through the subsurface. However, further from the transmitter the layer becomes so thin that it is essentially transparent. Although we have not obtained theoretical formulations for sloping interfaces, we have observed interference patterns for sloping glacier

interfaces and for the microwave model that resemble the lunar pattern.

Table 2 lists the parameters of a three-layer model, sketched in Figure 10 (b). In this model we assume, (i) that layer 1 is so thin that it is essentially transparent to all frequencies but 16 and 32 MHz; and, (ii) that the boundary between layers 2 and 3 is too deep to have much effect on the 16 and 32 MHz patterns. Theoretical curves for this model are shown for comparison with the data in Figure 9. Although the major features of the data are present also in the theoretical curves, the details are not always in good agreement. This lack of agreement may be due to slight adjustments in loss tangent (the particular features in most curves are very dependent on the loss tangent), or due to slight dipping of the interfaces (as mentioned above).

TABLE 2. PARAMETERS FOR 3-LAYER MODEL

(See Figures 9 and 10(b)).

	<u>Depth (m)</u>	<u>Dielectric constant</u>	<u>Loss tangent</u>
Layer 1	7 ± 1	3.8 ± 0.2	0.008 ± 0.004
Layer 2	100 ± 10	7.5 ± 0.5	0.035 ± 0.025
Layer 3	00	9 ?	?

Another model that fits reasonably well, the observed data is shown in Figure 11 and several theoretical curves, obtained with the FFT formulation of Tsang, Brown, Kong and Simmons (1974) are shown in Figure 12.

Conclusions

Despite our present inability to match the lunar SEP observations with the theoretical curves calculated for various models, we believe that the gross electrical properties of the Taurus-Littrow region have been obtained. At the present stage of our analysis of the lunar data, we are confident of the following conclusions:

- (1) The loss tangent of the lunar material in situ is less than 0.05 and possibly as low as 0.002, to depths of 2 to 3 kilometers.
- (2) No liquid water is present at Taurus-Littrow to a depth of 2 to 3 kilometers.
- (3) Electromagnetic scattering is not important at any of the SEP frequencies.
- (4) Scattering bodies with sizes of 10 to 300 meters are not present in the vicinity of the traverse from the SEP-site to Station 2.
- (5) The relative dielectric constant is about 3 1/2 near the surface and increases with depth to a value of 6 to 8 at about 100 meters. These values are consistent with the values expected for lunar soil overlying rock.
- (6) No model consisting of plane layers has been found that fits the observations accurately. Some features of a thinning layer, a three-layer model and continuously increasing dielectric properties match some of the features of the observed interference patterns.

(7) The Rover navigation data recorded on EVA II to Station
2 is in good agreement with VLBI and USGS traverse reconstructions.

PRECEDING PAGE BLANK NOT FILMED

Acknowledgements

Financial support was provided by the National Aeronautics and Space Administration through Contract NAS -11540 with sub-contract to University of Toronto. The lunar hardware was built by Raytheon. Technical and administrative support was provided by the Center for Space Research and the C. S. Draper Laboratory.

We thank Mssrs. J. Proctor and J. Rylaarsdam for computational and data processing assistance. Mr. G. Wagner designed and built the data reduction systems. Much of the data reduction was carried out at the Johnson Space Center and at the Lunar Science Institute, Houston, Texas.

References

- Annan, A.P., "Radio Interferometry Depth Sounding", M. Sc. thesis, Dept. of Physics, U. Of Toronto, 1970.
- Annan, A.P., "Radio Interferometry Depth Sounding"; Part I - Theoretical Discussion", Geophysics, v. 38, pp. 557-580, 1973.
- Annan, A.P., Waller, W.M., Strangway, D.W., Rossiter, J.R., and Redman, J.D., "The Electromagnetic Response of a Two-Layer Dielectric Earth Excited by a Horizontal Electric Dipole", submitted to Geophysics, 1974.
- Apollo Lunar Geology Investigation Team, (U.S.G.S.), "Preliminary Geological Analysis of the Apollo 17 Site", Apollo 17 Preliminary Science Report, 1974.
- Baños, A., "Dipole Radiation in the Presence of a Conducting Half-space", Pergamon Press, New York, 1966.
- Kong, J.A., "Electromagnetic Fields due to Dipole Antennas over Stratified Anisotropic Media", Geophysics, v. 37, pp. 985-996, 1972.
- Olhoeft, G. R., Strangway, D.W., and Frisillo, A.L., "Lunar Sample Electrical Properties", Proc. Fourth Lunar Sci. Conf., (Suppl. 4, Geochim. Cosmochim. Acta), v. 3, pp. 3133-3149, 1973.
- Rossiter, J.R., LaTorraca, G.A., Annan, A.P., Strangway, D.W., and Simmons, G., "Radio Interferometry Depth Sounding; Part II - Experimental Results", Geophysics, v. 38, pp. 581-599, 1973

- Rossiter, J.R., Strangway, D.W., Annan, A.P., Watts, R.D., and Redman, J.D., "Detection of Thin Layers by Radio Interferometry", submitted to Geophysics, 1974.
- Simmons, G., Strangway, D.W., Bannister, L., Baker, R., Cubley, D., LaTorraca, G., and Watts, R., "The Surface Electrical Properties Experiment", in Kopal, Z. and Strangway, D., eds., Lunar Geophysics, Proceedings of a Conference at the Lunar Science Institute, Houston, Texas, 18-21 October, 1971, D. Reidel, Dordrecht, pp. 258-271, 1972.
- Strangway, D.W., Simmons, Gene, LaTorraca, G., Watts, R., Bannister, L., Baker, R., Redman, D., and Rossiter, J., "Radio-Frequency Interferometry - A New Technique for studying Glaciers", J. Glaciology, in press, 1974.
- Surface Electrical Properties Team, "The Surface Electrical Properties Experiment", Apollo 17 Preliminary Science Report, in press, 1974.
- Tsang, L., Kong, J.A., and Simmons, G., "Interference Patterns of a Horizontal Electric Dipole over Layered Dielectric Media", J. Geophys. Res., v. 78, pp. 3287-3300, 1973.
- Waller, W. M., "Surface Electrical Properties Simulation Model", Lockheed Electronics Co. Final Report LEC/PESD 634-TR-139 for contract NAS 9-122200, NASA-JSC, Houston, 1973.
- Watkins, J.S., and Kovach, R.L., "Seismic Investigation of the Lunar Regolith", Proc. Fourth Lunar Sci. Conf. (Suppl. 4, Geochim. Cosmochim. Acta), v. 3, pp. 2561-2574, 1973

Watts, R.D., "Line-Source Radiation over a Layered Dielectric:
Inversion of Radio Interferometry Data", J. Geophys. Res.,
in press, 1974.

Figure Captions

Fig. 1. The three main waves used in radio interferometry. The surface wave travels above the surface of the dielectric and the subsurface wave travels just below it. Because these two waves travel at different velocities, their beat frequency is a function of the dielectric constant. Any reflected waves from a subsurface horizon also influence the interference pattern.

Fig. 2 Theoretical solutions and scale model data for a dielectric over a perfect reflector. The inaccuracy of the geometric optics approach for thin layers is readily apparent.

Fig. 3. Typical RFI data for the Athabasca Glacier and a set of theoretical curves.

Fig. 4. Photograph of the Taurus-Littrow site with superimposed information that shows the locations of traverses, major station stops, SEP transmitter site, and the explosive package (EP-4). SEP data were collected for a distance of 4 km along the traverse from SEP-site towards Station 2.

Fig. 5. Map of the EVA-II traverse, based on LRV navigation data, from the SEP site to Station 2. The Rover stops are indicated by LRV-1, -2, and -3.

Fig. 6 Notation of the field components. Three orthogonal magnetic field components are measured for each transmitting antenna. One transmitting antenna was approximately broadside to the traverse, the other was endfire to the traverse.

Fig. 7a,b,c. EVA-II traverse reconstruction as compiled from (i) LRV navigation data recorded by SEP; (ii) Goddard Very Long Baseline Interferometry; and (iii) U.S.G.S. traverse reconstruction from photographic information. The three independent reconstructions compare favorably to a distance of 3 km, although they disagree more than expected near LRV-2 and 3 (see Table 1).

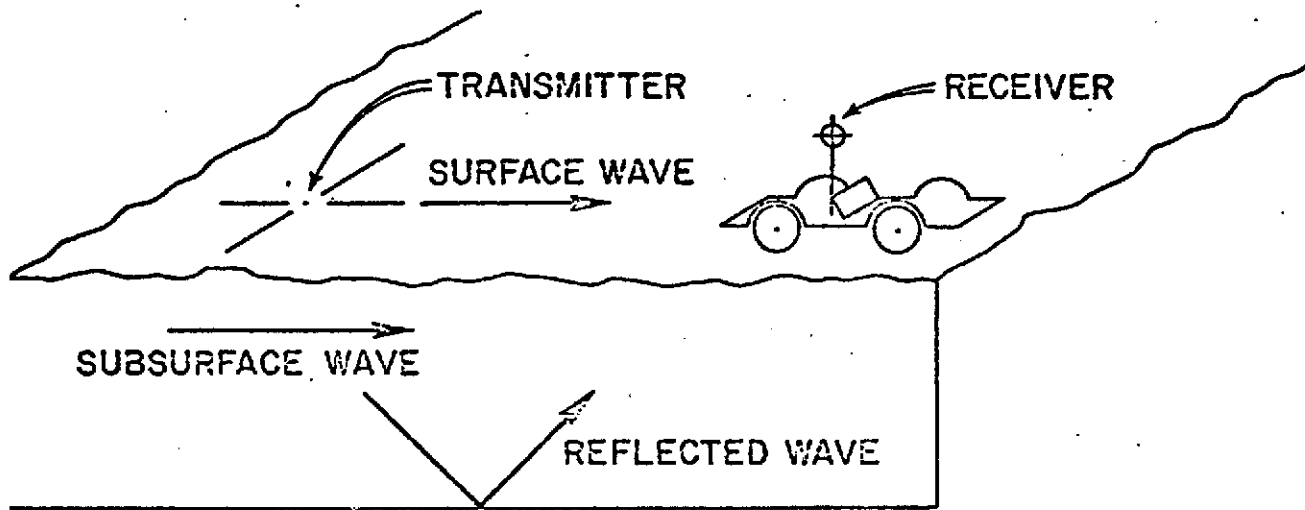
Fig. 8 (a-1). The surface Electrical Properties Experiment data for all 36 "components". Each component has been plotted as a function of free space wavelength, out to 1.7 km or 20 wavelengths (whichever is smaller). The vertical scale is in dB, with a reference at -90 dBm, as shown. The component is labelled at the end of the curve; H_ϕ endfire, H_ρ and H_z broadside are maximum coupled; the others, minimum coupled. The pattern has been corrected for a 360° turn of the Rover at the position of the EP-4 deployment.

Fig. 9 Comparison of the theoretical curves (dashed lines) with observed data (solid lines) for H_ρ and H_z broadside. The parameters for this model are given in Table 2.

Fig. 10 The model with a sloping interface.

Fig. 11 Model C11.

Fig. 12 Typical comparison of theoretical curves for Model C11
with observed data.

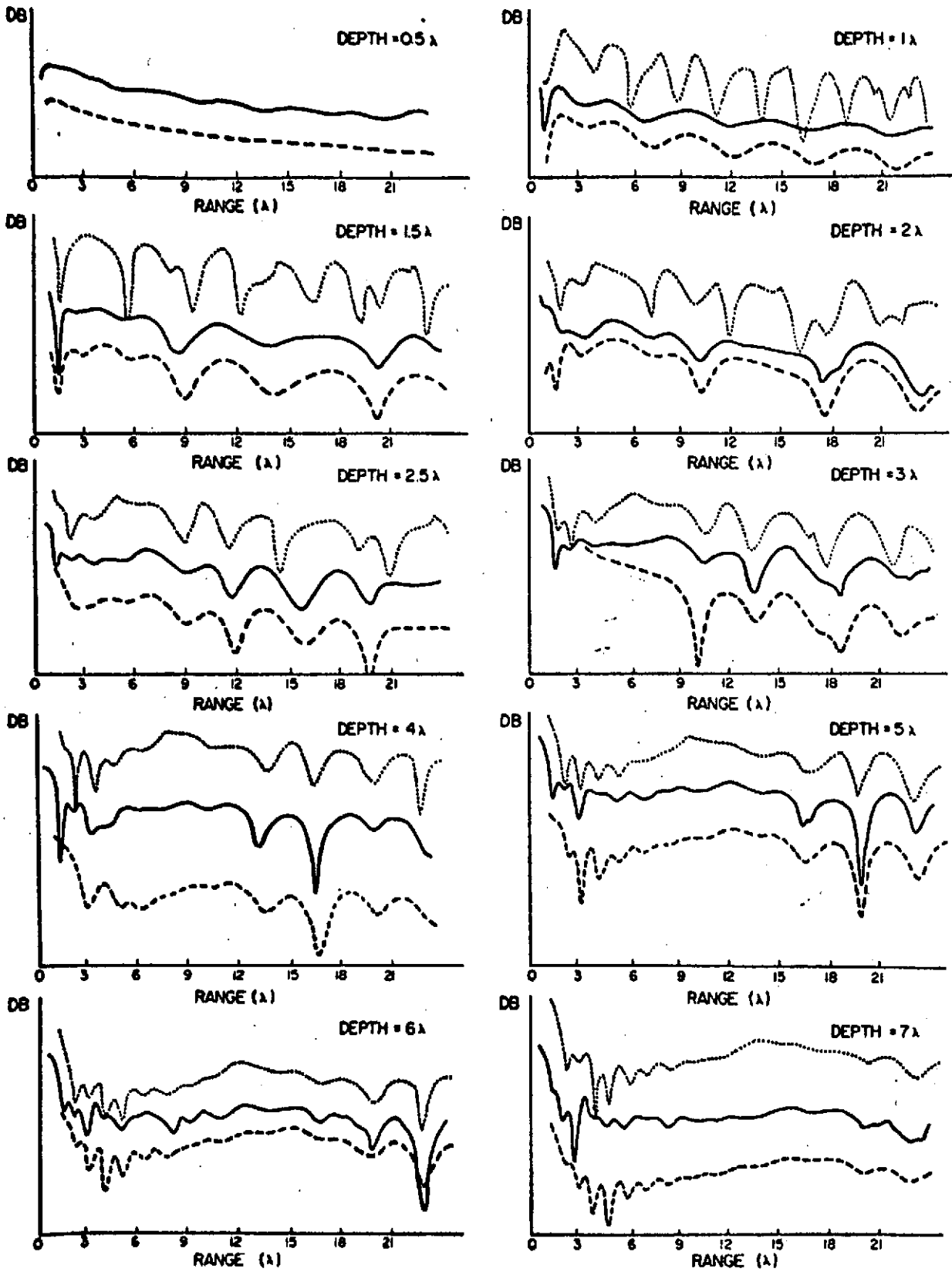


1(a)

Fig. 1.

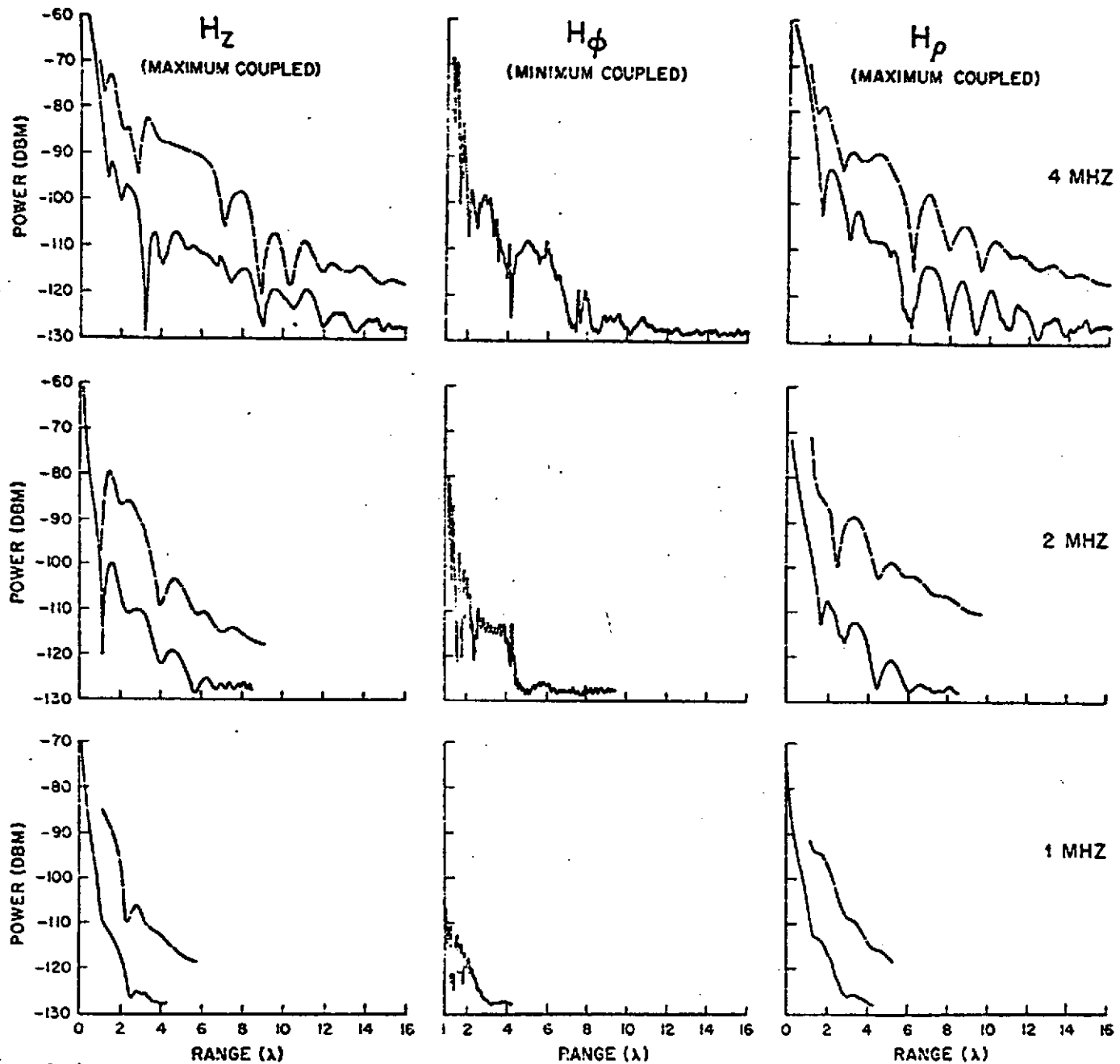
THEORETICAL SOLUTIONS AND SCALE - MODEL RESULTS
PLANE LAYERED GEOMETRY, VARIOUS DEPTHS TO REFLECTOR

Fig 2.
1-23



SCALE - MODEL ————
 THEORETICAL ······
 GEOMETRICAL OPTICS - - - -
 NORMAL MODES - - - -

$k = 2.16$
 $\tan \delta = 0.0022$



4(b)

Fig 3

APOLLO 17 LRV TRAVERSES

ORIGINAL PAGE IS
OF POOR QUALITY

42

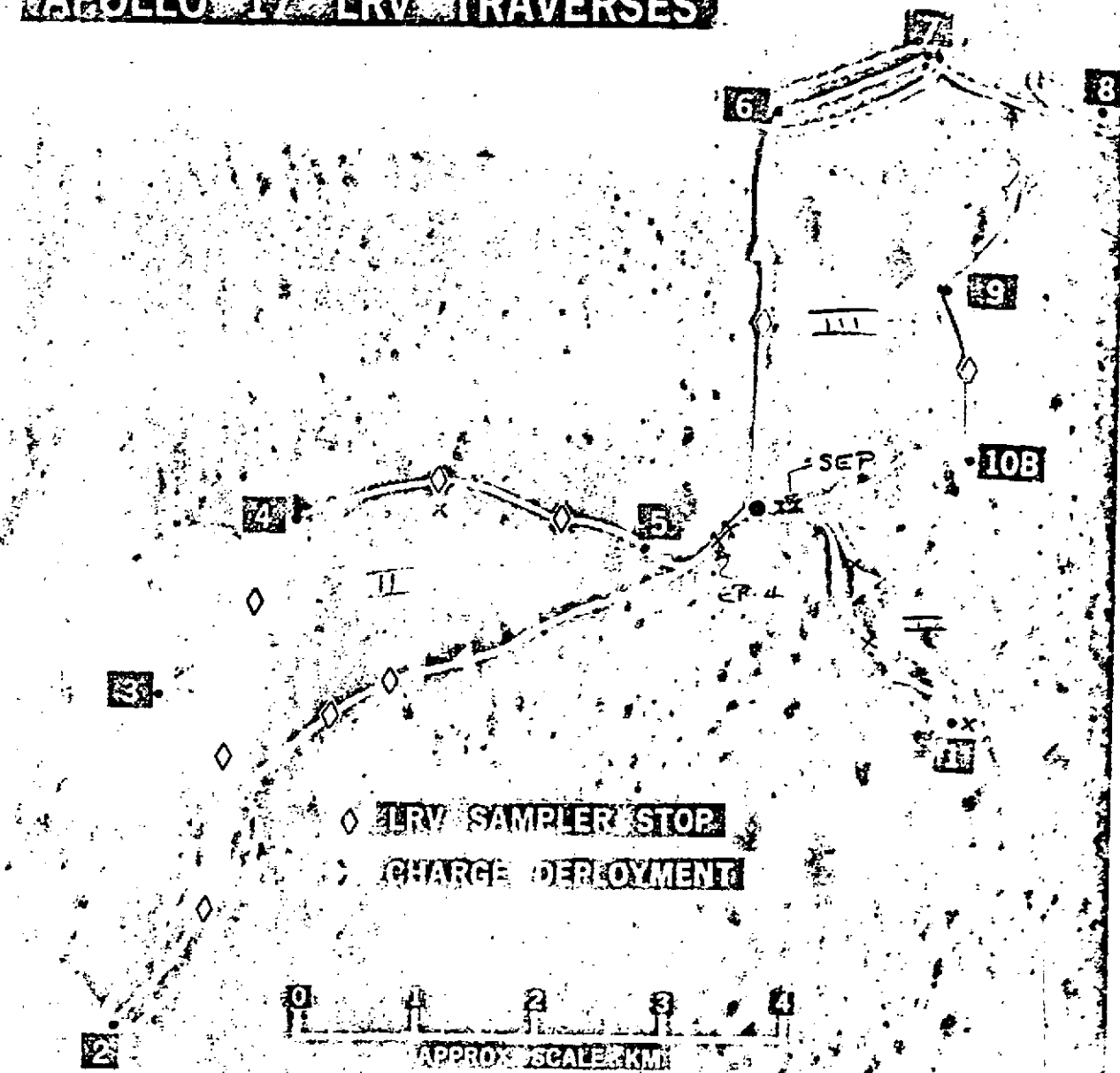


Fig-17B.- Pictorial view of the LRV traverses

Fig 4
1-25

ORIGINAL PAGE IS
OF POOR QUALITY

FIG. #3 EVA-II TRAVERSE RECONSTRUCTION FROM SEP-LRV NAVIGATION DATA

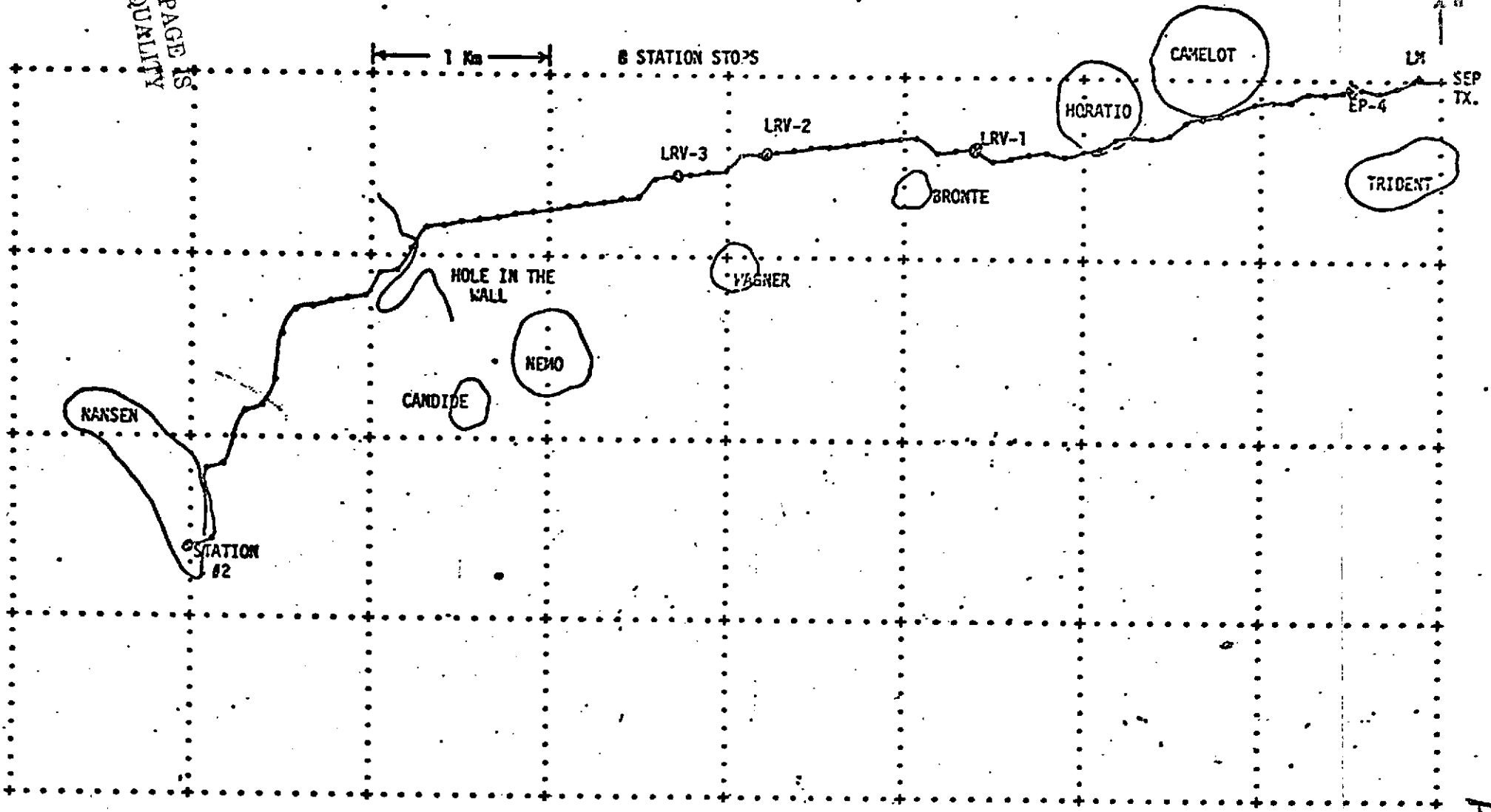
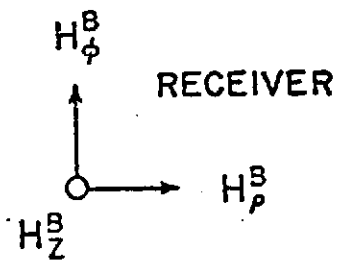


Fig. 5

BROADSIDE
ANTENNA (B)



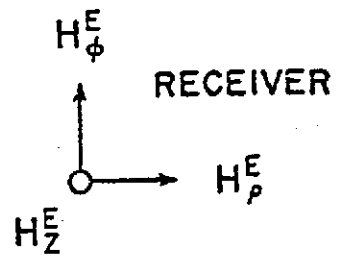
TRAVERSE



ENDFIRE
ANTENNA (E)



TRAVERSE



1(b)

ORIGINAL PAGE IS
OF POOR QUALITY

Fig. 6 1-27

FIG. #4(a) COMPARISON OF EVA-II TRAVERSE RECONSTRUCTION FROM SEP-LRV NAVIGATION DATA WITH VLBI AND USGS TRAVERSE DATA

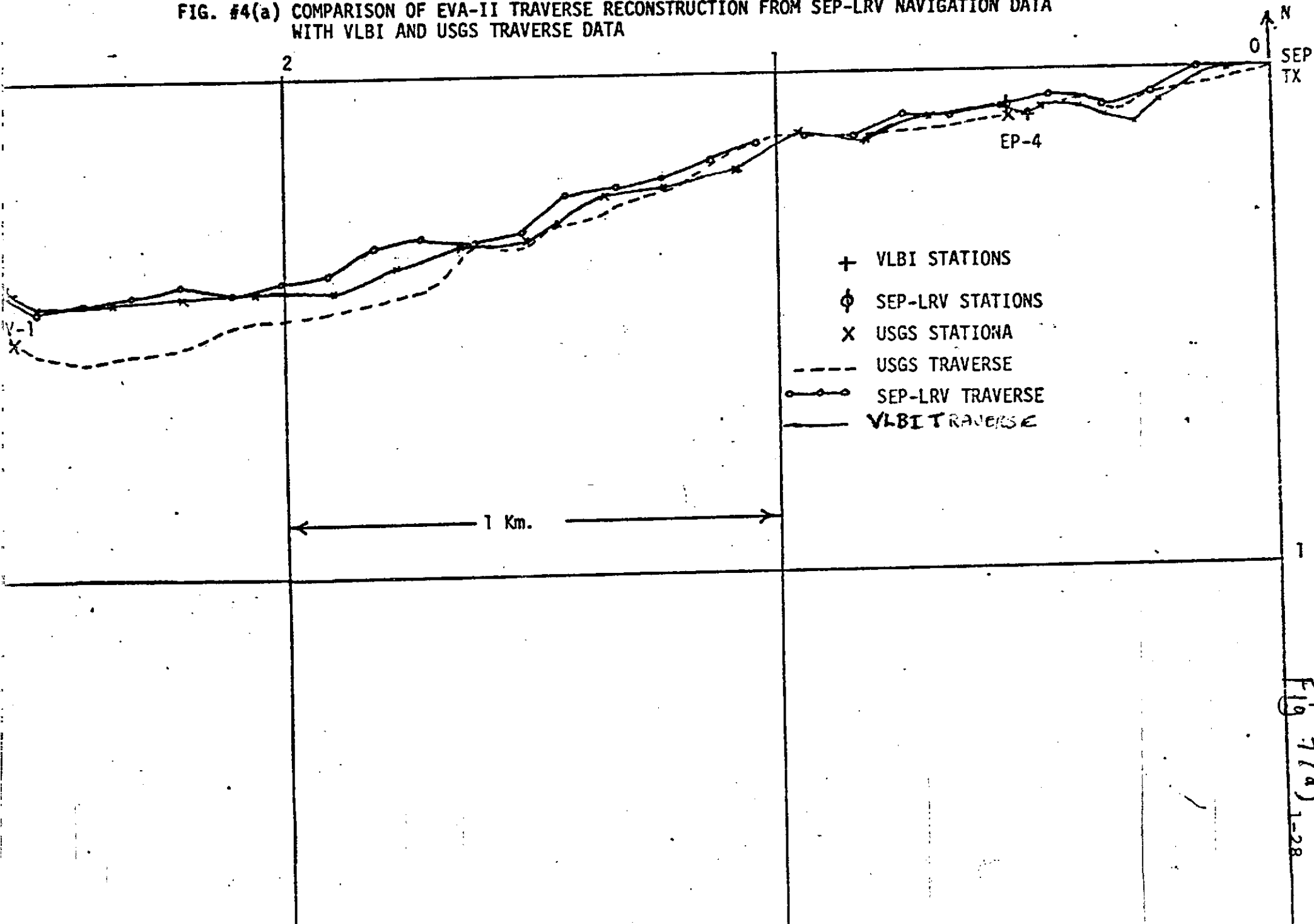


Fig. 7(a), 1-28

FIG. # 4(b)

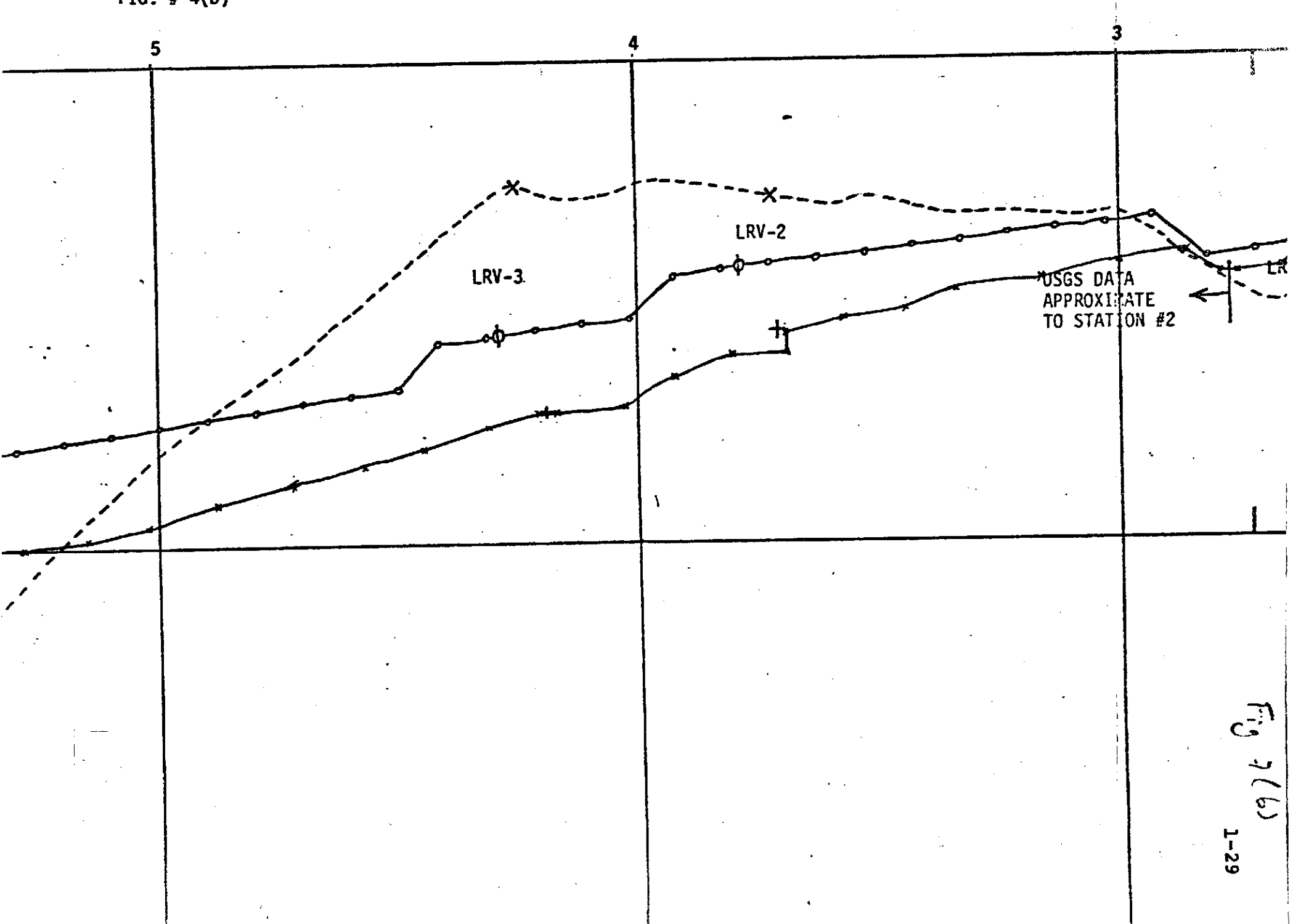
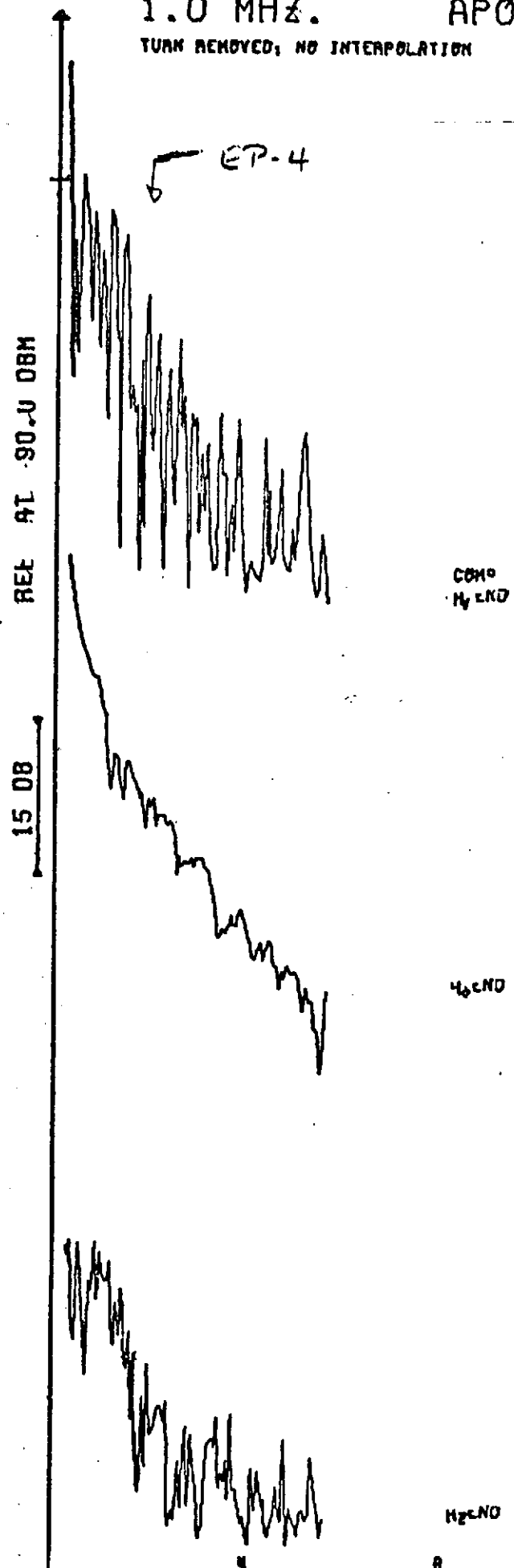


Fig 4(b)
1-29

1.0 MHz. APOLLO 17

TWAK REMOVED; NO INTERPOLATION



COMO
H2END

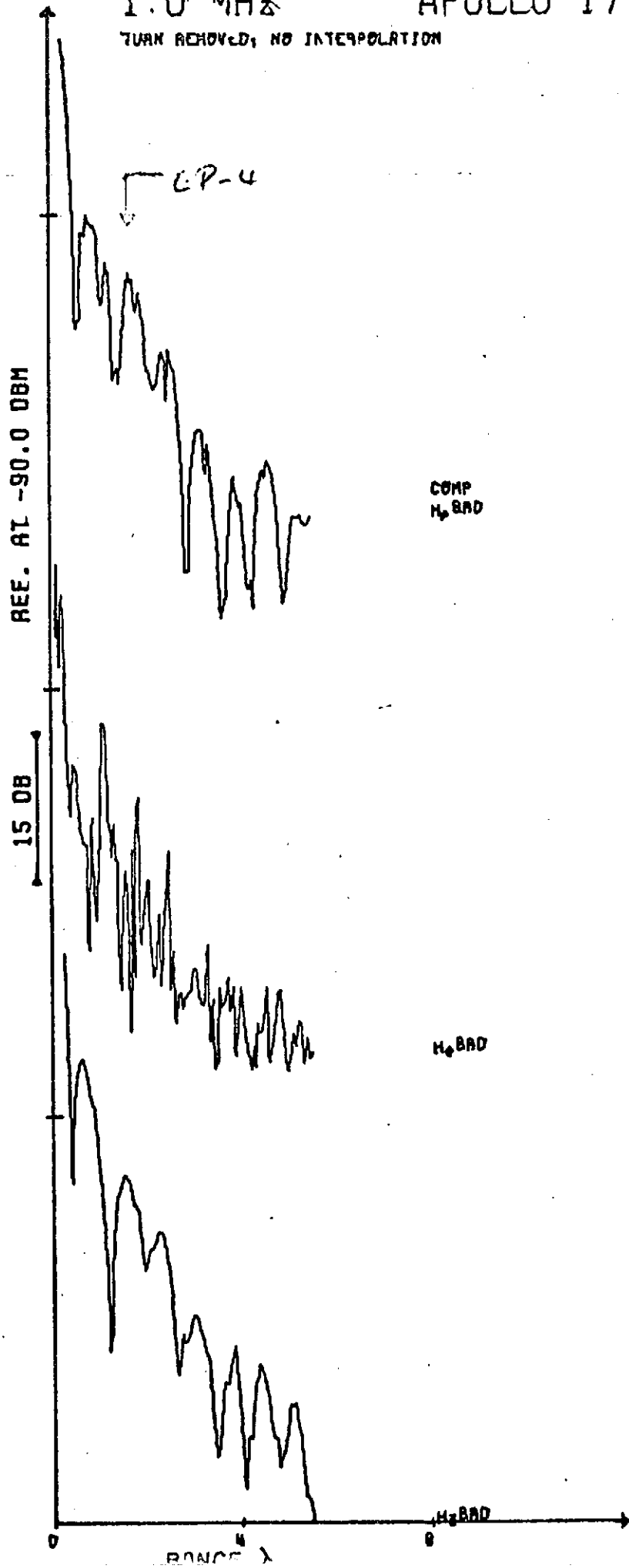
H2END

H2END

1.0 MHz

APOLLO 17

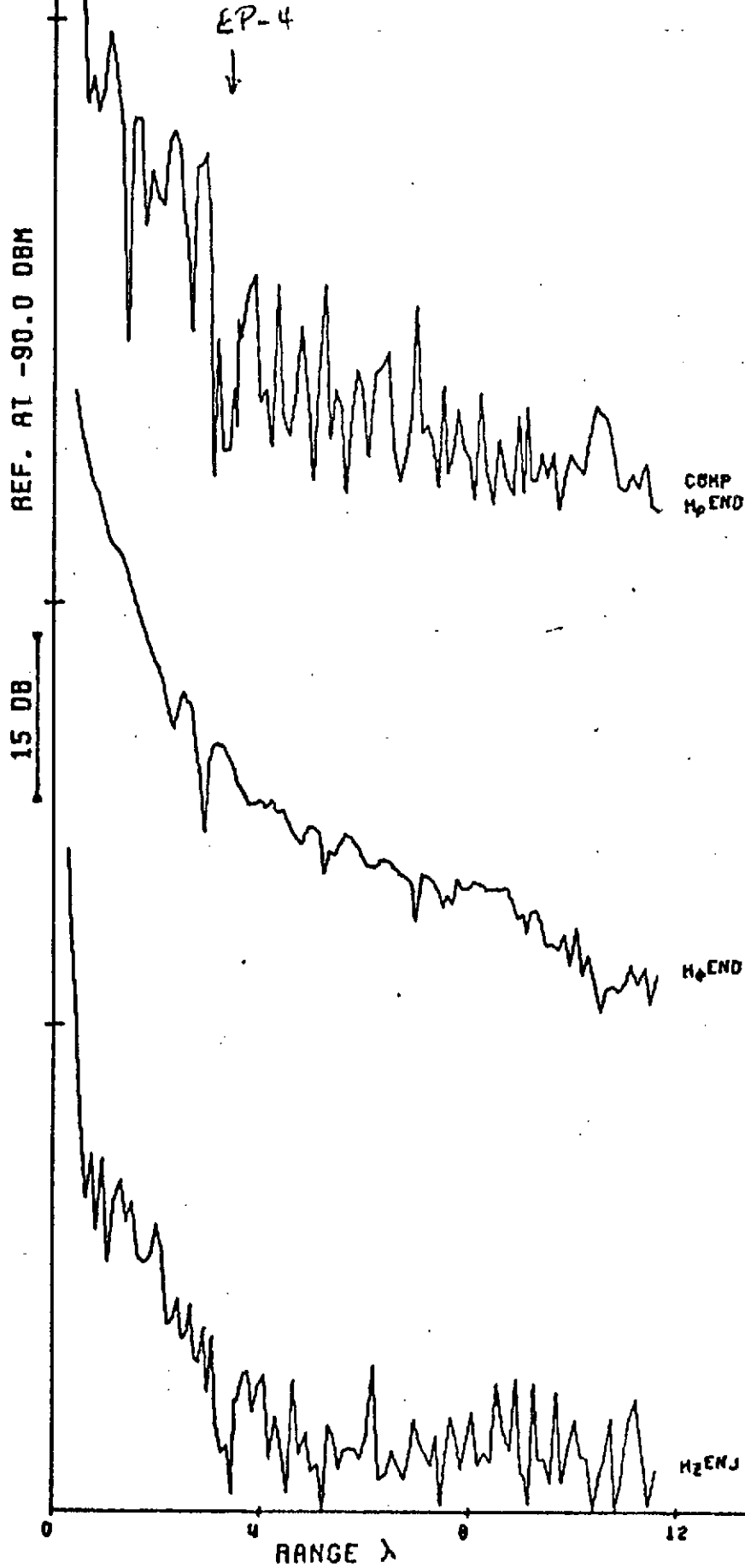
TURN REMOVED; NO INTERPOLATION



2.1 MHz. APOLLO 17

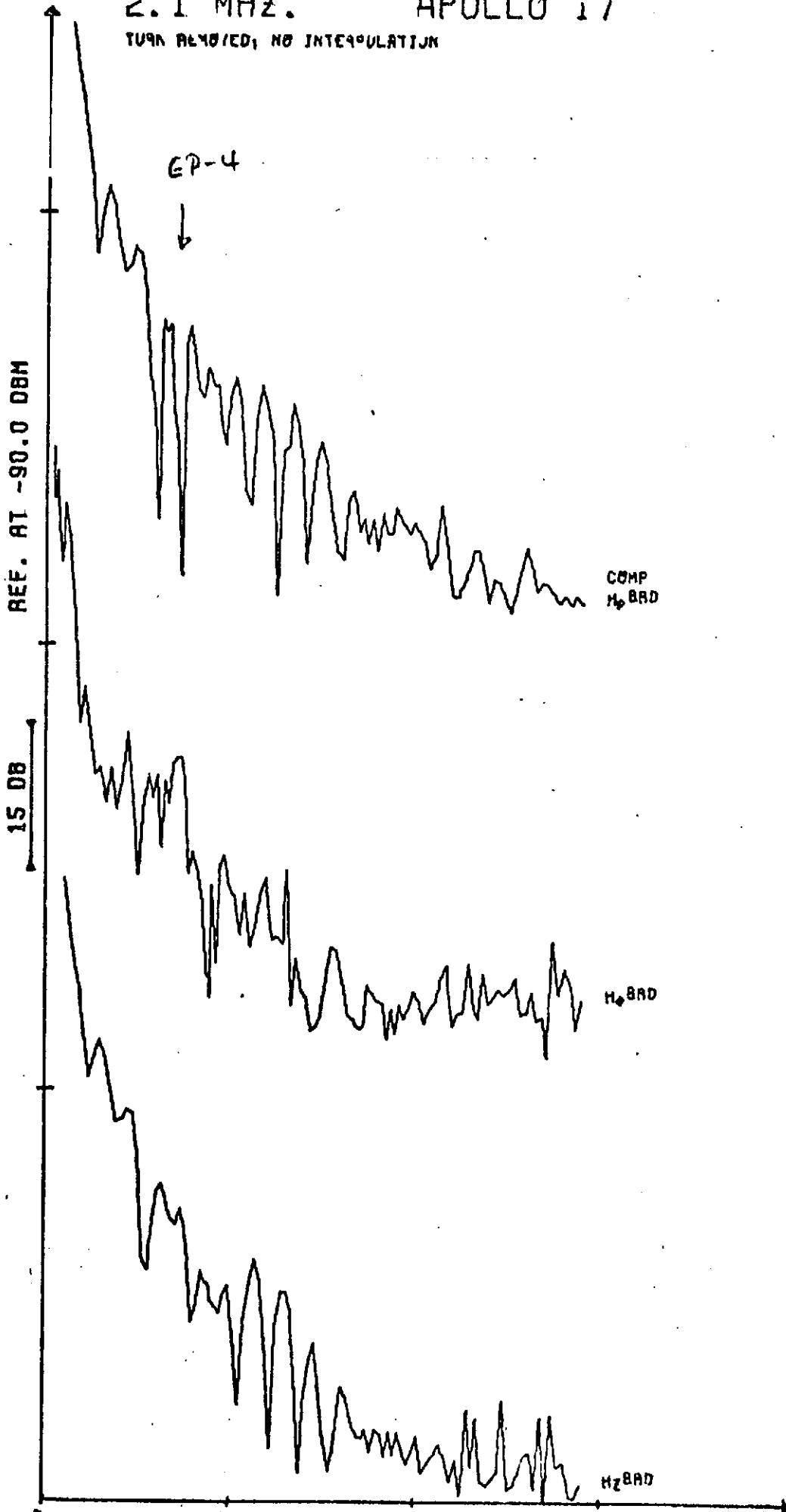
Fig 1(c) 1-33

TURN REMOVED; NO INTERPOLATION



2.1 MHZ. APOLLO 17

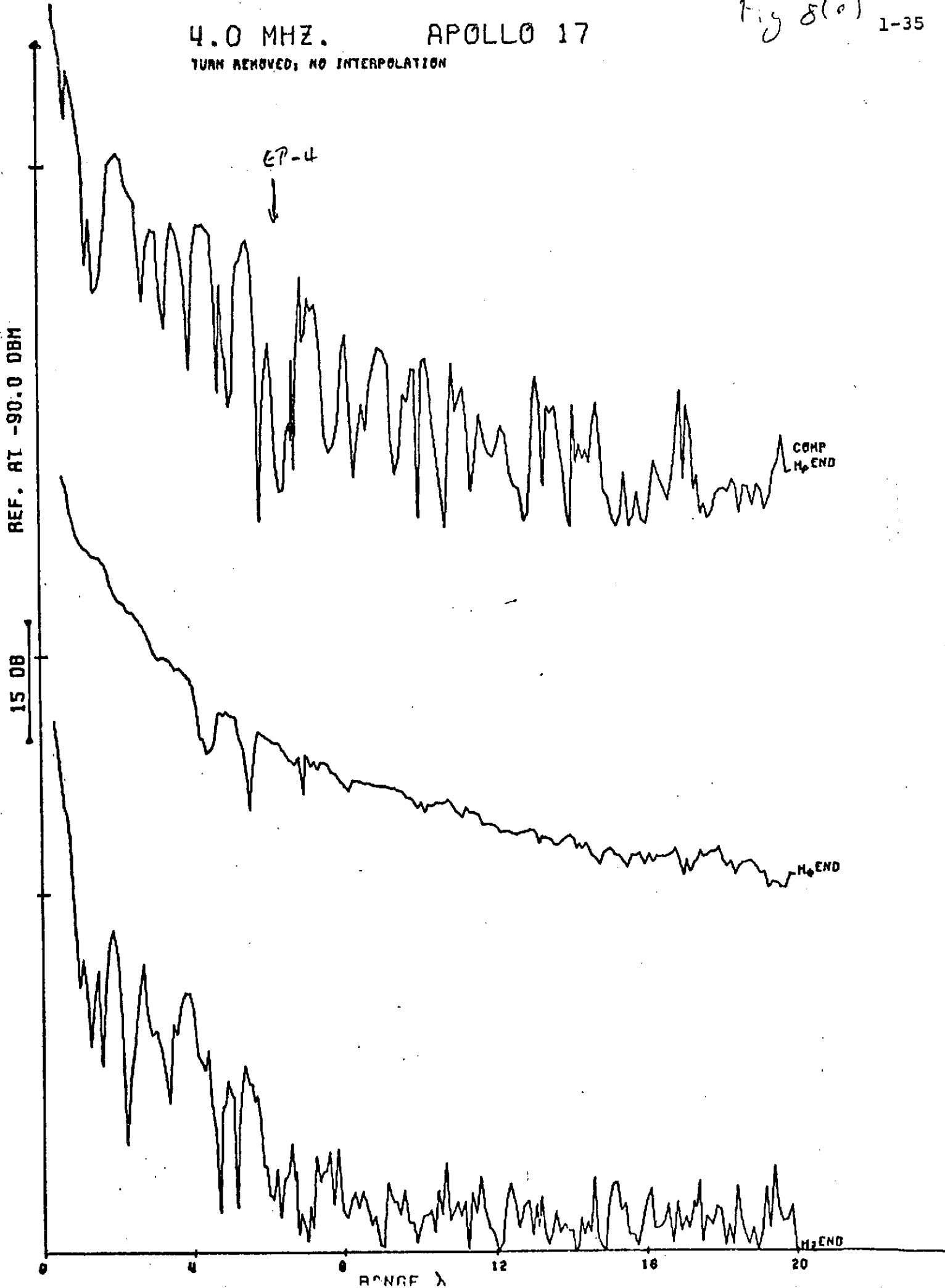
TURN REMOVED, NO INTERPOLATION



4.0 MHZ. APOLLO 17

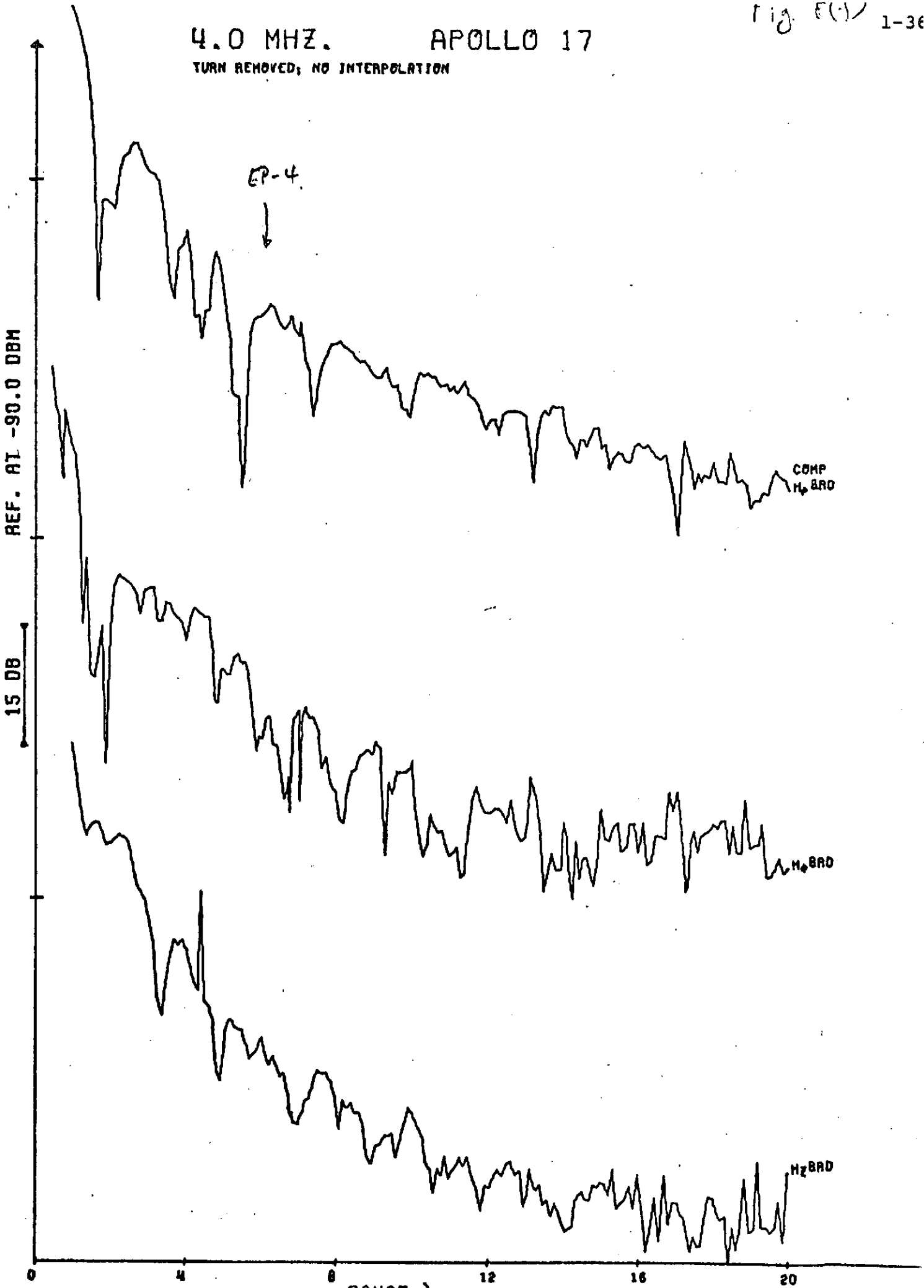
Fig 8(0) 1-35

TURN REMOVED; NO INTERPOLATION



4.0 MHZ. APOLLO 17

TURN REMOVED; NO INTERPOLATION



EP-4



COMP
H2 BRD

H2 BRD

H2 BRD

REF. AT -90.0 DBM

15 DB

RANGE

0 4 8 12 16 20

8.1 MHz.

APOLLO 17

Fig. 80

1-37

TURN REMOVED; NO INTERPOLATION

REF. AT -90.0 DBM

15 DB

EP-4



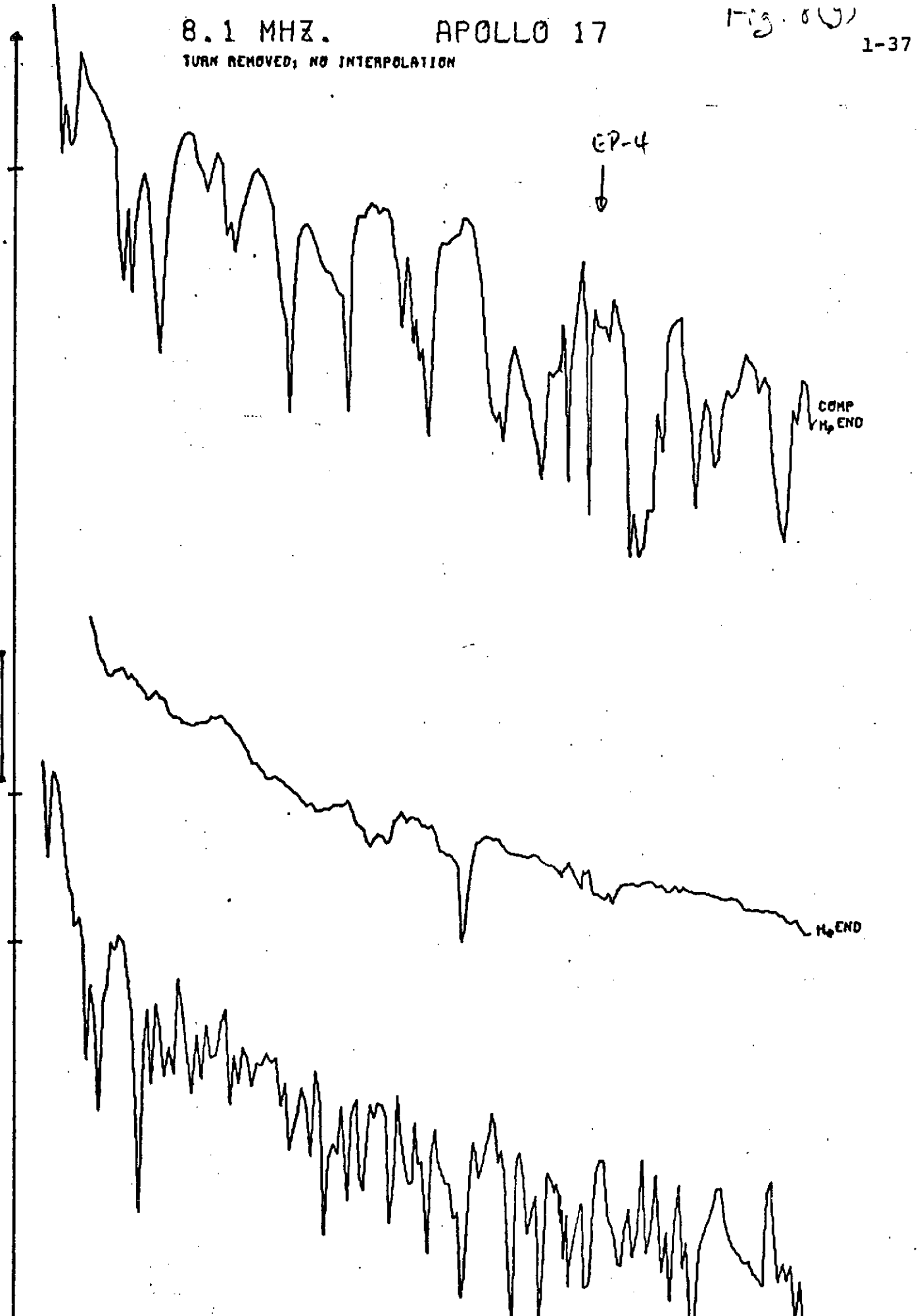
COMP
V_H END

H₂ END

H₂ END

0 4 8 12 16 20

RANGE λ



8.1 MHz. APOLLO 17

TURN REMOVED; NO INTERPOLATION

Fig 8(k)

1-38

REF. AT -90.0 DBM

15 DB

EP-4

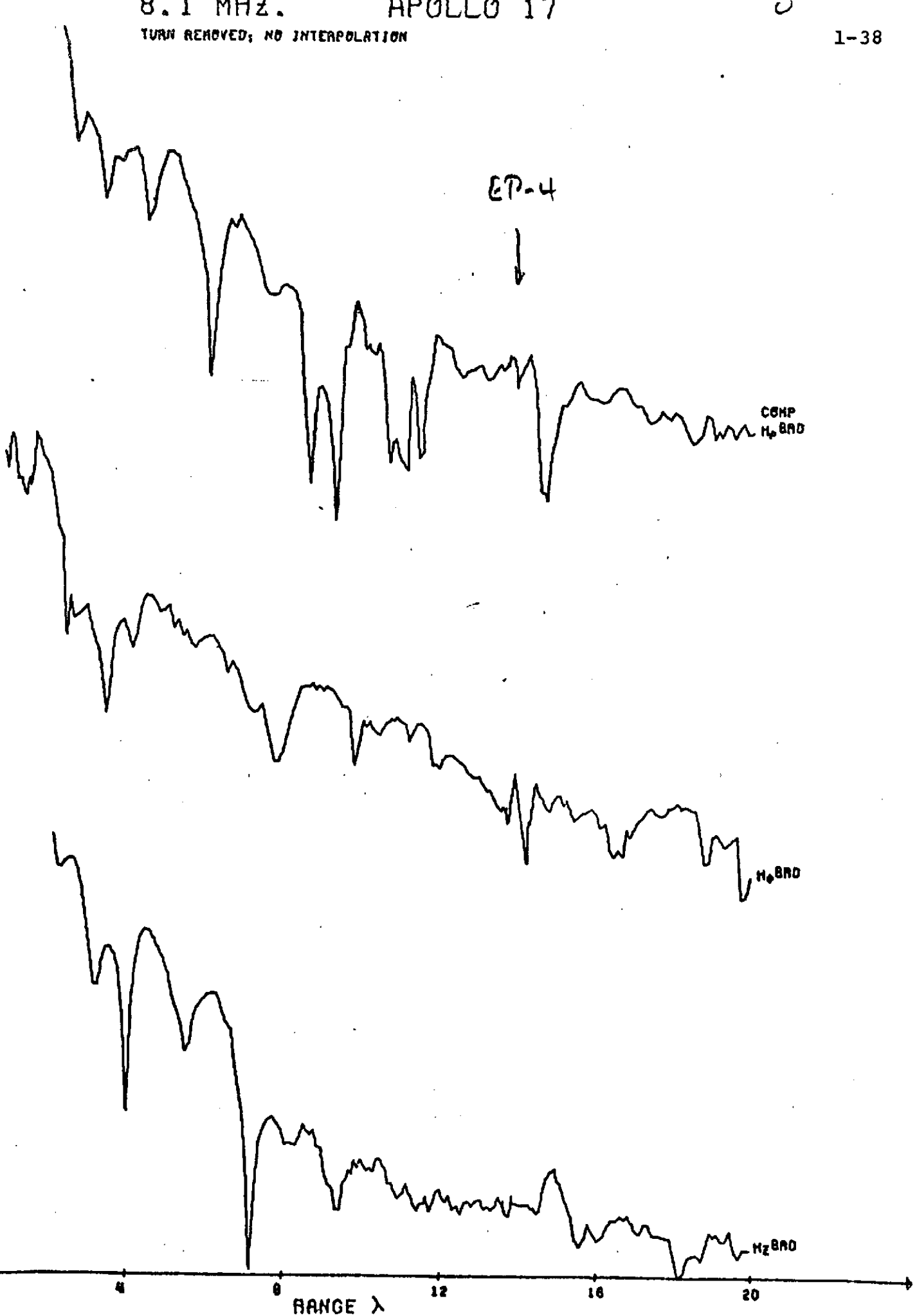
COMP
H_p BAND

H_p BAND

H_Z BAND

0 4 8 12 16 20

RANGE λ



16.0 MHZ.

APOLLO 17

Fig 8(?)

TURN REMOVED; NO INTERPOLATION

1-39

REC. AT -90.0 DBM

15 DB

COMP
Hz END

Hz END

Hz END

0

4

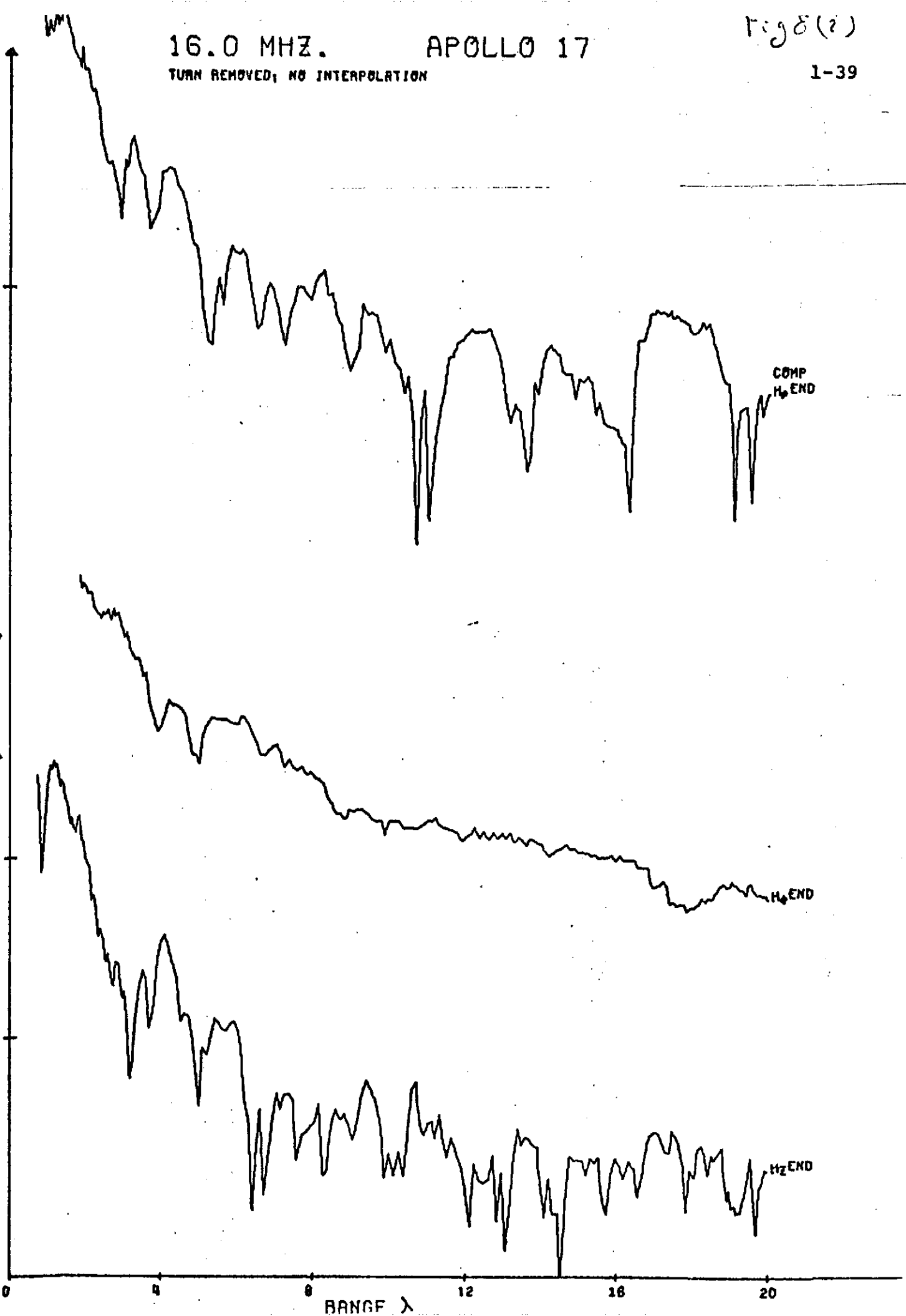
8

RANGE λ

12

16

20



16.0 MHz.

APOLLO 17

Fig. 8(J)

TURN REMOVED; NO INTERPOLATION

1-40

REF. AT -90.0 DBM

15 DB

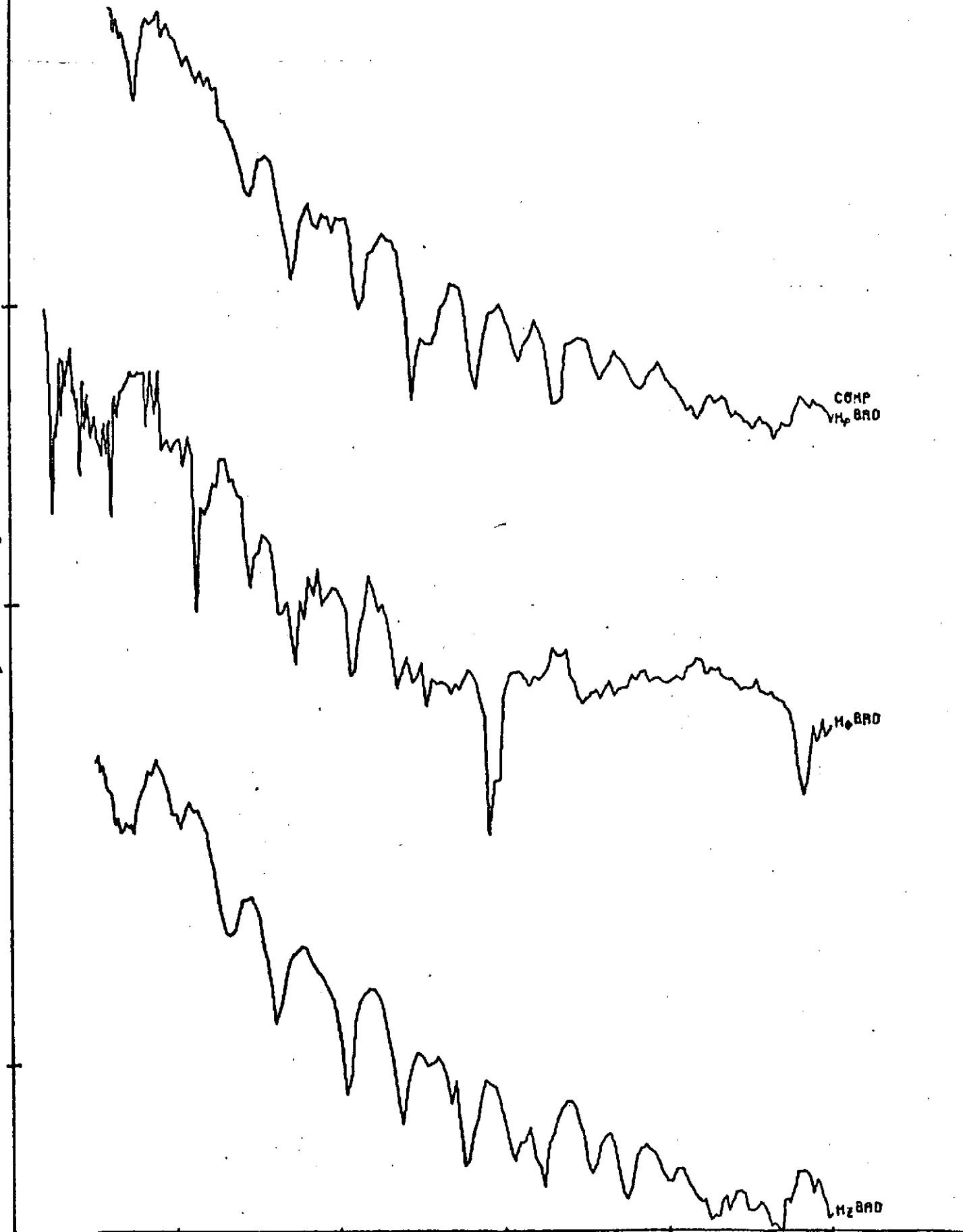
COMP
VH_p BRD

H₂ BRD

H₂ BRD

0 4 8 12 16 20

RANGE λ



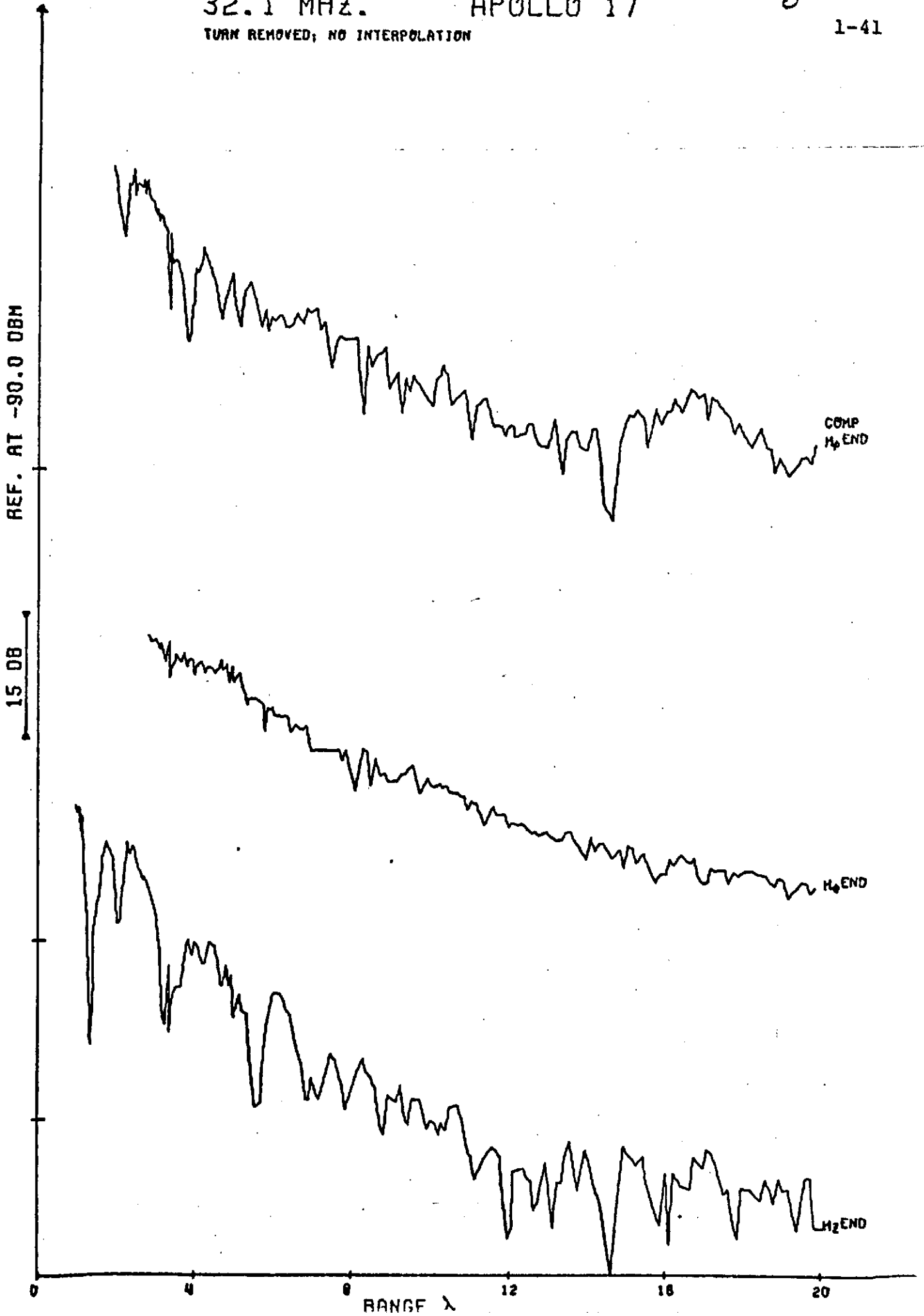
32.1 MHZ.

APOLLO 17

Fig 8 (K)

TURN REMOVED; NO INTERPOLATION

1-41



32.1 MHz.

APOLLO 17

Fig 8(a)

TURN REMOVED; NO INTERPOLATION

1-42

URN U.N. - 14 234

AN CT

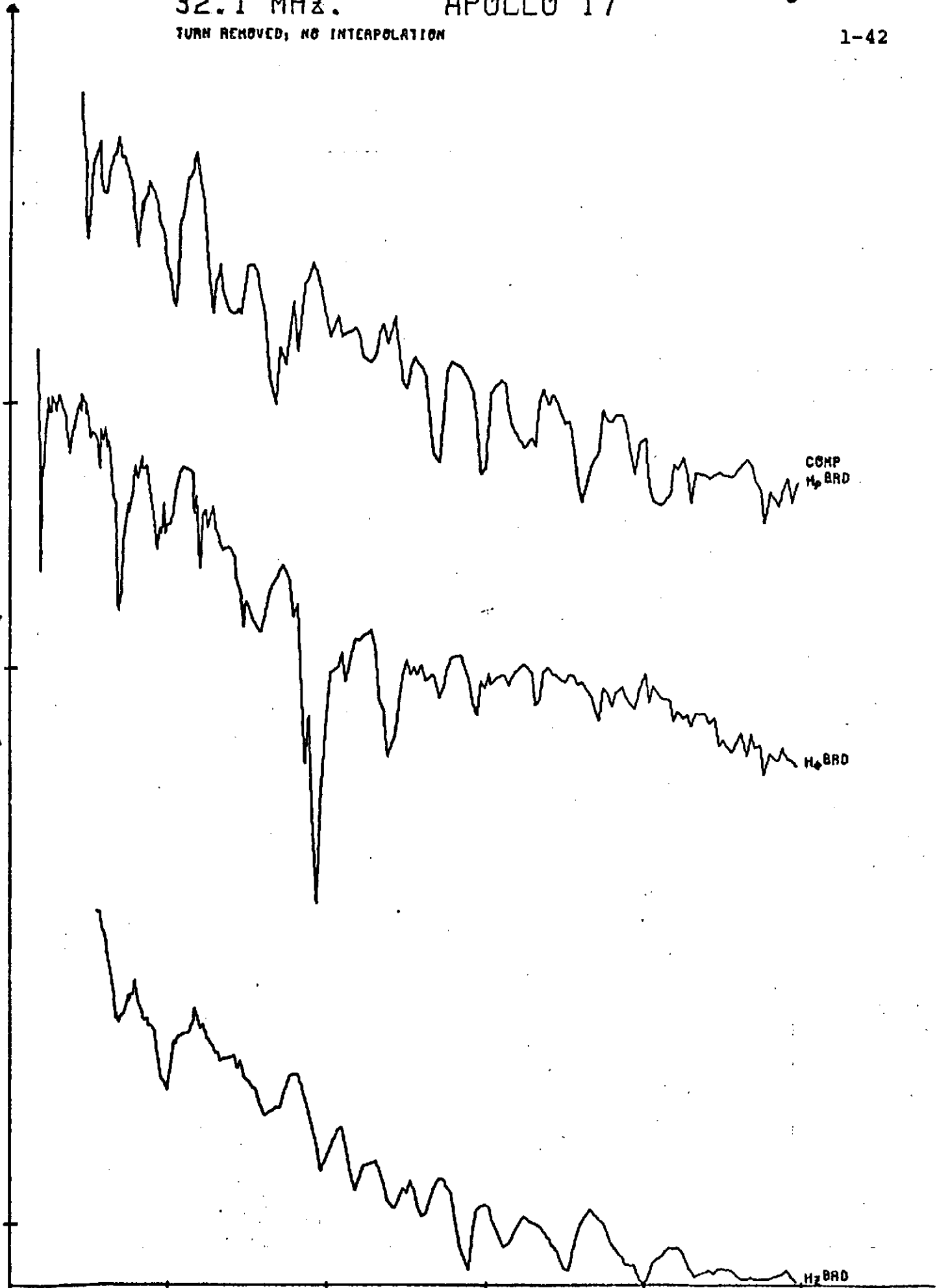
COMP
H₂ BRD

H₂ BRD

H₂ BRD

RANGE λ

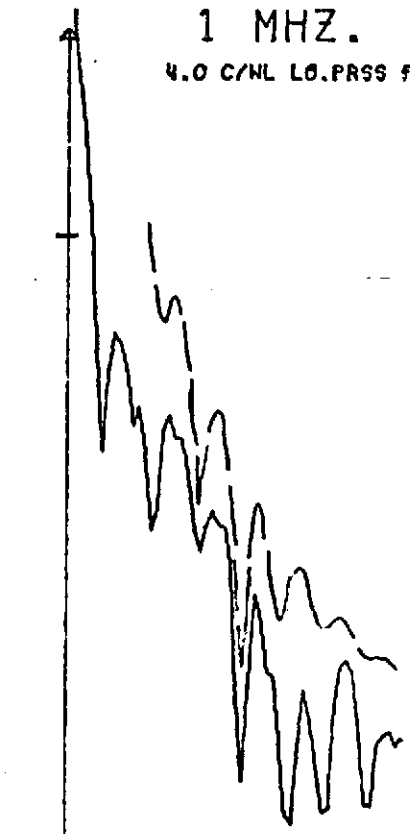
0 4 8 12 16 20



1 MHZ.
4.0 C/NL LO.PRSS FILTER

Fig 9(a)

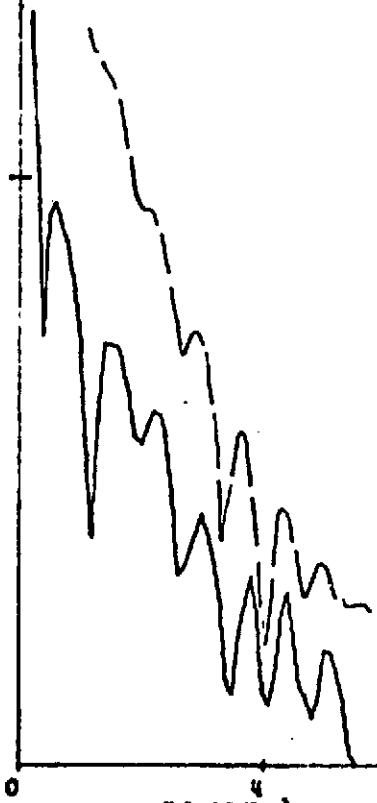
1-43



COMP	MAX	SITE	RUN	FREQ
H ₂ BRD	66.00	17	1	1

15 DB/INCH

1 MHZ.



ORIGINAL PAGE IS
OF POOR QUALITY

H ₂ BRD	60.60	17	1	1
--------------------	-------	----	---	---

RANGE λ

2 MHZ.

R.O C/NL LO.PASS FILTER

Fig 9(6)

1-44

15 DB/INCH

2 MHZ.

COMP	MAX	SITE	RUN	FREQ
H ₂ BRD	64.84	17	1	2

0

RANGE λ

8

12

H₂ BRD 63.74

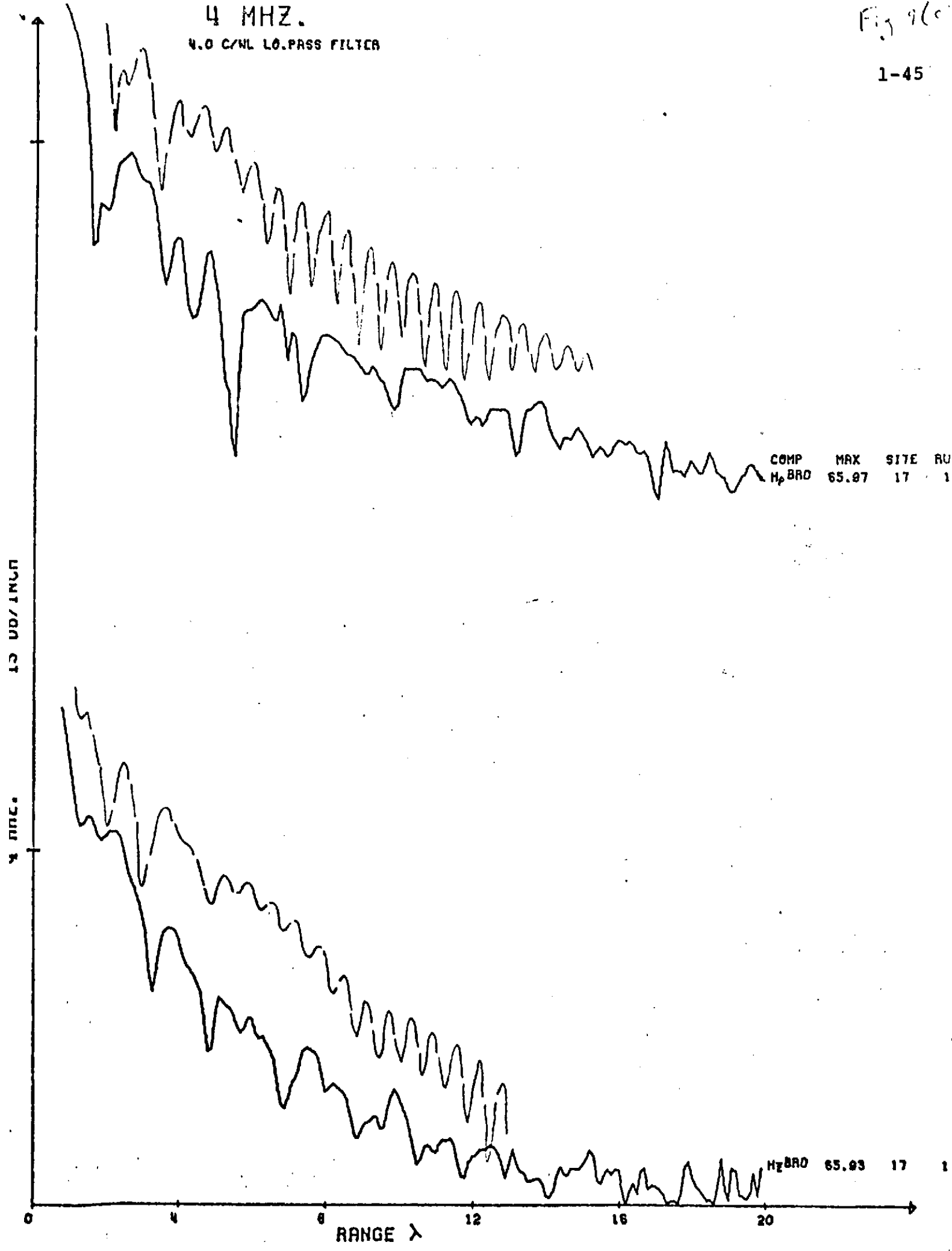
1

2

4 MHZ.
4.0 C/NL LO.PASS FILTER

Fig 960

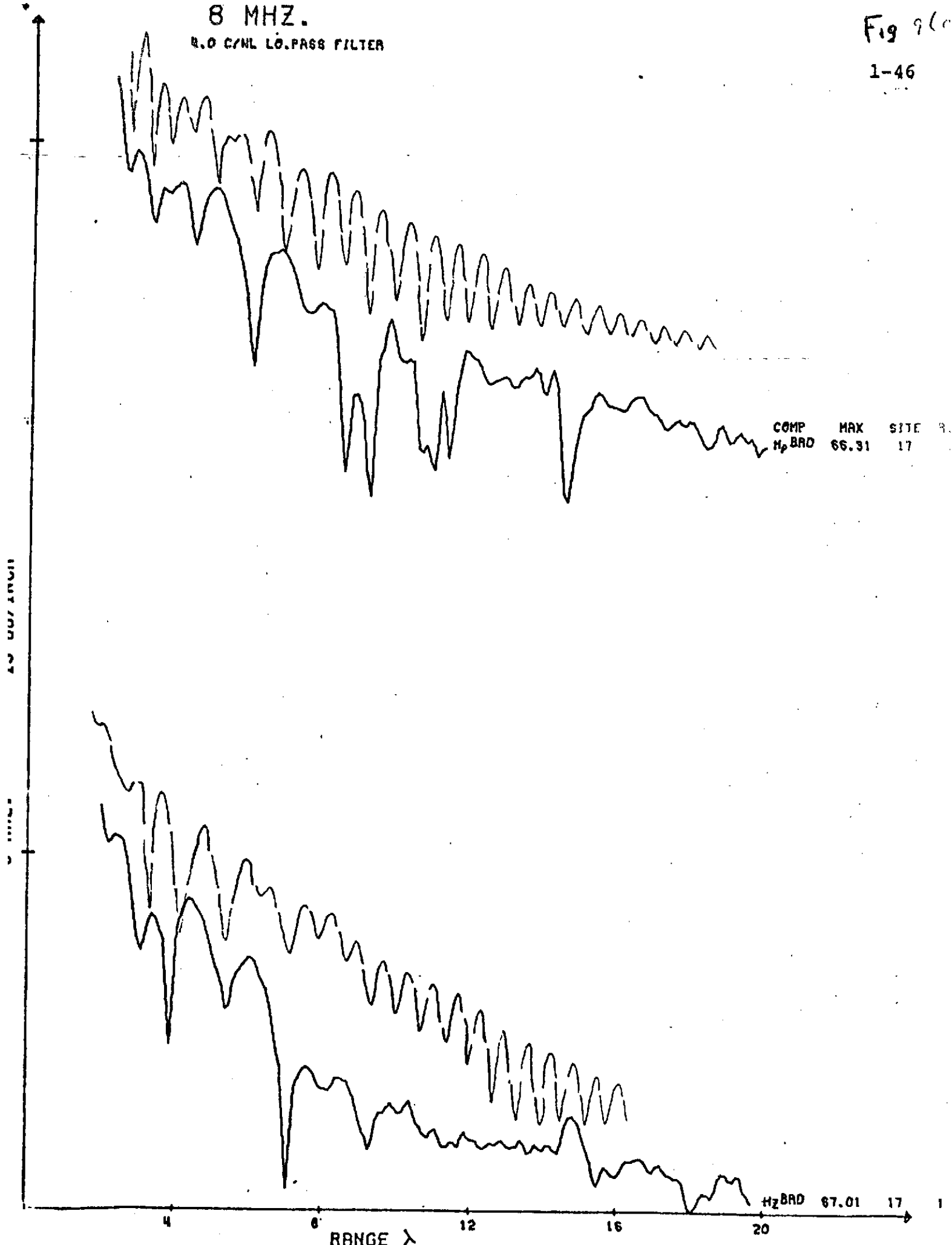
1-45



8 MHZ.
R.O. C/NL LO. PASS FILTER

Fig 96d

1-46



16 MHZ.
N.O C/NL LO.PASS FILTER

Fig 9(e)

1-47

15 DB/INCH

16 MHZ.

RANGE λ

COMP MAX SITE
Hz BRD 66.82 17

Hz BRD 66.79 17

0

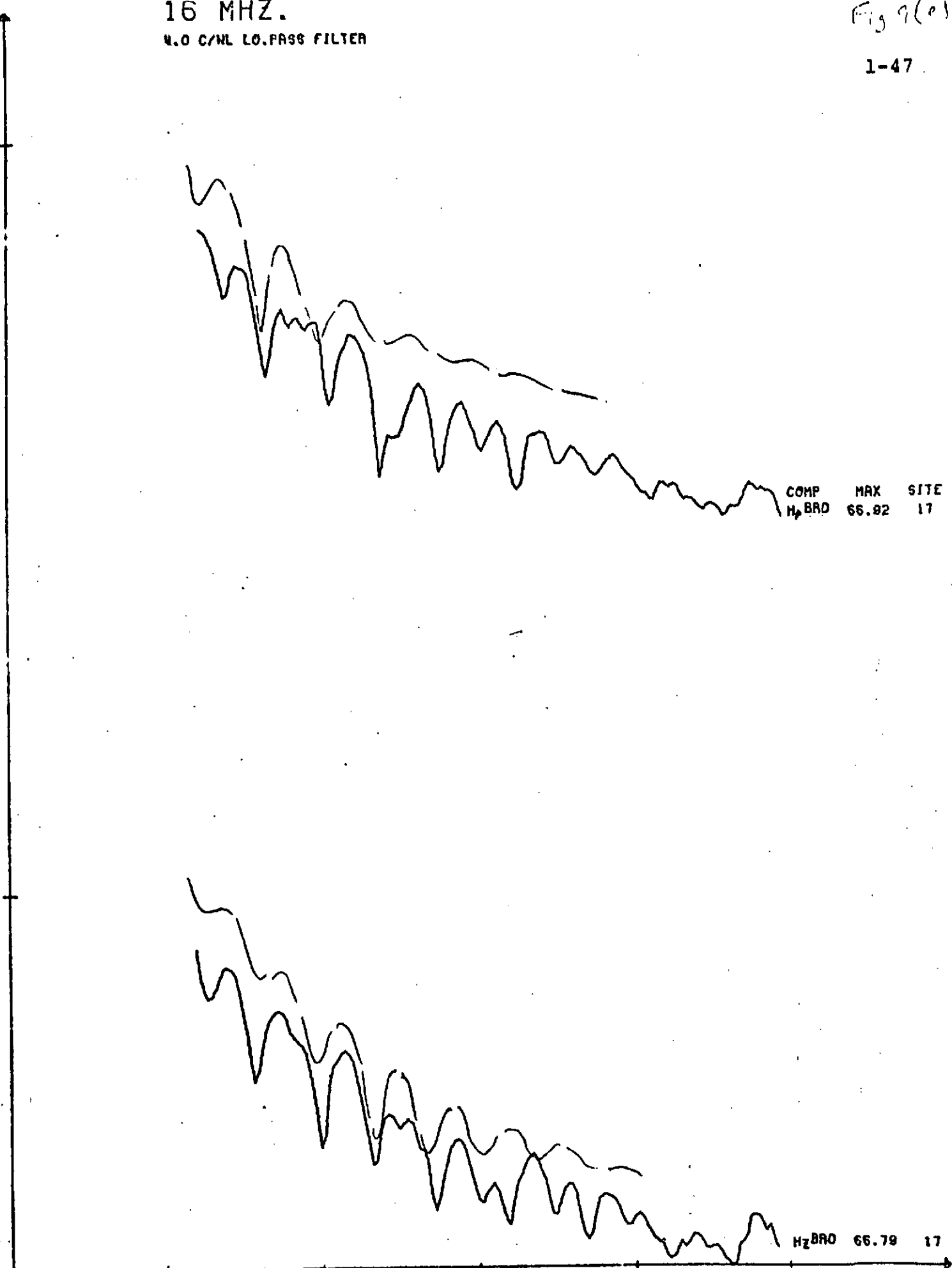
4

8

12

16

20



32 MHZ.
N.O C/NL LO.PASS FILTER

Fig 9(f)

1-48

15 DB/INCH

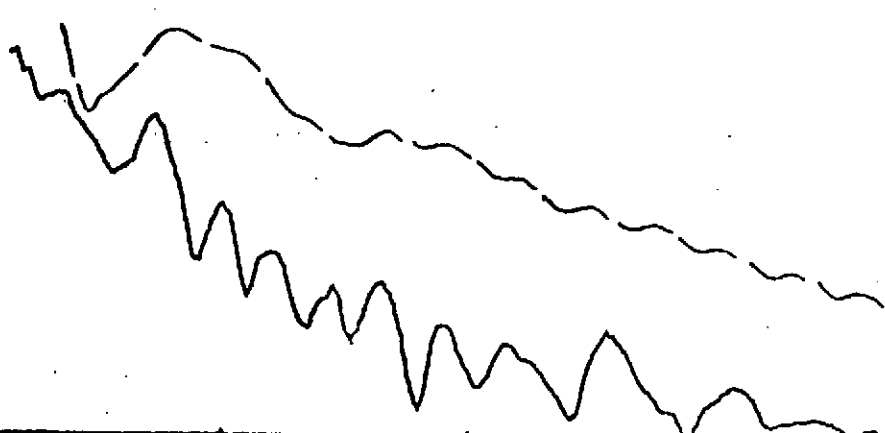
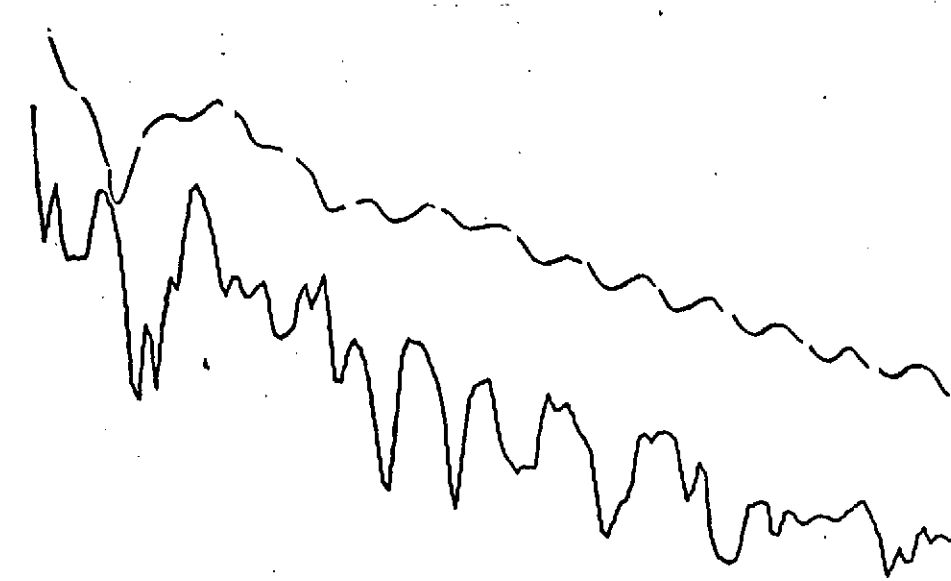
32 MHZ.

COMP	MAX	SITE
H _p BRD	67.26	17

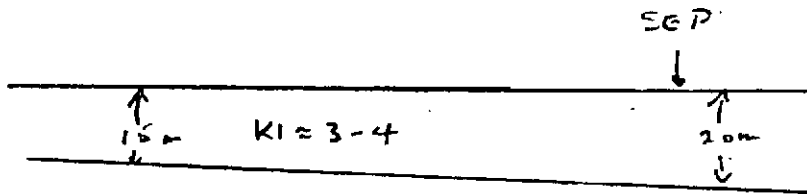
Hz BRD	MAX	SITE
67.22		17

RANGE: λ

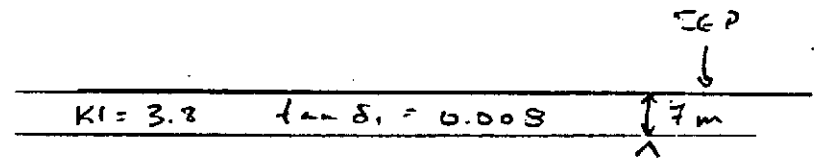
0 4 8 12 16 20



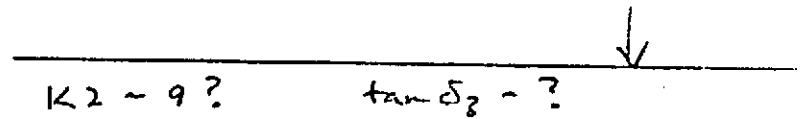
WCST



$K_2 \approx 6-7$



$K_2 = 7.5 \quad \tan \delta_2 = 0.03 \quad 100m$



$K_2 = 9? \quad \tan \delta_2 = ?$

10 (a)

Sloping interface model.

10 (b).

Three-layer model.

ORIGINAL PAGE IS
OF POOR QUALITY

Fig 10.

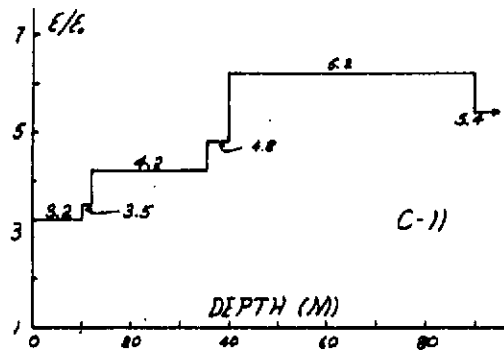


Fig. 11

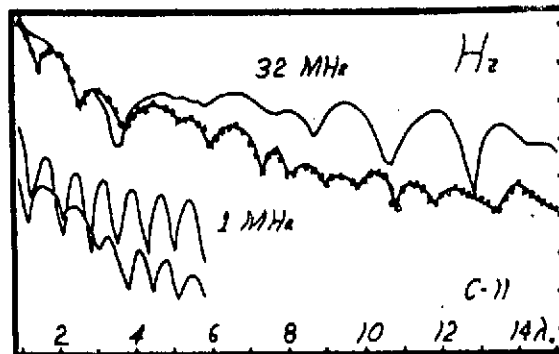


Fig. 12

ORIGINAL PAGE IS
OF POOR QUALITY

THE SURFACE ELECTRICAL PROPERTIES EXPERIMENT

GENE SIMMONS

Dept. of Earth and Planetary Sciences, MIT, Cambridge, Mass. 02139, U.S.A.

DAVID W. STRANGWAY

Geophysics Branch, NASA-Manned Spacecraft Center, Houston, Tex. 77058, U.S.A.

2-1

ELECTROMAGNETIC FIELDS DUE TO DIPOLE ANTENNAS OVER STRATIFIED ANISOTROPIC MEDIA†

3-1

J. A. KONG*

**RADIO INTERFEROMETRY DEPTH SOUNDING:
PART I—THEORETICAL DISCUSSION†**

4-1

A. P. ANNAN*

**RADIO INTERFEROMETRY DEPTH SOUNDING:
PART II—EXPERIMENTAL RESULTS†**

5-1

**JAMES R. ROSSITER*, GERALD A. LATORRACA†, A. PETER ANNAN*,
DAVID W. STRANGWAY*§, AND GENE SIMMONS†**

Interference Patterns of a Horizontal Electric Dipole over Layered Dielectric Media

6-1

L. TSANG AND J. A. KONG

*Department of Electrical Engineering, Massachusetts Institute of Technology
Cambridge, Massachusetts 02139*

REPRINTS INTENTIONALLY OMITTED

ORIGINAL PAGE IS
OF POOR QUALITY

Presented 23 Aug. 73 URSI/IEEE Boulder, Colo. by Gene Simmons for the SEP team.

ELECTROMAGNETIC PROBING OF THE MOON

INTRODUCTION

Last December on the Moon, two astronauts set out equipment for a very simple EM experiment: a transmitter with a half-wave electric dipole antenna. They attached to the Rover a receiver with a loop antenna and a magnetic tape recorder. They then proceeded to measure field strength as a function of distance from the transmitter. From those data, we expected to learn something interesting about the electrical properties of the Moon. Today, I would like to tell you about this experiment--about the theoretical work that we have done so that we could interpret the interference patterns, about the results of field testing both the experiment and equipment on earth before the Apollo 17 mission, and finally, about our present interpretation of the lunar data.

THE CONCEPT

The experiment is extremely simple in concept. This FIRST SLIDE shows the essentials. A horizontal electric half-wave resonant dipole is laid directly on the surface and radiates continuously. The amplitude of the radiation field is measured with a small loop and a calibrated receiver. The data are recorded on magnetic tape. We analyze the data in terms of continuous radiation but actually use switched CW at the frequencies shown on the slide. NEXT SLIDE please.

Slide
1

A very simple conceptual picture of the wave propagation is shown in this slide. One wave travels above the surface, a second wave travels below. In the vicinity of the interface, these two waves interfere and produce a distinctive interference pattern. The characteristics of the pattern depend uniquely on the frequency and the electrical properties of the medium. A third wave may exist. If a reflector is present in the subsurface, then a reflected wave, labeled "C" in this slide, interferes with the other two waves and complicates the pattern. The NEXT SLIDE shows two theoretical interference patterns for a layer over a half space. The usual features of such patterns are these: a rather rapidly decreasing function of distance with superimposed peaks and troughs. The exact details of the peaks and troughs and the rate of decrease with distance depends on the properties of the materials, as well as the presence, number, and depths of reflecting horizons.

2

3

These two curves illustrate nicely the effect of loss tangent of the material. The upper curve is for a loss tangent of 0.01, the lower curve for 0.05. Note that the vertical scale is in Db. So there really is quite a large difference between the pattern for different values of the loss tangent for a given geometry. The NEXT SLIDE shows additional features that are typical of such interference patterns. Note on this slide that I have used linear scales.

4

The high-spatial-frequency wiggles in the early part of the pattern are related to the permittivity of the upper layer. In fact, from the spatial beat frequency, we can calculate the dielectric constant of the upper layer. The prominent peak at about five λ is caused by the reflected wave. The later parts of the pattern are not simple functions of the dielectric constant and depth to reflectors. However, they are very sensitive to small variations in depths and properties. For simple geometries, the origin of the peaks and troughs can be readily identified. So let's look briefly at the theoretical basis of the experiment.

THEORY

The calculation of the field produced by a dipole on the interface between semi-infinite media of differing properties is truly a classic problem in electromagnetic theory. Many in the audience have contributed significantly to the development of the present day solutions. I am sure that most of you have examined the solutions in various forms. If not recently, then at least in your classroom days. The history of solutions to this problem goes back to a 1909 paper by A. Sommerfeld and is replete with mistakes. Indeed, because of the mistakes made by so many prominent scientists and engineers in solving the simple half-space problem, it has been with some considerable trepidation that we have extended solutions to our particular problem.

To put the solution in integral form is reasonably straight forward. NEXT SLIDE, please. We use cylindrical coordinates. The transmitting antenna is located at the origin and we calculate the three components of the field at any point (ρ, ϕ, z) . I show here the integral for one component only as illustration.

k_ρ - transverse wave propagation vector

I_l - moment of the antenna

k_z - z-component of wave vector

R_{TE} - reflection coefficient

$H_1(1)$ - Hankel function of the 1st kind

The reflection coefficient is a function of the properties of various layers and their depths. The exponential term $\exp(ik_z z)$ accounts for the receiver height. In integral form, the solution is elegant and almost certainly free of errors, however, I find it difficult to compare this integral directly with data. Of course, it's in the evaluation of the integral that one is likely to make mistakes. I have always suspected that's why theoreticians lose interest in problems when they get the solution in integral form. So we have used several different schemes to solve the integrals for our particular problem. First, we have solved the integrals numerically

with Simpson's Rule which unfortunately used rather large amounts of computer time. This direct method has provided a very good standard by which to compare other solutions. A second approach to solving the integrals used the geometrical optics approximation (GOA). In the GOA, we can readily identify the origin of the contributions to the total field. In this NEXT SLIDE, I have plotted the relative amplitudes of the individual contributions to the solution for the H_2 field for a particular case. The half-space solution which shows the many characteristic wiggles is identical to the solution that was produced by Sommerfeld in his correct 1926 version, and has been reproduced by many other authors. An excellent discussion of the half-space case is given in the monograph by Baños. Note especially the relative amplitudes of the first reflection, second reflection, third reflection, and so on. It is from such plots as this that we can understand the failure of the radiation fields to decrease monotonically with distance. The contributions from second and third reflections have increased significantly the amplitude of the field. In adding these various reflections, one includes of course, the phase of the signal. 6

Perhaps now is the appropriate time to emphasize that in the SEP experiment we use only amplitude. We would have liked to use phase also but the practical difficulties of detecting, measuring, and recording both amplitude and phase seemed too great--at least within the constraints of a flight experiment.

The NEXT SLIDE lets us compare the geometrical optics approximation with the exact solution obtained with Simpson's Rule. We think that the "fit" is quite good. 7

A third way to evaluate the integrals is that of mode theory. We identify the poles of the integrals on the complex plane and use the theory of residues to evaluate the integrals. The NEXT SLIDE shows a comparison of the result of GOA and mode analysis. We have also included data from a glacier traverse and I will discuss the glacier data later. For this model, at least, both GOA and the mode formulation give comparable results. In actual fact, there is considerable overlap in model conditions for which this occurs. However, for very thin layers, one must use the mode approach. For thick layers, the computation time for the mode approach is prohibitive and the GOA gives adequate solutions. So that we find in working with "real" data that we generally make a choice between the two methods on the basis of practicality when the layers are optically thick, but for thin layers use the mode formulation. 8

And finally a fourth method that we have just begun using is based on the Fast Fourier Transform (FFT) algorithm. With suitable manipulations of the integral, we can get it in a form to use the FFT to solve the integral. In order to keep credits straight, let me mention that Ray Brown and Leang Tsang were mainly responsible for the FFT method. The results obtained with FFT are identical with those obtained with our other methods. Let me show some slides for comparison. In the NEXT SLIDE, we show FFT, Mode, and GOA for 8-1

a two layer model. Then, quickly, the NEXT SLIDE shows FFT and Simpson's Rule for a three layer model. And then in the NEXT SLIDE we compare FFT and Simpson's Rule for a six layer model. The FFT is especially useful for models with many layers. It has the disadvantage though that the source of individual contributions to the solution is not identifiable.

8-2
8-3a
8-3b

Given that the concept of the experiment might work, and given that we have a mathematical formulation that appears to give reasonable looking results, we had to convince ourselves that (1) the experiment really would work, and (2) we had a correct formulation of theory before going to the Moon. After all, one would be rather fool-hardy to go to the Moon to test an experiment only to discover that he had chosen the wrong sign for a square root!

TESTING THE EXPERIMENT

We field-tested both the experiment concept and the mathematical formulations on several glaciers. Why choose glaciers? In order for the subsurface waves to propagate sufficiently far to obtain interference patterns, we needed a geologic material in which the attenuation was low. Everyone knows that ordinary rocks at the surface of the earth are much too conductive because they contain water. We knew of two such geologic materials that occurred in sufficient quantity to provide useful tests--glacial ice and salt. Both have quite low conductivity. The geometry of glaciers seemed better for our purposes and so, early on, we decided to use glaciers. We have tried the SEP technique on the Gornier Glacier in Switzerland, the Athabasca Glacier in Alberta, Canada, and several glaciers and icefields near Juneau, Alaska. But let me describe the results for the Athabasca Glacier only.

We chose the Athabasca for several reasons. It is easy to get there. One can drive to the foot of the glacier. One can even drive tracked vehicles out onto the glacier. In addition, several other workers had previously determined rather well the geometry of Athabasca Glacier by several independent techniques including gravity, DC electrical sounding, some EM sounding, seismic work, and the most definitive of all, actual drilling. Shown in the NEXT SLIDE is a contour map of the Athabasca Glacier. On this slide, the dots indicate the location of drill holes. The heavy line indicates the location of a SEP profile. Along this profile we were able to match the depths to about 5 meters. The NEXT SLIDE is an example of the data obtained on the Athabasca and the quality of the "fits" obtained. Quite frankly, not all field data could be matched equally well with our theoretical curves. Perhaps Dave Strangway will show you some of the misfits. In addition to the gross features shown in this slide--and often matched well--there were also quite a few other features in the glacier data probably caused by scattering of the EM waves off such features as crevasses, holes in the ice, boulders, and bottom topography. Even though we had not identified the cause of such features before the Apollo 17 flight, we were very comforted to find that we could indeed match actual field data with our experiment with the theoretical curves.

Incidentally, I should add that an unstated reason for choosing the Athabasca Glacier is the excellent working conditions shown in this NEXT SLIDE. Also our field assistants, shown in the NEXT SLIDE resting up, rather liked the Athabasca. 11

A second method of testing our mathematical formulation was that of model tanks. We scaled wave lengths and used three centimeter radar equipment, modified somewhat, to obtain interference patterns with various dielectric oils and aluminum plates for reflectors. Shown in the NEXT SLIDE are the results for one experiment. I show this slide for two purposes--to illustrate tank results and to indicate that for very thin layers the GOA is inadequate. Notice that we match extremely well the experimental data with the mode results. Note that we use the E-Field, rather than H. In scale models, at least as we construct them, we were unable to make electrically small loops in order to measure the magnetic field and have contented ourselves with measuring the electric field at the receiver. One of the distinct advantages of using tank models for this kind of work is that one can vary the thickness of individual layers over a large range and can see experimentally the conditions under which the various solutions are satisfactory. 13

Thus, we had essentially three different techniques for verifying that the mathematical formulations for our theory of layered media were essentially correct. One, we could compare with the exact calculations obtained with Simpson's Rule; two, we could match experimentally-observed data on glaciers and could calculate thickness quite accurately; and three, we could match experimentally-observed data from scaled models. From these tests, we were quite sure that our experiment could provide useful data from the Moon.

LUNAR EQUIPMENT

Let's discuss briefly the equipment that was used in the experiment on the Moon. In the NEXT SLIDE, we show the transmitter as it was deployed on the surface of the Moon. Note the solar cell panels, the sole power source for the transmitter. At 1 MHz, we used a power input to the antenna of 4 watts. At the other frequencies, 2, 4, 8, 16, and 32 MHz, the power input to the antenna was 2 watts. The transmitter box was about 1 foot on each side. The transmitting antennas were carried on reels to the Moon and then deployed by the astronauts. The antennas were electric wires with traps placed at the appropriate distances to provide tuned half-wave dipoles at each frequency. Total length of the transmitter antenna, tip to tip, was 70 meters. In the NEXT SLIDE, we see the antenna laid out on the surface. The Rover track was used as a reference for laying the antenna. The NEXT SLIDE shows the receiver and receiving antenna mounted on the Lunar Rover. We were always concerned about parasitic resonances in the Rover and the various tools nearby. As you can see, the SEP receiving antennas were uncomfortably close to various potentially disturbing materials. Apparently, and I use the word with careful consideration, apparently the parasitic resonances did not develop, at least with respect to the horizontal loop. To date, we have mainly analyzed the H_z component. 14 15 16

The NEXT SLIDE shows the receiver in an opened condition and the tape recorder being removed. Note the optical surface reflectors used for cooling the receiver and the thermometer used to monitor the temperature of the receiver. The whole tape recorder was returned to earth by the astronauts. Let's now look briefly at what we've learned from the data. 17

THE LUNAR DATA

First, the location of the lunar experiment. NEXT SLIDE, please. 18
 The location of the Apollo 17 landing site is here. Previous missions were here, here and so on. The Apollo 17 landing site is in the mountains adjacent to the southeast corner of Mare Serenatatis. 19
 The NEXT SLIDE shows an artist's sketch of the general region and the NEXT SLIDE shows the immediate vicinity of the landing site, including the valley, the prominent cliff that is 80 meters high, and the majestic mountains. The planned and actual touchdown spot is shown here. Note the route of the traverses. The location of the SEP transmitter was just south of the LM, about here. We obtained data along the traverse from the SEP site towards Station 2. We also obtained, but have not yet reduced, data from Station 4, back towards the LM. We had planned to obtain data from the SEP site towards Station 6 and beyond. However, a combination of events prevented us. On reaching Station 6, the astronauts found that the switch on the receiver was in the "Standby" position. Subsequently, we were unable to obtain data because of overheating of the receiver. We finally removed the tape recorder about halfway along this traverse in order to prevent the loss of data that had already been recorded. So the data that we have from the Moon consists of the profile from the SEP site towards Station 2, plus some data from Station 4, towards the SEP, which have not yet been reduced. Let's now examine some of the data, and our interpretation of them, from the SEP site towards Station 2. 20
 20A

In the lunar equipment, we used two transmitter antenna orientations, six frequencies, three orthogonal receiving antennas. So, $2 \times 6 \times 3$ is 36 individual profiles for each traverse. In this NEXT SLIDE, I show you one such profile, namely the Hz component for the north-south antenna and for the 16 MHz frequency. For comparison, I show the theoretical profile calculated for a half space with dielectric constant of 3.2. Note how well we match the locations of the peaks and troughs and the falloff with distance. Thus, we are confident that we have the correct values for dielectric constant and for loss tangent. We match equally well the data for the other frequencies. In this NEXT SLIDE, I show the match for the 1 MHz Hz data. With a simple half-space model, we match the data quite well with values of permittivity given in the NEXT SLIDE. Note that the model used for each frequency is a half-space. Because the skin depth varies with frequency, we inferred that these data implied a continuous variation of permittivity with depth. So we drew a model with smoothly varying ϵ with depth and proceeded to calculate the interference pattern. NEXT SLIDE, please. 21
 22
 23
 24
 We used a 20 layer model and the FFT program.

Much to our surprise the pattern showed no peaks and troughs. It varied smoothly with distance. We therefore reject the model of a smoothly varying ϵ with depth.

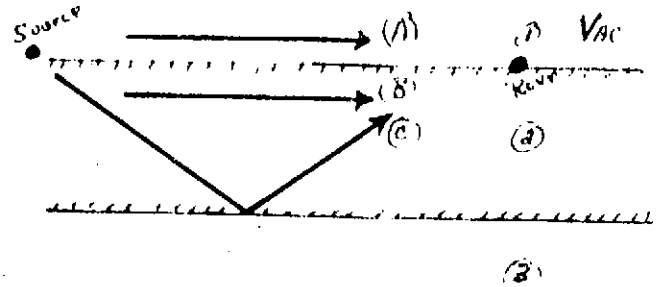
Our current approach is to restrict the models to a few layers and to include finite discontinuities in ϵ . We use the "half-space" values of ϵ as a function of frequency as a guide. We have calculated 2 dozen models with this approach. None fits perfectly. I think, though, that several features have emerged: First, the loss tangent is quite low--at least as low as 0.003 and perhaps as low as 0.001. Second, ϵ near the surface is about 3.2, attains a maximum within 100 to 200 m of the surface and then decreases slightly. Third, discrete layers are present. Fourth, ϵ does not change significantly from 5.6 over the next 2 - 2 1/2 km. Fifth, free water is not present in the outer 2 1/2 km of the Moon, at least at the Apollo 17 site.

In this NEXT SLIDE, I show our present best model. As you can 25 see, the match is not perfect and we clearly have not yet wrung out all the information in even the H_2 data.

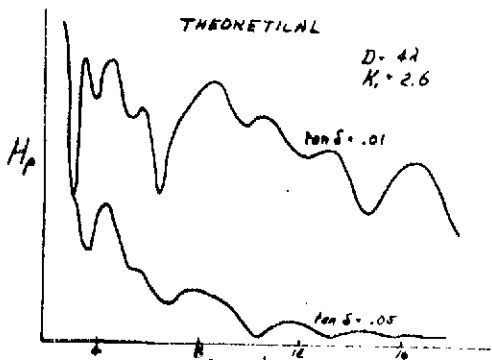
Let me summarize the status of the SEP experiment. We have 26 developed and fully tested the concepts that the field strength of the radiation from a dipole antenna can be used to estimate the electrical properties of subsurface materials and to determine the geologic structure. We have applied this technique to the study of the Moon and several glaciers. We suggest that the same technique with some modifications may very well be useful for prospecting for subsurface water in arid regions and for the study of salt domes and salt deposits. In connection with the lunar experiment, our analysis is still in progress but we have found a "best" model that fits the gross features. In closing, let me say that we had great confidence that our equipment would work properly on the Moon. On the other hand, we did have backup equipment in case of failure, shown in the NEXT SLIDE. For some reason, Jack Schmitt insisted on wearing a 27 disguise whenever he practiced.



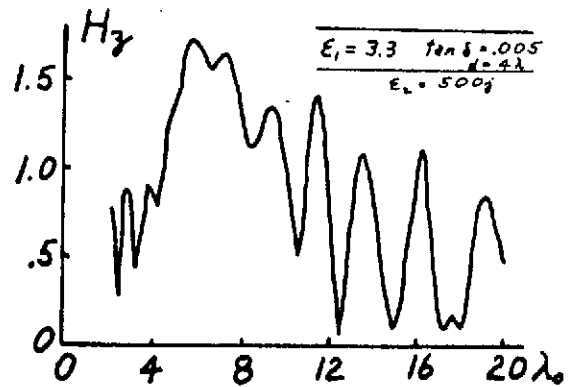
Freqs: 1, 2, 4, 8, 16, 32 MHz



1



2



3

4

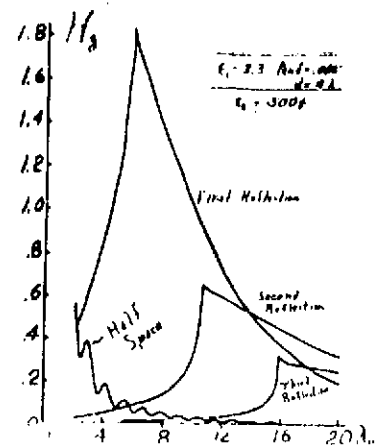
5

$$H_p = \int d\theta_p \frac{I R A^2}{8\pi h_p} (1 + R'')$$

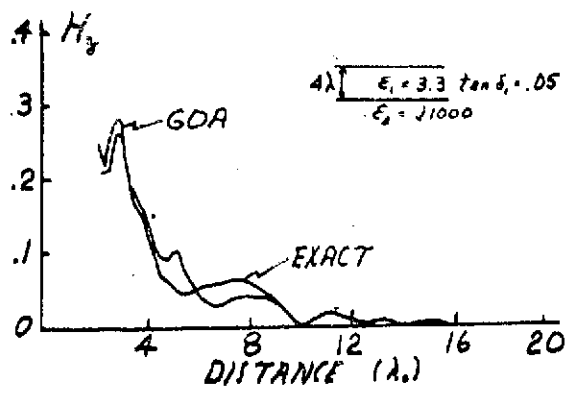
$$\cdot e^{-\gamma z} H_1^{(1)}(h_p \rho) \sin \phi$$

$$R'' = f(h_p, \mu, \epsilon, d_s)$$

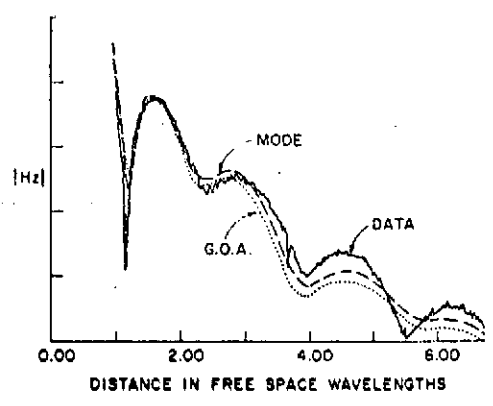
6



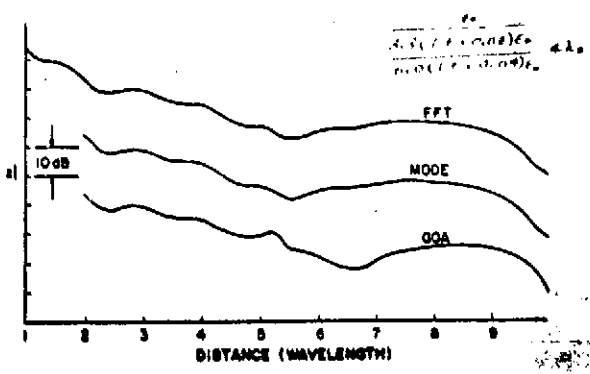
ORIGINAL PAGE IS OF POOR QUALITY



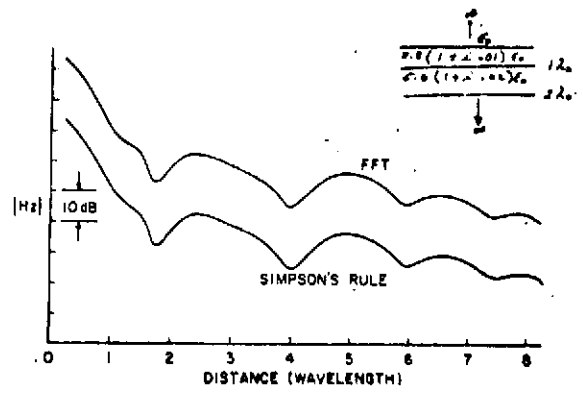
7



8



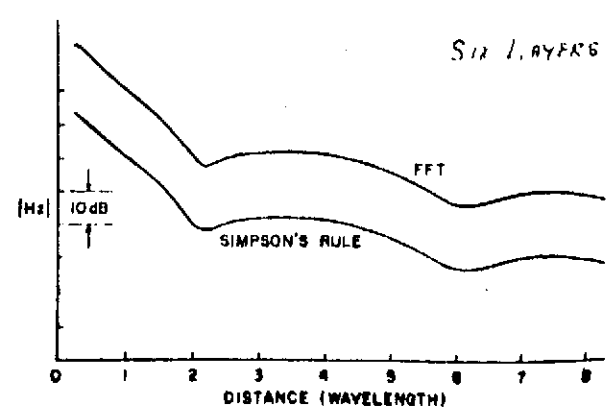
8-1



8-2

SIX LAYER MODEL FOR FFT TEST

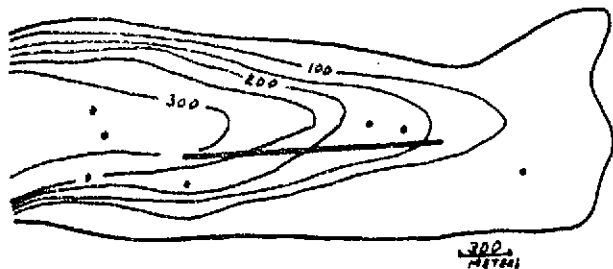
ϵ_i/ϵ_0	$d_i(\lambda_0)$
2(1 + j.01)	0.5
3(1 + j.02)	1
4(1 + j.03)	2
5(1 + j.04)	3
6(1 + j.05)	4
8(1 + j.06)	∞



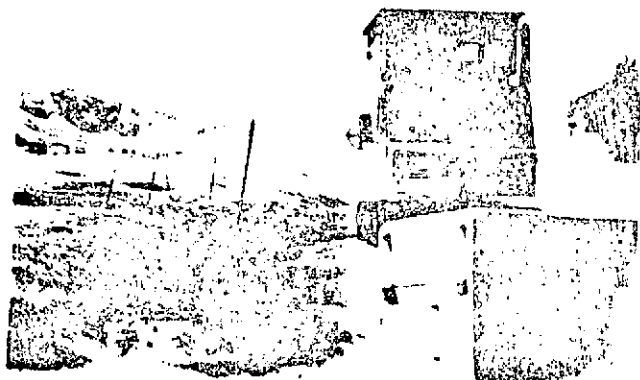
8-3b

8-3a

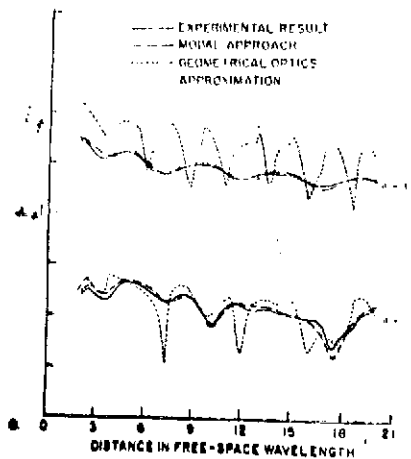
ATHABASCA



9



11



14

13 ORIGINAL PAGE IS OF POOR QUALITY

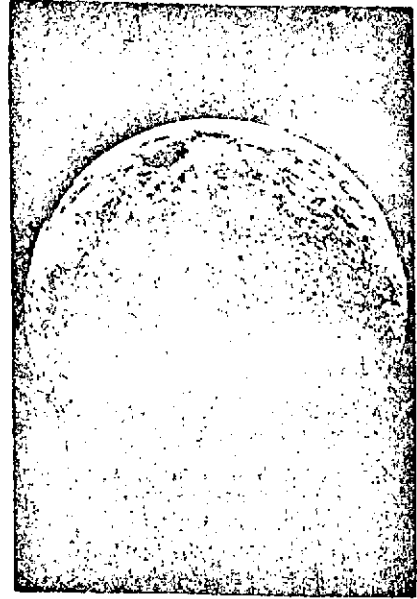


15

16 (Note image is reversed in this slide)



17



18



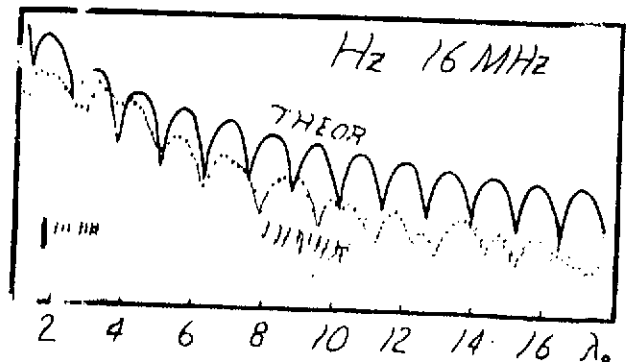
19



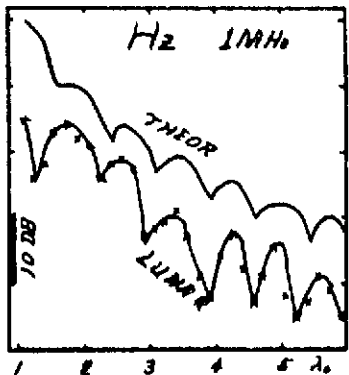
20



20A



21

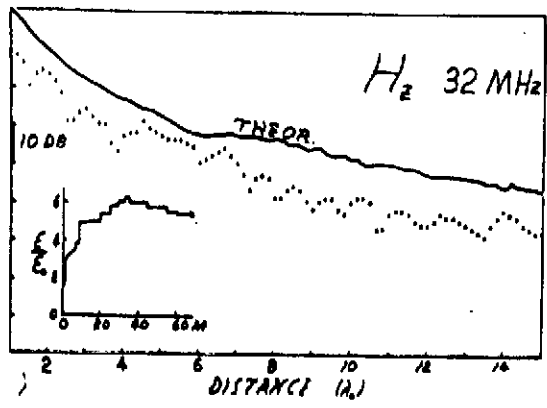


22

SEP RESULTS

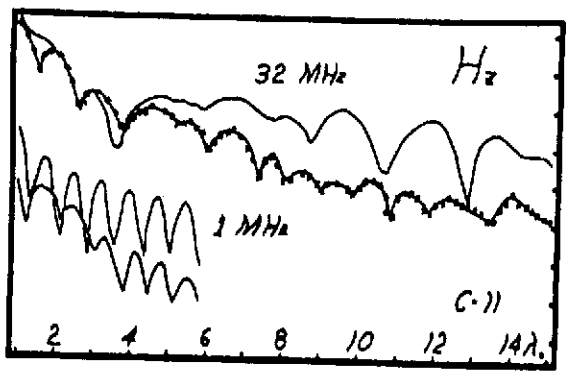
Hz N-5 ANTENNA

f (MHz)	ϵ/ϵ_0
1	5.4
2	6.2
4	4.2/4.8
8	3.2
16	3.2
32	3.2

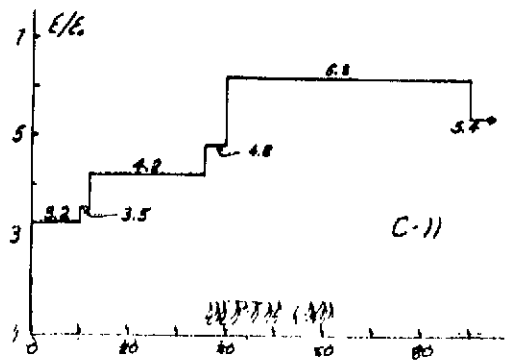


24

23



25



26

ORIGINAL PAGE IS OF POOR QUALITY

27

GEOPHYSICAL SUBSURFACE PROBING
WITH RADIO-FREQUENCY INTERFEROMETRY*

by

J. A. Kong⁺, L. Tsang⁺, and Gene Simmons⁺⁺

Abstract: The radio-frequency interferometry method can be used to probe interiors of celestial bodies and terrestrial areas with low conductivity. Several glaciers have been studied with this technique. An experiment based on this method was designed for Apollo 17 to examine the lunar subsurface. In order to interpret the interference patterns, we have studied theoretically the electromagnetic fields due to a dipole antenna on the surface of a horizontally stratified n-layered medium. Three approaches are used to calculate the interference patterns: 1) direct numerical integration 2) asymptotic evaluation by the saddle point method 3) residue series approach. The asymptotic approach leads to the geometrical optics interpretation. The residue approach leads to modal analysis. Validity of the formulation is checked by comparisons with analogue model tank experiments and actual field data obtained from glaciers.

* This work was supported in part by NASA Contract No. NAS9-11540 and in part by the Joint Services Electronics Program (Contract DAAB07-71-C-0300). The paper was originally presented at the URSI Symposium held at Williamsburg, Virginia, December 15, 1972.

+ Department of Electrical Engineering and Research Laboratory of Electronics, Massachusetts Institute of Technology.

++ Department of Earth and Planetary Sciences, Massachusetts Institute of Technology.

1. INTRODUCTION

The subsurface of planetary bodies, including the earth and its moon, can be examined with electromagnetic waves. In 1955, radio-frequency interference fringes were used for geophysical prospection of underground water in the Egyptian desert¹⁻². Recently the technique was developed for use during the Apollo 17 mission to measure the subsurface electromagnetic properties of the moon³. In the experiment, a transmitting antenna consisting of a pair of orthogonal dipoles is laid directly on the lunar surface. The antenna radiates sequentially at frequencies of 1, 2.1, 4, 8.1, 16 and 32.1 MHz in a time window of 100 millisecond for each frequency. The time window is sufficiently long that the experiment is effectively a continuous wave experiment. A receiving antenna consisting of three orthogonal loops is mounted on the lunar roving vehicle. As the vehicle traverses the lunar surface, the strengths of the magnetic field components are measured as a function of distance from the transmitting antenna. The data are recorded on magnetic tape and returned to earth for analysis. The interference patterns of the field-distance plot contain information about the electromagnetic properties of the lunar subsurface. To test both equipment and theory, experiments have been performed on glaciers⁴⁻⁵ in Switzerland, Canada, and Alaska and on a scale model tank in the laboratory.

In this paper, we present the theoretical basis of the experiment and compare the various methods of attack. The mathematical model is a stratified n -layer medium. Each layer is bounded by plane boundaries and possesses different electric permittivity, magnetic permeability, and thickness. Although dipole radiation in the presence of stratified media has been studied extensively⁶⁻¹⁶, a proper account for the interference fringes method is still lacking. The geometrical optics approximation was the first approach used in calculating interference patterns^{1,15-16}. With the use of the reflection coefficient formulation¹⁴, all field components can be expressed in integral forms with a single variable of integration. In order to obtain explicit expressions for the six field components, the following three different approaches are used to evaluate the integrals: 1) geometrical optics approximation, 2) modal approach, and 3) direct numerical integration. The direct numerical integration can be made to yield accurate results and is useful in calculating near field solutions. The geometrical optics approximation consumes very little computer time and permits a very simple interpretation in terms of ray optics. In the modal approach, the solutions are expressed in terms of summations over normal modes pertaining to the structure of the stratified medium.

II. THEORY

1. General Formulation

Consider a stratified medium of n layers. Each layer is homogeneous, isotropic, and horizontal. The electric permittivity and the magnetic permeability of the i th layer are ϵ_i and μ_i , respectively. The zeroth layer is free space. Both layer 0 and t are semi-infinite half-spaces. An infinitesimal dipole lies on the interface between regions 0 and 1. We use cylindrical coordinates ρ , ϕ and z . The origin of the coordinate system is at the dipole. The z -axis is vertical and perpendicular to the interfaces. The angle ϕ is measured with respect to the dipole and ρ is the distance transverse to the z -axis. The electromagnetic fields produced by a horizontal electric dipole, located at the origin of coordinates and oriented in the x -coordinate direction in free space, can be written in terms of their transverse electric (TE) and transverse magnetic (TM) wave fields in the form of integrals. The TE and TM solutions of the fields are:

$$\vec{E}^{\text{TE}} = \int_{-\infty}^{\infty} dk_{\rho} \left(\frac{\omega \mu I l}{8\pi} \right) (1 + R^{\text{TE}}) e^{ik_z z} \begin{bmatrix} -\frac{1}{k_z \rho} H_1^{(1)}(k_{\rho} \rho) \cos \phi \\ \frac{k_{\rho}}{k_z} H_1^{(1)}(k_{\rho} \rho) \sin \phi \\ 0 \end{bmatrix} \quad (1)$$

$$\vec{H}^{-\text{TE}} = \int_{-\infty}^{\infty} dk_{\rho} \left(i \frac{I l}{8\pi} \right) (1 + R^{\text{TE}}) e^{ik_z z} \begin{bmatrix} ik_{\rho} H_1^{(1)}(k_{\rho} \rho) \sin \phi \\ \frac{1}{\rho} H_1^{(1)}(k_{\rho} \rho) \cos \phi \\ \frac{k_{\rho}^2}{k_z} H_1^{(1)}(k_{\rho} \rho) \sin \phi \end{bmatrix} \quad (2)$$

$$\vec{E}^{-TM} = \int_{-\infty}^{\infty} dk_{\rho} \ i \frac{I\ell}{8\pi\omega\epsilon} (1-R^{TM}) e^{ik_z z} \begin{bmatrix} ik_z k_{\rho} H_1^{(1)'}(k_{\rho}\rho) \cos \phi \\ -i \frac{k_z}{\rho} H_1^{(1)}(k_{\rho}\rho) \sin \phi \\ k_{\rho}^2 H_1^{(1)}(k_{\rho}\rho) \cos \phi \end{bmatrix} \quad (3)$$

$$\vec{H}^{-TM} = \int_{-\infty}^{\infty} dk_{\rho} \ \left(\frac{I\ell}{8\pi}\right) (1-R^{TM}) e^{ik_z z} \begin{bmatrix} -\frac{1}{\rho} H_1^{(1)}(k_{\rho}\rho) \sin \phi \\ -k_{\rho} H_1^{(1)'}(k_{\rho}\rho) \cos \phi \\ 0 \end{bmatrix} \quad (4)$$

In Eqs. (1) and (2), $I\ell$ is the antenna strength, ω is the angular frequency, k_{ρ} and k_z are the ρ - and z -components of the wave vector. $H_1^{(1)}(k_{\rho}\rho)$ is the first order Hankel function of the first kind, the prime on the Hankel function denotes differentiation with respect to its argument. In the column matrices, the first element denotes the ρ -component, the second element the ϕ -component, and the third element the z -component. The reflection coefficients R^{TE} and R^{TM} include all contributions due to the stratified medium. They can be obtained by means of propagation matrices¹² which relate wave amplitudes in different layers.

In this paper, we illustrate the solutions of the above formulation with the two layer case, where the reflection coefficients are deduced from (3) and given by:

$$R^{TM} = \frac{1}{R_{01}^{TM}} \left[1 - \frac{1 - (R_{01}^{TM})^2}{1 + R_{01}^{TM} R_{12}^{TM} \exp(i2k_{1z}d)} \right] \quad (5)$$

$$R^{TE} = \frac{1}{R_{01}^{TE}} \left[1 - \frac{1 - (R_{01}^{TE})^2}{1 + R_{01}^{TE} R_{12}^{TE} \exp(i2k_{1z}d)} \right] \quad (6)$$

For simplicity, we use d to denote the depth of the subsurface reflector. Note that the ten integrals in Eqs. (1) through (4) all contain either $1 - R^{TM}$ or $1 + R^{TE}$ in the integrand.

We solve the integrals by the following three approaches.

2. Geometrical Optics Approximation

In the geometrical optics approximation, we expand $1 - R^{TM}$ and $1 + R^{TE}$ in a series.

$$1 - R^{TM} = (1 + R_{10}^{TM}) \left[1 + (1 + R_{10}^{TM}) \sum_{m=1}^{\infty} (R_{10}^{TM})^{m-1} (R_{12}^{TM})^m e^{i2k_{iz}md} \right] \quad (7a)$$

$$1 + R^{TE} = (1 + R_{01}^{TE}) \left[1 + (1 + R_{10}^{TE}) \sum_{m=1}^{\infty} (R_{10}^{TE})^{m-1} (R_{12}^{TE})^m e^{i2k_{iz}md} \right] \quad (7b)$$

Each term in the series can be evaluated by the saddle point method and attributed to a particular image source¹⁵. The wave that arrives at the receiver after one reflection from the subsurface can be traced back to the first image and is identified with the first term in the summation series in Eq. (7). Similarly, the plane wave that arrives at the receiver after n reflections from the subsurface is represented by the n th image and corresponds to the n th term in the summation series.

The wave that reaches the receiver without reflection from the subsurface corresponds to the first term in both expressions. Thus, the first term is the classic half space solution. If there is no subsurface reflector the spatial wavelength of the interference pattern λ_{int} is related to the refraction index n_t of the half-space medium by

$$n_t = 1 + \lambda_0 / \lambda_{int} \quad (8)$$

where λ_0 is the free space wavelength corresponding to the transmitting antenna frequency. From measurements of λ_{int} we can estimate the value of the index of refraction of the half-space medium.

When there is a subsurface reflector, the energy per unit angle launched from the transmitting antenna into the first layer in the broadside direction, is a maximum at the critical angle

$$\theta_c = \sin^{-1} (1/n_t) \quad (9a)$$

If the peak due to the first reflection occurs at a distance ρ_c , then the thickness of the layer, d , is given by

$$d = \rho_c / 2 \tan \theta_c = \frac{\rho_c}{2} \sqrt{n_t^2 - 1} \quad (9b)$$

In the endfire direction, the energy per unit angle launched from the transmitting antenna into layer '1' is a maximum at the angle

$$\theta_d = \sin^{-1} \sqrt{2/(1 + n_t^2)} \quad (10a)$$

If the peak due to the first reflection occurs at the distance ρ_d , then the layer thickness is given by

$$d = \rho_d / 2 \tan \theta_d = \frac{\rho_d}{2} \sqrt{\frac{n_t^2 - 1}{2}} \quad (10b)$$

The complete interference pattern is obtained by summing all the wave components with due regard given to both amplitude and phase. It is sometimes suggested that Eqs. (9b) and (10b) be used to predict the depth of the subsurface reflector. In practice, the peak positions due to the first reflections in the actual experimental data are difficult to identify.

3. Mode Analysis

In the mode analysis, we first find all the poles of $1 + R^{\text{TE}}$ and $1 - R^{\text{TM}}$ in the complex plane of k_ρ . The original path of integration from $-\infty$ to $+\infty$ is then deformed to the steepest path passing through the saddle point. In the case of a receiver near the surface the saddle point occurs at $k_\rho = k$. The value of the integral is then equal to the sum of the residues of each pole lying between the original path and the steepest descent path plus the saddle point contribution and any branch cut contributions. The poles of $1 + R^{\text{TE}}$ and $1 - R^{\text{TM}}$ are determined from

$$R_{10}^{\text{TE}} R_{12}^{\text{TE}} \exp(i2k_{1z}d) = \exp(i2\ell\pi) \quad (11)$$

$$R_{10}^{\text{TM}} R_{12}^{\text{TM}} \exp(i2k_{1z}d) = \exp(i2\ell\pi) \quad (12)$$

Setting $\ell = 0, 1, 2, \dots$ yields positions of the poles. Each pole corresponds to a wave mode¹¹. The modes with wave vector components $k < \text{Re}(k_\rho) < k_1$, $\text{Im}(k_\rho) \geq 0$, $\text{Re}(k_z) < 0$ and $\text{Im}(k_z) > 0$ are surface wave modes. They correspond to waves that reach the receiver from the surface and decrease in magnitude exponentially as they leave. There are only a finite number of surface wave modes being excited and they are the significant ones when distance is large from the transmitter.

The other group of modes are the leaky wave modes. The wave vector components $\text{Re}(k_\rho) < k$, $\text{Im}(k_\rho) > 0$, $\text{Re}(k_z) > 0$ and $\text{Im}(k_z) < 0$. They correspond to waves that reach the receiver from beneath the surface and increase in magnitude exponentially as they leave the surface. There are an infinite

number of leaky wave modes being excited and they decay very rapidly with distance from the transmitting antenna. They are important only in the near and intermediate ranges.

In evaluating the integrals, the original path of integration is deformed to the steepest descent path passing the saddle point. For the poles that lie between the original and the new path of integration, the corresponding modes are excited. For the poles that lie close to the saddle point, their effect on the saddle point contribution must be taken into account by using the modified saddle point method. The saddle point contribution corresponds to the direct wave from the transmitter to the receiver.

The number of excited modes depends on the thickness of the slab. When the slab is thicker, there will be more surface wave modes existing between the old and the new path of integration. If the slab is sufficiently thin, no surface mode will be generated.

In addition to the saddle point and the pole contributions, there are two branch points at $k_\rho = k_1$ and $k_\rho = k_2$. Since the integrand is an even function of k_{1z} , the branch point at k_1 does not contribute to the integral. The contribution due to the branch point k_2 corresponds to an inhomogeneous wave decaying away from the bottom surface with $\exp(-2\sqrt{k_2^2 - k_1^2}d)$. Thus the inhomogeneous wave is important only when the slab is sufficiently thin.

4. Numerical Evaluation

The integrals in Eqs. (1) through (4) can be readily evaluated numerically provided they are well defined and properly convergent. In the actual computation procedures, we change the Hankel functions to Bessel functions and integrate from 0 to ∞ instead of $-\infty$ to $+\infty$. Although the Hankel function has a singularity at $k_\rho = 0$, the integrand as a whole is regular at that point. For the integrands to be well defined, we must avoid the branch point $k_\rho = k$. When $\text{Im}(k) \neq 0$, the branch point does not lie on the path of integration. If $\text{Im}(k) = 0$, we choose the Sommerfeld path for the integration.

Simpson's rule is used in carrying out the numerical integration. The amount of computer time needed to obtain a given accuracy is reduced in two ways. First, because of the presence of the factor $\exp(ik_z z)$ in the integrand, we choose $z \neq 0$; the larger the value of z , the faster is the rate of convergence. Physically, this choice corresponds to having the receiving point above the surface. In the lunar experiment, the receiving antenna is about 2 meters above ground when mounted on the Lunar Roving Vehicle. Secondly, we vary the integration increments Δk_ρ as a function of distance from the transmitter. The magnitude of Δk_ρ depends mainly on the rate of oscillation of the Bessel function which for large value of the argument $k_\rho \rho$ is proportional to $\cos(k_\rho \rho)$.

For comparison with other techniques, we have evaluated numerically the H_z -component of a two layer model with a perfect reflector. The frequency is 8MHz which corresponds to a free-space wavelength of $\lambda_0 = 37.5$ meters. The layer has

dielectric constant $3.3\epsilon_0$, loss tangent 0.01, and a layer thickness of $4\lambda_0$. The results are shown in Fig. 6. The receiving antenna has a height of 3 meters. We used Δk_ρ as small as 0.5 to determine the increment Δk_ρ . With a distance of $\rho \leq 14\lambda_0$, $\Delta k_\rho = 0.5/14\lambda_0 \approx 0.004$. The computation is stopped when the absolute magnitude of the integrand becomes smaller than 0.002 of the accumulative area. About 5000 increments are used typically for computation. Computation time on the IBM 360-65 was about 2 minutes per point as shown in Figure 1.

The numerical method has both advantages and disadvantages. If the technique is properly applied, the results can be made quite accurate. But the computation time is large and it provides no physical insight. However, as opposed to other asymptotic methods, which are valid only when the distance is far from the transmitter, the numerical method is valid for all distances. Thus the numerical method provides a useful check for other techniques of computation. Most useful of all, it supplements the asymptotic methods for near field calculations. Because the magnitude of the increment Δk_ρ is inversely proportional to ρ , the computation time per point for small values of ρ is also considerably less than that for large values of ρ .

5. Comparison of Theoretical Solutions

In Figure 1, we show H_z as a function of distance calculated on the basis of the three different approaches for a single model. The model consists of a single layer, 4λ in thickness, with $\epsilon = 3.3\epsilon_0$ and $\tan\delta = 0.01$, between free space above and a perfect conductor below. The fields are calculated for a

receiver at a height of 3 meters above surface at 8 MHz. Inspection of the figure shows that the results from the mode analysis agree well with those obtained from numerical integration. Note in particular that the positions of the first peaks in the geometrical optics approximation and in the mode analysis occur at different locations. In the following sections, the theoretical calculations are compared with the various experimental results.

III. EXPERIMENTAL CONFIRMATION

Both the concept of this experiment and the equipment have been tested extensively on glaciers and with laboratory-sized scale models. Because of the variability of natural materials, we used several different glaciers--the Gorner Glacier in Switzerland, the Athabasca Glacier in Alberta, Canada, and several glaciers that drain the Juneau, Alaska icefields. Each of these glaciers had been studied previously. Because the shape, depth, and physical properties of each glacier were known already¹⁷⁻²⁰, the data obtained on the glaciers can be used to check our theoretical expressions. Although we have collected data on several profiles on the Gorner, about 50 profiles on the Athabasca and about 120 profiles with lengths of 1 to $1\frac{1}{2}$ km on the Juneau glaciers, we shall cite results for only two profiles. These results are typical of the other profiles.

1. The Gorner Glacier

The Gorner glacier, located in southern Switzerland, has been studied for more than a century. The rather extensive set of data includes the results of gravity, seismic, and (D.C.)

electrical resistivity surveys. The thickness and shape of the glacier were well-determined. Our field gear was quite simple and included a General Radio 1330A bridge oscillator for the transmitter, a Galaxy R530 communications receiver, and homemade antennas. The glacier was quite thick in our test area. In Fig. 1 we show the interference pattern of the vertical magnetic component for the broadside transmitting antenna at 10 MHz. The observed peaks and troughs match very well the corresponding features in the theoretical curve calculated for a one layer medium with dielectric constant $3.2\epsilon_0(1 + i0.03)$. For one layer media, the summation terms in Eq. (7) do not contribute.

2. The Athabasca Glacier

The Athabasca glacier, located about 75 miles south of Jasper, Alberta, Canada, has been thoroughly studied¹⁹⁻²⁰ also by such other methods as seismology, gravity, electrical resistivity measurements, and drill holes. The ice thicknesses measured by seismic reflections and by direct measurement in boreholes agree quite well and we use the profiles reported by Paterson and Savage as standards with which to compare the thicknesses determined from our electrical sounding technique. In figure 3, we show typical results, the interference pattern of the vertical magnetic component at 2 MHz. Note the excellent match between the experimental curve and the theoretical curves obtained with both the geometrical optics approximation and the mode analysis. Our interferometry data indicate a depth of 180 meters which is in good agreement with the results of drilling, seismic and gravity surveys.

3. The Scaled Model Tank Experiment

A scaled model tank, operating at 6 GHz, was used to obtain interference patterns for a dielectric layer with dielectric constant $2.16\epsilon_0(1 + i0.0022)$ over an aluminum reflector. The general features of the model tank were described by Rossiter et al.⁵ With the mode analysis, we are able to match the experimental curves from the model tank experiment. To show which modes are excited, we transform to a complex $\theta = \theta' + i\theta''$ plane such that $k_\rho = k \sin \theta$, and $k_z = k \cos \theta$. In Fig. 4, we illustrate on the θ -plane the solution of the H_z -component by the modal approach. There are two double-valued functions k_{1z} and k_{2z} . We choose the two branch cuts to be $\text{Re}(k_{1z}) = 0$ and $\text{Re}(k_{2z}) = 0$. Of the four Riemann sheets, we are interested in the poles on the sheet with $\text{Re}(k_{1z}) > 0$ and $\text{Re}(k_{2z}) > 0$. The excited modes marked with circles are surface wave modes. The excited modes marked with crosses are the leaky wave modes. All unexcited modes are denoted by triangular signs. In Fig. 5, we compare the experimental results for layer thicknesses of 1λ , 2.5λ , and 5λ . Note specifically that for shallower depths the geometrical optics approximation fails to account for even the gross features whereas the mode approach fits the experimental data excellently.

IV. CONCLUSIONS

The radiation fields due to a horizontal electric dipole laid on the surface of a stratified medium have been calculated with three different approaches and compared with the various experimental results. The solutions are obtained from the reflection coefficient formulation and written in integral forms. In the near field of the transmitting antenna, analytical methods involving asymptotic expansion are not applicable. Direct numerical integration of the integrals by a computer is the simplest and the most useful. The numerical method for near field calculations also yields accurate results and uses less computer time than far field calculations. When the receiver is far away from the transmitting antenna, the integrals can be evaluated asymptotically by the method of steepest descents. For lossy media and large layer thickness, the geometrical optics approach gives rather accurate results. The interference patterns calculated from this approach can be easily interpreted in terms of ray optics. When losses are small and layers are thin, the mode approach is most attractive. The results can be interpreted in terms of normal modes of the layered medium. Although the calculations and illustrations presented in this paper were done for the one layer and the two layer cases, the calculations can be readily generalized to handle more layers.

Acknowledgements

We are indebted to Peter Annan, Gerry LaTorraca, Larry Bannister, James Rossiter, Richard Baker, Frank Miller, Raymon Watts, and David Redman for help in collecting the field data; to David Strangway for supplying the tank model data; to Hans Rothlisberger for his assistance on the Groner Glacier; to James Meyer for discussions and to Wen Kong for preparing the manuscript.

FIGURE CAPTIONS

- Fig. 1. Comparison of theoretical results. These interference patterns are calculated for a dielectric layer with dielectric constant $3.3\epsilon_0(1 + i0.01)$ overlying a perfect conductor. The receiver has a height of 0.08 wavelength. The amplitude is normalized with the factor $I\ell/4\pi\lambda^2$.
- Fig. 2. Comparison of Gerner glacier data with theoretical results for the vertical magnetic field component H_z at 10 MHz. The theoretical curve is calculated for a one-layer medium with dielectric constant $3.2\epsilon_0(1 + i0.03)$ with the amplitude normalized with the factor $I\ell/4\pi\lambda^2$. The experimental curve is shifted upward to show the match.
- Fig. 3. A set of Athabasca data taken at 2 MHz, site 3 compared with the theoretical results obtained with mode approach and geometrical optics approach. The theoretical results are calculated for a layer of ice with dielectric constant $3.3\epsilon_0(1 + i0.15)$ and depth $1.2\lambda = 180$ meters. The scale is 8 db/division.

Fig. 4. The complex θ -plane for mode analysis. The calculation is made for a layer of thickness l free-space wavelength and dielectric constant $2.16\epsilon_0(1 + i0.0022)$ lying on a perfect reflector. The transformation is $k_\rho = k_\rho \sin\theta$, $k_z = k_\rho \cos\theta$. The excited surface wave modes and the leaky modes lying between the original path of integration and the path of the steepest descent are shown by circles and crosses, respectively.

Fig. 5. Scaled model tank experimental data compared with theoretical results obtained with the mode approach and the geometrical optics approximation. The model consists of a layer of oil with dielectric constant $\epsilon = 2.16\epsilon_0(1 + i0.0022)$. The subsurface reflector is an aluminum plate.

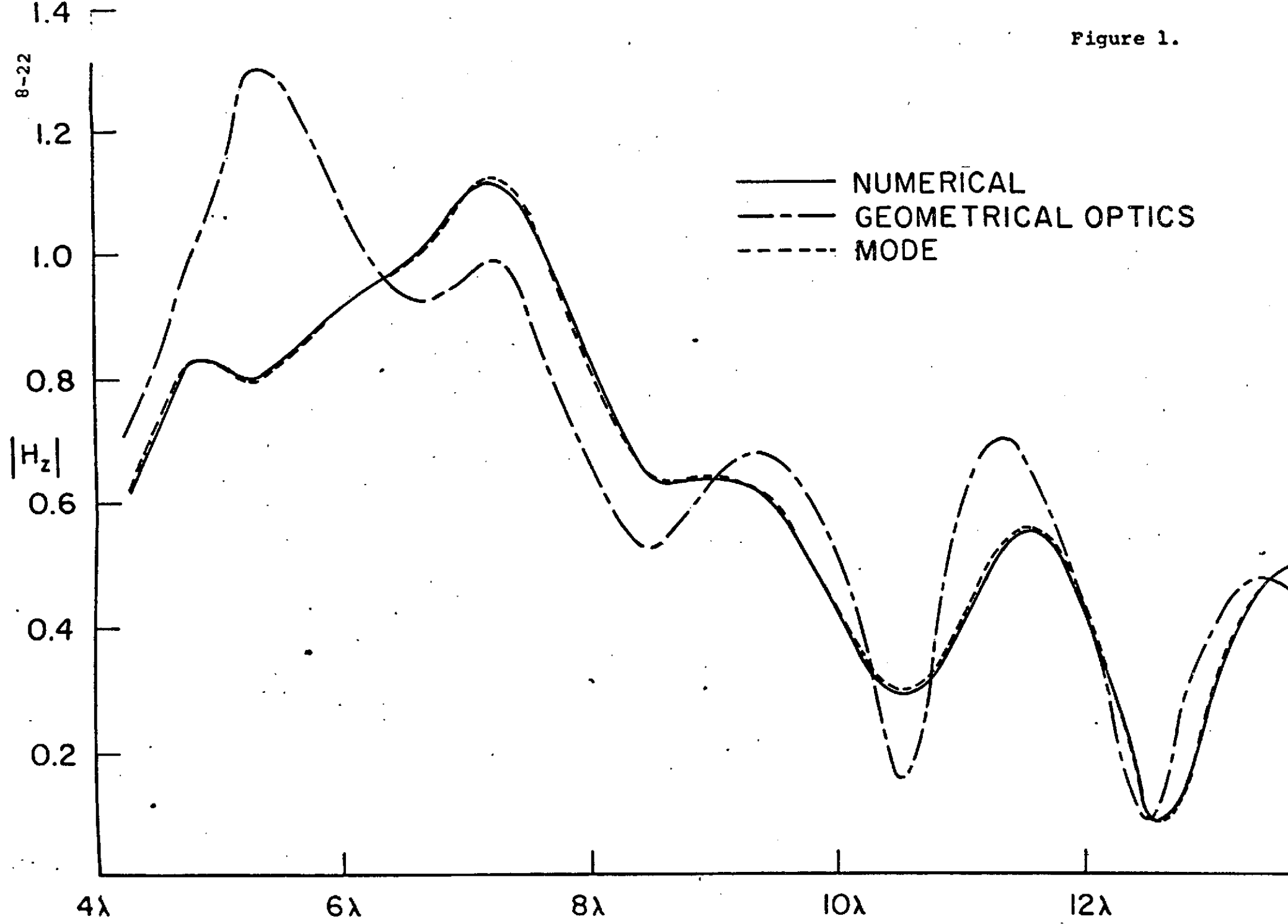
REFERENCES

1. M. A. H. El-Said, "Geophysical Prospection of Underground Water in the Desert by Means of Electromagnetic Interference Fringes," Proc. IRE, Vol. 44, pp. 24-30, Jan. 1956.
2. M. A. H. El-Said, "A New Method for the Measurement of the Average Dielectric Constant of the Underground Medium of Site," IEEE PGAP, Vol. AP-4, pp. 601-604, Oct. 1956.
3. G. Simmons, D. W. Strangway, L. Bannister, R. Baker, D. Cubley, and G. LaTorraca and R. Watts, "The Surface Electric Properties Experiment," Proc. Conf. Lunar Geophys., Houston, Texas pp. 258-270.
4. D. W. Strangway, G. Simmons, R. Watts, G. LaTorraca, L. Bannister, R. Baker, J. D. Redman, and J. R. Rossiter, "Radio Frequency Interferometry - A New Technique for Studying Claciers," in press, J. Glaciology, 1974.
5. J. R. Rossiter, G. A. LaTorraca, A. P. Annan, D. W. Strangway, and Gene Simmons, "Radio Interferometry Depth Sounding, Part II - Experimental Results," Geophysics, June, 1973, Vol. 38, No. 3, pp. 581-589.
6. A. Sommerfeld, Partial Differential Equations, Academic Press, 1949.
7. K. M. Brekhovskikh, Waves in Layered Media, Academic Press, 1960.
8. A. Baños, Dipole Radiation in the Presence of a Conducting Half-Space, Pergamon Press, 1962.

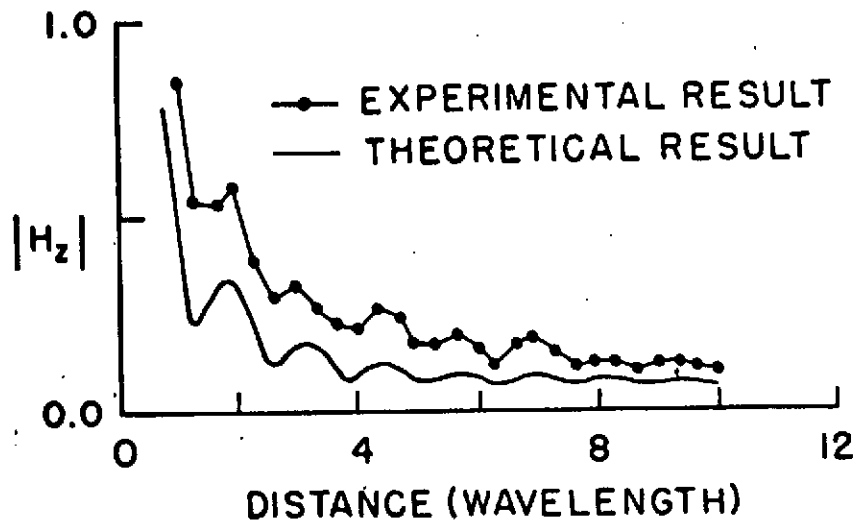
9. P. Gudmandsen, Electromagnetic Probing of Ice: in Electromagnetic Probing in Geophysics (J. R. Wait, ed.), The Golem Press, 1972
10. J. R. Wait, Electromagnetic Waves in Stratified Media, Pergamon Press, 1970
11. L. B. Felsen and N. Marcuvitz, Radiation and Scattering of Waves, Prentice Hall, 1973
12. J. R. Wait, "Influence of a Sub-Surface Insulating Layer on Electromagnetic Ground Wave Propagation," IEEE Trans. on Ant. and Prop., Vol. AP-14, pp. 755-759, 1966.
13. J. R. Wait, "Asymptotic Theory for Dipole Radiation in the Presence of a Lossy Slab Lying on a Conducting Half-Space," IEEE Trans. on Ant. and Prop., Vol. AP-15, pp. 645-648, 1967
14. J. A. Kong, "Electromagnetic Fields due to Dipole Antennas over Stratified Anisotropic Media," Geophysics, V.37, No.6, pp.985-996, Dec. 1972
15. L. Tsang, J. A. Kong, and Gene Simmons, "Interference Patterns of a Horizontal Electric Dipole over Layered Dielectric Media", J. Geophysical Research, Vol. 78, No. 17, pp. 3287-3300, June, 1973.
16. A. P. Annan, "Radio Interferometry Depth Sounding, Part I - Theoretical Discussion," Geophysics, Vol. 38, No. 3, pp. 557-580 June, 1973.
17. S. Evans, "Dielectric Properties of Ice and Snow - a Review," J. Glaciology, v.5, pp.773-792, 1965

18. D. C. Pearce and J. W. Walker, "An Empirical Determination of the Relative Dielectric Constant of the Greenland Ice Cap," J. Geophysical Research, v.72, No.22, pp.5743-5747, 1967
19. J. C. Savage and W. S. B. Paterson, "Borehole Measurements in the Athabasca Glacier," J. Geophysical Research, V.68, No. 15, pp.4521-4536, 1963
20. E. T. Kanasewich, "Gravity Measurements of the Athabasca Glacier, Alberta, Canada," J. Glaciology, V.4, pp.617-631, 1963

Figure 1.



DISTANCE IN FREE-SPACE WAVELENGTH



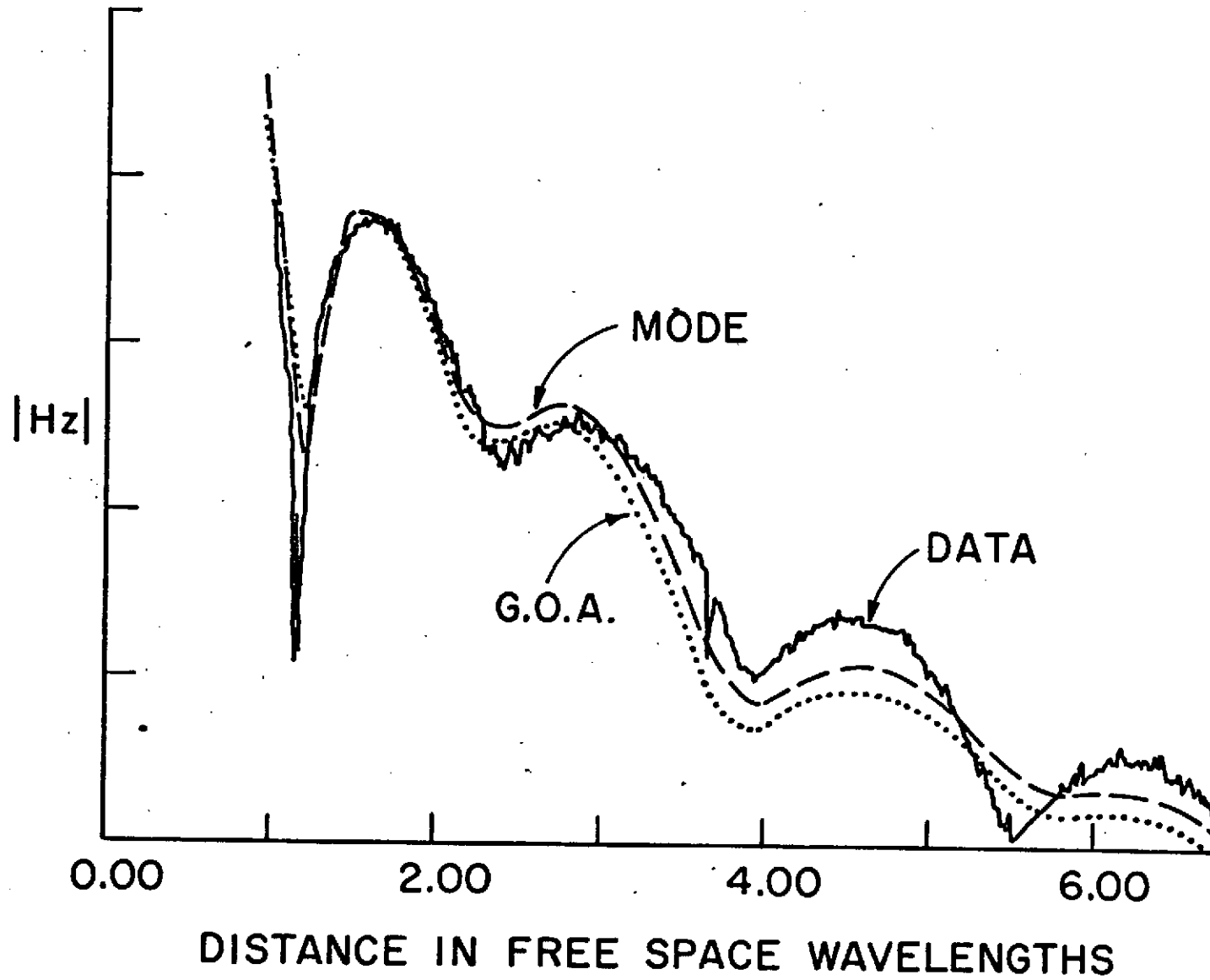
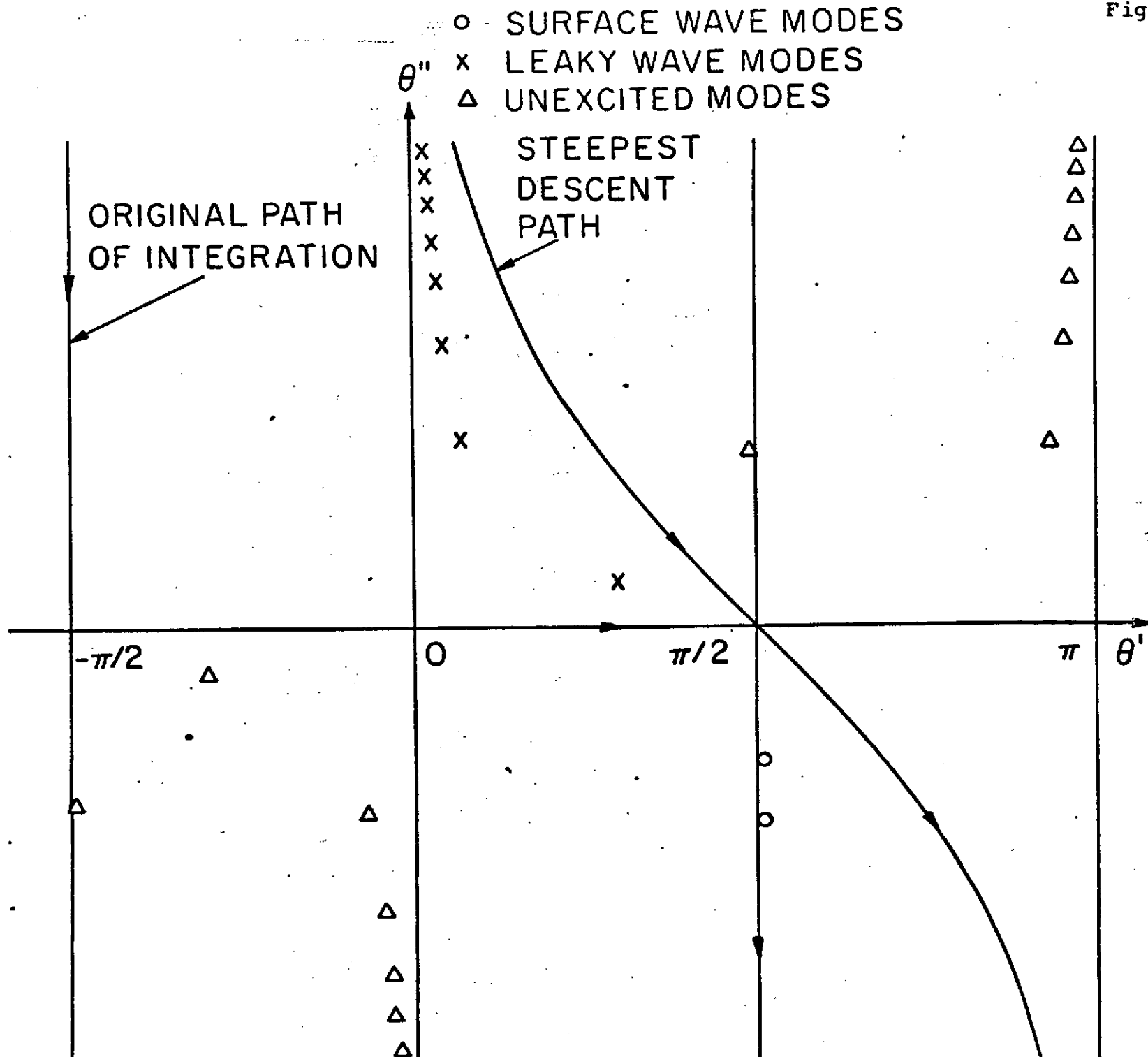
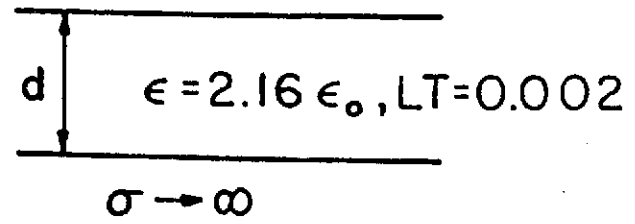
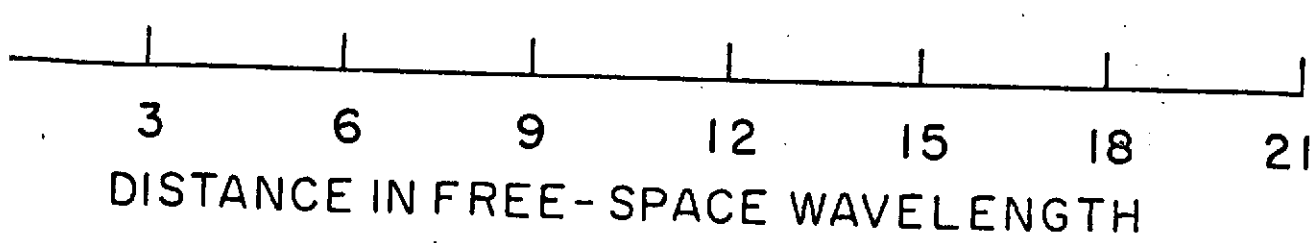
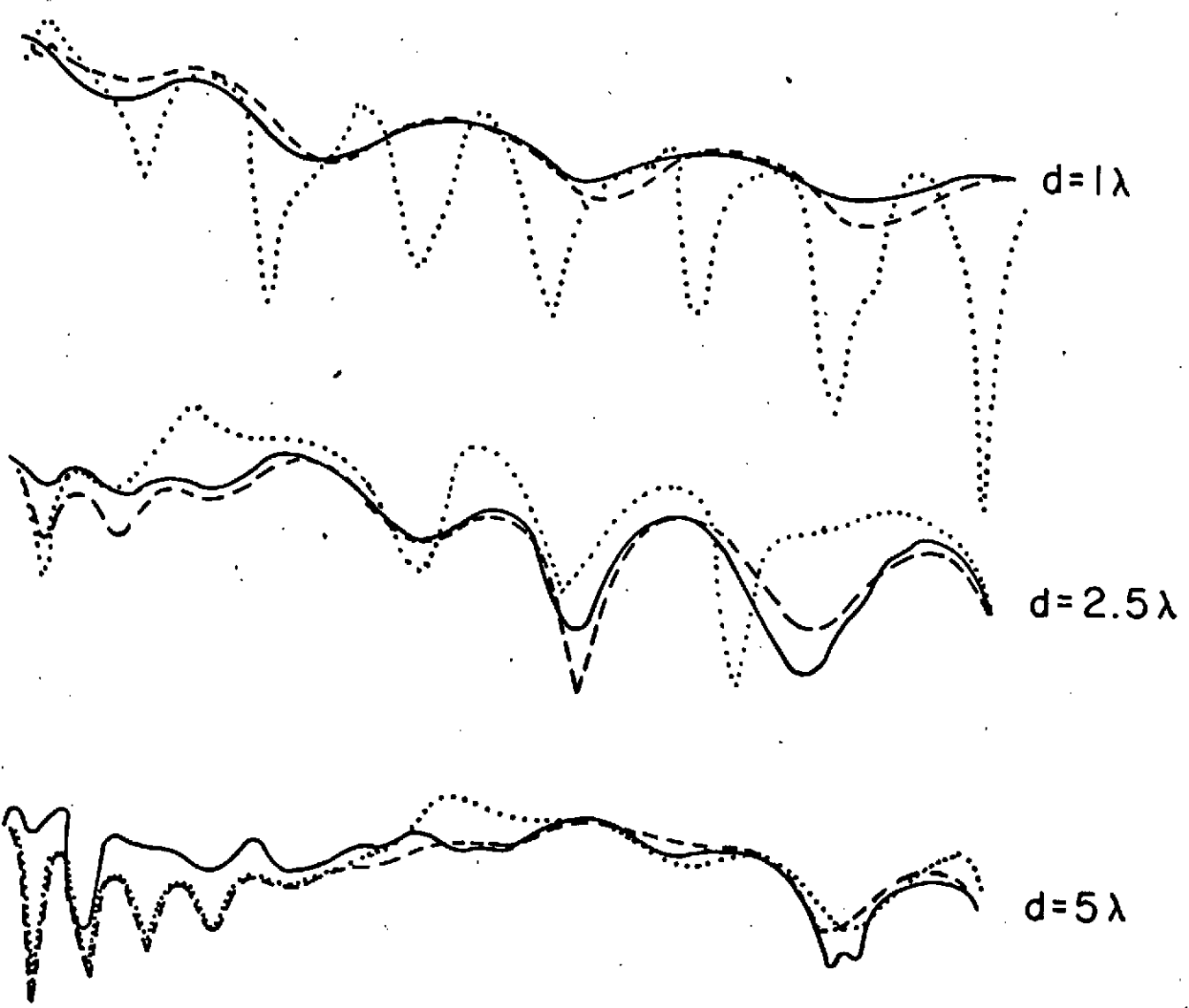


Figure 4.





- EXPERIMENTAL RESULT
- GEOMETRICAL OPTICS APPROXIMATIONS
- MODE APPROACH



Numerical Evaluation of Electromagnetic Field Due to
Dipole Antennas in the Presence of Stratified Media

L. Tsang

Department of Electrical Engineering
Massachusetts Institute of Technology
Cambridge, Massachusetts 02139

Raymon Brown

Department of Earth and Planetary Sciences
Massachusetts Institute of Technology
Cambridge, Massachusetts 02139

J. A. Kong

Department of Electrical Engineering
Massachusetts Institute of Technology
Cambridge, Massachusetts 02139

and

Gene Simmons

Department of Earth and Planetary Sciences
Massachusetts Institute of Technology
Cambridge, Massachusetts 02139

Submitted to the Journal of Geophysical Research 20 March 1973
Revised 31 January 1974

Abstract

Two numerical methods are used to evaluate the integrals which express the EM fields due to dipole antennas radiating in the presence of a stratified medium. The first method is a direct integration by means of Simpson's rule. The second method is indirect and approximates the kernel of the integral by means of the Fast Fourier Transform (FFT). In contrast to previous analytical methods which applied only to two layer cases, the numerical methods can be used for any arbitrary number of layers with general properties.

I. Introduction

In the Radio Frequency Interferometry technique described by Rossiter et al. (1973), propagating electromagnetic waves are used to explore various geological features. This technique was the basis of an Apollo 17 flight experiment to probe the subsurface features of the moon (Simmons et al., 1972, 1974). It has been used also to study several terrestrial glaciers (Strangway et al., 1974).

The theoretical basis of the technique has been described by Annan (1973) and by Tsang et al. (1973). Briefly, the electromagnetic fields due to dipole antennas radiating in the presence of layered media are formulated in terms of reflection coefficients (Kong, 1972) and the results written in integral form for all field components. The chief practical difficulties arise in the evaluation of the integrals. For some techniques, the computation time on a large digital computer is prohibitive. For others, the region of validity does not include any region of interest. These matters are discussed in detail by Tsang et al. (1973) and Kong et al. (1974) who described both analytical and numerical methods for evaluating the integrals. Due to the complication introduced by the reflection coefficients, the analytical methods apply only to a few simple cases. Regions of validity of such analytical methods are also limited. The geometrical optics approximation, mode analysis, and Simpson's rule have been used to solve our problem for the case of a single layer overlying a half space. In this paper, the Simpson's rule has been extended to multilayer cases. In addition, we formulate

the expressions, so that the FFT can be used to calculate the integrals. The case of many layers and the case of continuous variation with depth of the electrical properties can then be readily handled.

II. Formulation of the Problem

Consider the case of a transmitting dipole antenna which is laid on the free surface of a horizontally stratified medium with n layers. For notation, we use a cartesian coordinate system with the dipole coincident with the x -axis. The i th layer is characterized by permeability μ_i , permittivity ϵ_i , and position of the boundaries $z = -d_{i-1}$ and $z = -d_i$. The zeroth-layer is free space and the layer, denoted by $i = t$, extends to infinity in the z -direction. Distance is always scaled to the free space wavelength λ_0 . The integral expressions for the electromagnetic fields due to the radiation from such an antenna have been obtained by Kong (1972). In the region above the stratified medium, all six components of the electric and the magnetic field vectors take the form of an integral which involves Hankel functions of the first kind, reflection coefficients that contain all the information necessary to characterize the medium, and an exponent $\exp(ik_z z)$, where z is the distance above the free surface and k_z is the wave vector component along the z -axis. We shall develop the details for a single field component as typical of the whole set, the vertical component of magnetic field vector H_z . We now use a cylindrical coordinate system with the transmitting antenna located at the origin; ρ denotes distance and ϕ denotes the angle made with the direction of the horizontal dipole.

Then

$$H_z = \int_{-\infty}^{\infty} dk_{\rho} \frac{i I \ell k_{\rho}^2}{8\pi k_z} (1 + R^{TE}) e^{ik_z z} H_1^{(1)}(k_{\rho} \rho) \sin\phi \quad (1)$$

where

k_ρ is the ρ -component of the propagation vector k

l is the current moment of the antenna

R^{TE} is the reflection coefficient

$H_1^{(1)}(u)$ is the Hankel function of the first kind with argument u ,

the reflection coefficient R^{TE} contains all of the information on the physical properties of the medium that pertain to Transverse Electric (TE) fields and is given by Kong (1972)

$$\begin{aligned}
 R^{\text{TE}} = & \exp(i2k_z d_0) \frac{\mu_0^{(+)}{}^1}{\mu_0^{(-)}{}^1} \left(1 - \frac{\mu_0^{(+)}{}^1/\mu_0^{(-)}{}^1 - \mu_0^{(-)}{}^1/\mu_0^{(+)}{}^1}{\mu_0^{(+)}{}^1/\mu_0^{(-)}{}^1} \right) \quad (2) \\
 & + \exp(i2k_{1z} (d_1 - d_0)) \frac{\mu_1^{(+)}{}^2}{\mu_1^{(-)}{}^2} \left(1 - \frac{\mu_1^{(+)}{}^2/\mu_1^{(-)}{}^2 - \mu_1^{(-)}{}^2/\mu_1^{(+)}{}^2}{\mu_1^{(+)}{}^2/\mu_1^{(-)}{}^2} \right) \\
 & + \dots + \exp(i2k_{nz} (d_n - d_{n-1})) \frac{\mu_n^{(-)}{}^t}{\mu_n^{(+)}{}^t} \dots
 \end{aligned}$$

where

$$\mu_i^{(\pm)}{}^{i+1} = \frac{\mu_{i+1}}{\mu_i} \pm \frac{k_{(i+1)z}}{k_{iz}} \quad (2a)$$

k_{iz} is the z -component of the wave vector in the i^{th} layer,

n is the number of layers, and t denotes the last region which is semi-infinite. The properties of the i^{th} layer are completely general and are given as the complex permittivity ϵ_i and the complex permeability μ_i .

In the following sections we use the Fast Fourier Transform (FFT) to evaluate the integral for typical models. We then compare the results obtained by means of the FFT with the results based on Simpson's rule, the geometrical optics approximation and mode analysis. First though, we note a few preliminary observations with regard to the integral: (a) The singularity at $k_\rho = 0$ in the Hankel function is a removable singularity. (b) The reflection coefficient is an even function of k_ρ . The Hankel function can be changed into a Bessel function and the range of integration can also be changed to $0 - \infty$. The integral becomes

$$H_z = \int_0^\infty dk_\rho \, i \frac{I_0}{4\pi} \frac{k_\rho^2}{k_z} (1 + R^{\text{TE}}) e^{ik_z z} J_1(k_\rho \rho) \sin\phi \quad (3)$$

- (c) As $k_\rho \rightarrow \infty$, $R^{\text{TE}} \rightarrow 0$ and $\exp(ik_z z)$ also tends to 0.
- (d) The Bessel function oscillates rapidly for large arguments. The integrand will converge rapidly if we choose $z \neq 0$. Physically, this choice corresponds to the observation point being above the free surface of the stratified medium.
- (e) The integrand may possess branch points, poles, and other singularities along the axis of integration. One can eliminate the mathematical difficulties caused by these singularities by either of two devices--move these singularities away from the real axis by setting loss tangents of the media not equal to zero or deform the path of integration a small distance away from the real axis on the complex k_ρ -plane.

III. Integration by Fast Fourier Transform Method

Separate the integral (1) into two parts I_1 and I_2 . The first part corresponds to solutions in the absence of any stratified medium, and the result is given by the identity

$$I_1 = \frac{\partial}{\partial \rho} \left(\frac{e^{ikr}}{r} \right) = \frac{-i}{2} \int_{-\infty}^{\infty} \frac{k_{\rho}^2}{k_z} e^{ik_z z} H_1^{(1)}(k_{\rho} \rho) dk_{\rho} \quad (4)$$

$$\text{where } r = \sqrt{\rho^2 + z^2}$$

The second part includes all effects due to the reflection coefficient R^{TE} and after changing to Bessel functions,

$$I_2 = \int_0^{\infty} dk_{\rho} \frac{i I_0 k_{\rho}^2}{4 \pi k_z} R^{\text{TE}} e^{ik_z z} J_1(k_{\rho} \rho) \sin \phi \quad (5)$$

which is the integral that we want to solve with the FFT.

In applying the FFT, we use the formula (Gradshteyn and Ryzhik, 1965)

$$\int_0^{\infty} e^{-\nu k_{\rho}} J_1(k_{\rho} \rho) dk_{\rho} = \frac{1}{\rho} \left(1 - \frac{\nu}{\sqrt{\nu^2 + \rho^2}} \right) \quad (6)$$

$$\nu = \nu_R + i\nu_I, \quad \text{Re} \{ \nu + i\rho \} > 0$$

The integral is written in the following form

$$I_2 = \int_0^{\infty} dk_{\rho} g(k_{\rho}) e^{-\nu_R k_{\rho}} J_1(k_{\rho} \rho) \quad (7)$$

where

$$g(k_\rho) = i \frac{I \ell}{4\pi} \frac{k_\rho^2}{k_z} R^{TE} e^{ik_z z} + v_R k_\rho \quad (8)$$

We can write (Cooley, 1967) for $\Delta k_\rho = 1/2F$ where F is the Nyquist frequency

$$g(k_\rho) = \frac{1}{N\Delta k_\rho} \sum_{n=-\frac{N}{2}}^{\frac{N}{2}-1} a(f) e^{i2\pi f k_\rho} \text{ for } 0 < k_\rho < (\frac{N}{2} - 1)\Delta k_\rho \quad (9)$$

where

$$a(f) = \int_{-\infty}^{\infty} g(k_\rho) e^{-2\pi i f k_\rho} dk_\rho$$

$$f = n/N\Delta k_\rho$$

The proper choice of N , the number of samples, is essential for the best performance of the FFT and should be some integral power of two (i.e. $2^1, 2^2, 2^3$, etc.).

The factor $-2\pi f$ corresponds to v_I in Equation (6). The right hand side of (9) is periodic and does not tend to zero at ∞ . We can multiply (9) by $\exp(-v_R k_\rho)$ so that the right hand side of (9) is sufficiently small for the range of k_ρ between $(\frac{N}{2} - 1)\Delta k_\rho$ and ∞ . Then the final solution becomes, in view of the identity (6)

$$I_2 = \frac{1}{N\Delta k_\rho} \sum_{n=-N/2}^{\frac{N}{2}-1} a\left(\frac{n}{N\Delta k_\rho}\right) \frac{1}{\rho} \left[1 - \left(v_R - \frac{i2\pi n}{N\Delta k_\rho} \right) / \sqrt{\left(v_R - \frac{i2\pi n}{N\Delta k_\rho} \right)^2 + \rho^2} \right] \quad (10)$$

In choosing the increment Δk_ρ , we recall the two alternatives suggested in Section II. If we make the upper half space slightly conductive, which corresponds to $\text{Im } k \neq 0$, then we choose Δk_ρ to be smaller than the distance of the branch point from the real axis on the complex k_ρ -plane. If we insist on a real k , then we choose Δk_ρ such that one of the data points coincides with the branch point and such that Δk_ρ is smaller than the distance of the pole or branch point closest to the real axis on the complex k_ρ -plane.

To calculate the expansion coefficient a in Equation (9) we use the FFT algorithm in a subroutine which, for a given set of data d_k , returns the result

$$T_j = \sum_{n=0}^{N-1} d_k e^{-i \frac{2\pi j n}{N}} \quad j = 0, 1, \dots, N-1 \quad (11)$$

We first alias the function $g(k_\rho)$ with period $N\Delta k_\rho$ and denote the aliased version by $g_p(k_\rho)$. The subroutine requires data points of $g_p(k_\rho)$ between 0 and $(N-1)\Delta k_\rho$. Note that the function $g_p(k_\rho)$ is equal to $g(k_\rho)$ between 0 and $(N/2-1)\Delta k_\rho$ but $g_p(k_\rho)$ between $(\frac{N}{2}-1)\Delta k_\rho$ and $(N-1)\Delta k_\rho$ is equal to $g(k_\rho)$ between $-(N/2)\Delta k_\rho$ and $-\Delta k_\rho$. In the subroutine we calculate

$$a_p\left(\frac{n}{N\Delta k_\rho}\right) = \Delta k_\rho \sum_{\ell=0}^{N-1} g_p(\ell\Delta k_\rho) e^{-i2\pi\ell n/N} \quad n = 0, 1, \dots, N-1 \quad (12)$$

and return the aliased version of $a(n/N\Delta k_\rho)$, $a_p(n/N\Delta k_\rho)$. We must be careful in translating from $a_p(n/N\Delta k_\rho)$ to $a(n/N\Delta k_\rho)$ within the limits $-\frac{1}{2\Delta k_\rho}$ to $\frac{1}{2\Delta k_\rho}$ in order to use the result (10).

We must choose $N\Delta k_\rho$ such that the function $g(k_\rho)$ is sufficiently near zero outside the limits $-N\Delta k_\rho/2$ to $N\Delta k_\rho/2$. Although mathematically, we could choose z to be large, its value is predetermined by the experimental arrangement. v_R must not be too small. Note that v_R must be greater than zero but cannot be larger than z or the exponent in (8) will cause $g(k_\rho)$ to diverge. We choose $v_R = z/2$.

In Figures 1 and 2, we show the interference patterns for H_2 calculated with FFT on the IBM 360/65 computer for a three layer and a six layer case, respectively. The height of the observation point was taken to be 2 meters, the height used in the lunar experiment. The computation time was about 2.5 minutes for each case. These results are to be compared with the results obtained with Simpson's rule and shown also in Figures 1 and 2.

IV. Integration by Simpson's Rule

Evaluation of the integral (1) by Simpson's rule was discussed by Kong, Tsang, and Simmons (1974). In applying the Simpson's rule for integration, the integration intervals are divided into small increments Δk_ρ . The criterion for the choice of the increment depends on the rate of oscillation of the Bessel function. We choose Δk_ρ as small as 0.1 radian. Thus when $\rho = 20\lambda_0$ and the frequency is 32 MHz, we have $\Delta k_\rho \approx 0.0005$. We stop computation when the absolute amplitudes of the integrand become less than 0.2 % of the accumulative value for the integral.

Note that the error term in Simpson's rule is given by $n(\Delta k_\rho)^5/90$ times the fourth derivative of the integrand. The presence of the branch point due to k_z at $k_\rho = k$ will invalidate the integration even in the simple case of $R^{TE} = 0$, if one integrates along the real axis. We choose to keep k real and to deform the path to the Sommerfeld path of integration. Subroutines for Bessel functions of complex arguments are constructed. For small arguments, we use a power series representation, and for large arguments, we use asymptotic expansions for the Bessel functions. The subroutines have been checked against tables of Bessel functions.

The computation is very time consuming. However, the convergence of the integrand will be very fast if the observation point is far above ground, i.e., for a large positive value of z . Note also that the magnitude of Δk_ρ is inversely proportional to ρ . Thus the computation takes

less time for regions near the transmitting dipole, where, in fact, most computational methods that use asymptotic expansion are invalid.

V. Discussion

The magnitude of H_z for the three layer case and for the six layer case, calculated by FFT and by Simpsons rule are shown in Figures 1 and 2 for comparison. We conclude that both techniques yield identical results. Computation times are very different though - Simpsons rule used 32 minutes for the three layer case and about 40 minutes for the six layer case on an IBM 360/65 computer which is to be compared with 2.5 minutes for each FFT calculation. Another possible consideration for some applications may be the fact that the FFT consumes large amounts of storage space in the computer when the Nyquist frequency and the number of sampling points are large. Also, the comparisons have been made for ranges that are unfavorable to Simpson's rule.

Further substantiation that our FFT formulation is correct can be obtained by comparison of FFT-results for a two layer model with results obtained with both the geometrical optics approximation and mode analysis. See Figure 3. Note that the curves have been displaced 20db so they can be seen more easily. Because the features of the FFT-results are also present in the results of both mode and geometric optics approximation (within the range of validity), we conclude that the FFT formulation is correct. We note briefly though that other factors are sometimes important in the choice of a computational technique. The analytical methods consume very little

time, but they are applicable only in certain regions because of the approximations involved. The geometrical optics result applies when the distance is far from the transmitting antenna (ideally, greater than about $5-10 \lambda_0$) and when the layer is thick and lossy. The mode method can be applied to general cases, and is extremely useful for thin layers. Tsang et al. (1973) discussed the geometrical optics approximation in greater detail. See Kong et al. (1974) for a complete discussion of mode analysis applied to electromagnetic wave propagation in layered media.

Acknowledgement

This work was supported by NASA Contract No. NAS9-11540 through the Center for Space Research, Massachusetts Institute of Technology. We would like to thank Norman Brenner for the use of his FFT subroutine algorithm.

References

- Annan, A.P., Radio Interferometry depth sounding: Part I - Theoretical discussion, Geophysics, vol. 38, 557, 1973.
- Cooley, J.W., P.A.W. Lewis, and P.D. Welch, Application of the Fast Fourier Transform to computation of Fourier integrals, Fourier series, and convolution integrals, IEEE Trans. on Audio and Electroacoustics, AU-15, 79, 1967.
- Gradshteyn, I.S., and I.W. Ryshik, Tables of Integrals Series and Products, p. 707, Academic Press, New York, 1965.
- Kong, J.A., Electromagnetic fields due to dipole antennas over stratified anisotropic media, Geophysics, 37, 985, 1972.
- Kong, J.A., L. Tsang, and G. Simmons, Lunar subsurface probing with radio frequency interferometry, IEEE Trans. on Ant. and Prop., in Press, 1974.
- Rossiter, J.R., G.A. LaTorraca, A.P. Annan, D.W. Strangway, and G. Simmons, Radio interferometry depth sounding: Part II - Experimental results, Geophysics, v. 38, 581, 1973.
- Simmons, G., D.W. Strangway, L. Bannister, R. Baker, D. Cubley, G. LaTorraca, and R. Watts, The Surface Electrical Properties Experiment, Lunar Geophysics, Z. Kopal and D. Strangway (eds) D. Reidel Publishing Co., 258, 1972.
- Simmons, G., D. Strangway, P. Annan, R. Baker, L. Bannister, R. Brown, W. Cooper, D. Cubley, J. deBettencourt, A.W. England, J. Groener, J.A. Kong, G. LaTorraca, J. Meyer, V. Nanda, D. Redman, J. Rossiter, L. Tsang, J. Urner, and R. Watts, Apollo 17 Preliminary Science Report, NASA, in Press, 1974.

Strangway, D.W., G. Simmons, R. Watts, G. LaTorraca, L.
Bannister, R. Baker, J.E. Redman, and J.R. Rossiter,
Radio frequency interferometry-- A new technique for
studying glaciers, in Press, J. Glaciology, v. 13,
N. 67, April 1974.

Tsang, L., J.A. Kong, and G. Simmons, Interference patterns
of a horizontal electric dipole over layered dielectric
media, J. Geophys. Res., V. 78, N. 17, 3287, 1973.

FIGURE CAPTIONS

Figure 1. Comparison of the direct and FFT methods for a three layer model in which

$$\epsilon_1 = (3.3)(1 + i0.01)\epsilon_0 \quad d_1 = 1\lambda_0$$

$$\epsilon_2 = (5.0)(1 + i0.02)\epsilon_0 \quad d_2 = 2\lambda_0$$

$$\epsilon_3 = (8.0)(1 + i0.04)\epsilon_0$$

Vertical scale is 10 db per division. The curves have been displaced vertically 20 db for ease of comparison.

Figure 2. Comparison of the direct and FFT methods for a six layer model in which

$$\epsilon_1 = (2.0)(1 + i0.01)\epsilon_0 \quad d_1 = 0.5\lambda_0$$

$$\epsilon_2 = (3.0)(1 + i0.02)\epsilon_0 \quad d_2 = 1\lambda_0$$

$$\epsilon_3 = (4.0)(1 + i0.03)\epsilon_0 \quad d_3 = 2\lambda_0$$

$$\epsilon_4 = (5.0)(1 + i0.04)\epsilon_0 \quad d_4 = 3\lambda_0$$

$$\epsilon_5 = (6.0)(1 + i0.05)\epsilon_0 \quad d_5 = 4\lambda_0$$

$$\epsilon_t = (8.0)(1 + i0.06)\epsilon_0$$

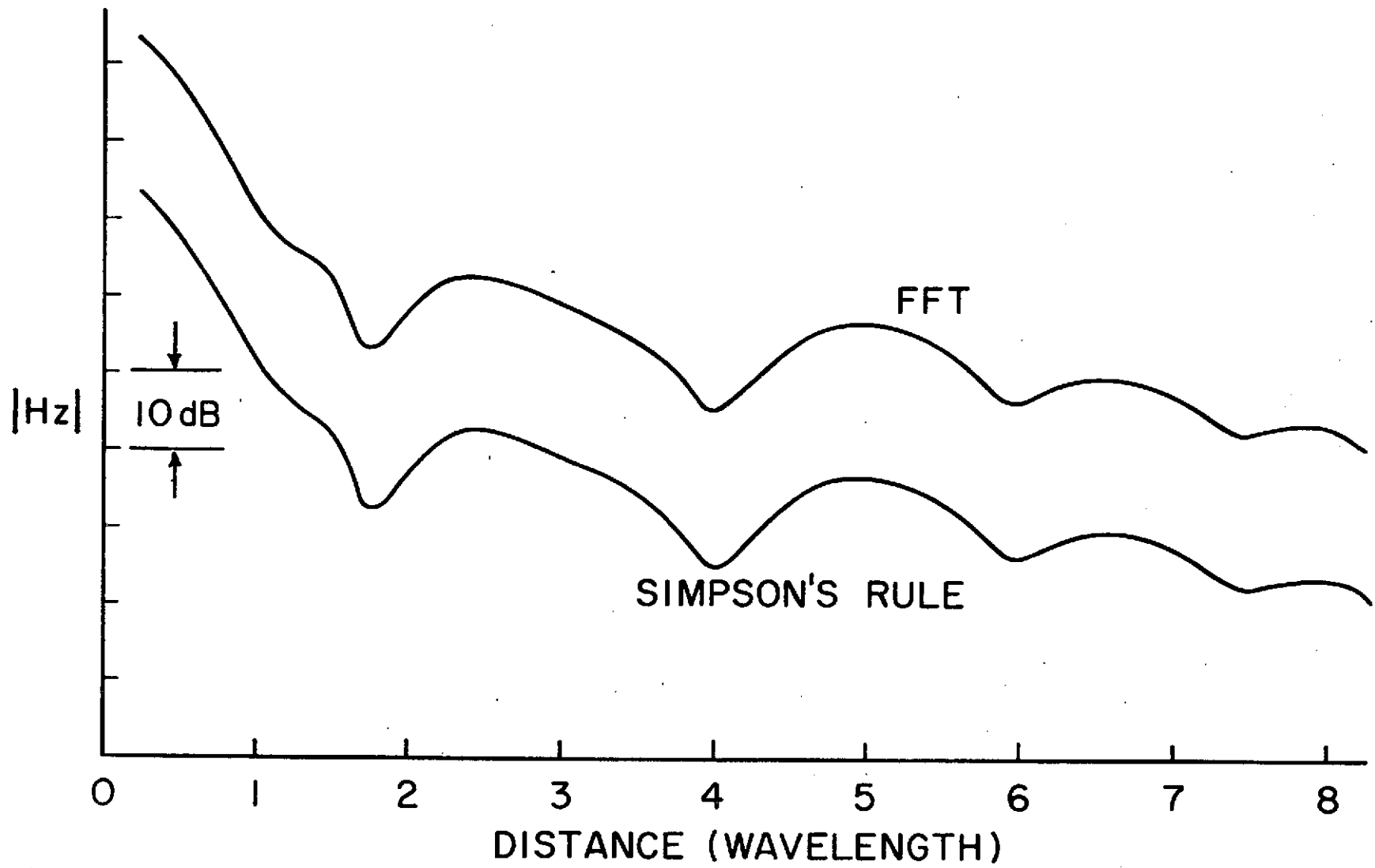
Vertical scale is 10 db per division. The curves have been displaced vertically 20 db for ease of comparison.

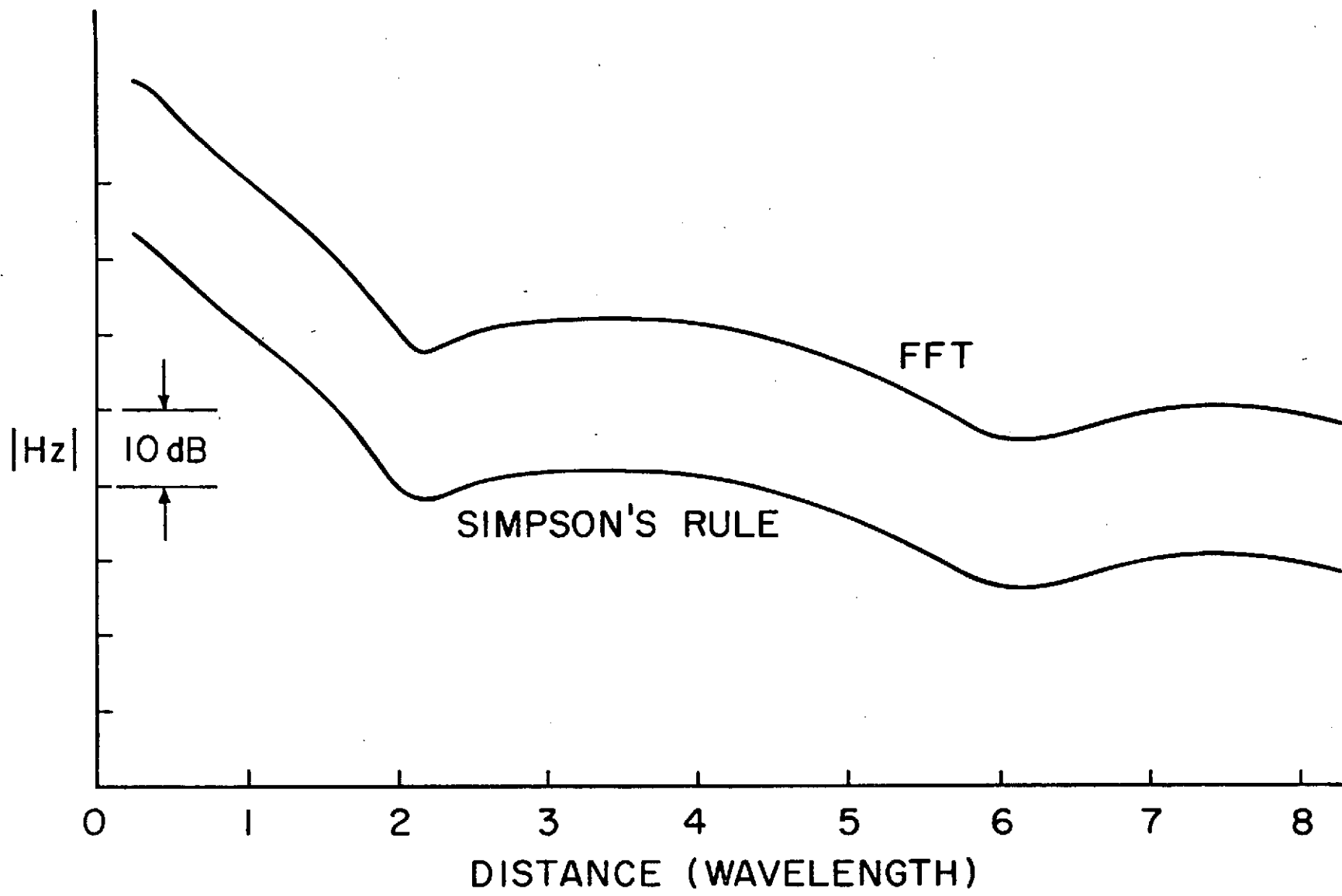
Figure 3. Comparison of the FFT, Geometrical Optics (GOA), and Mode Theory (MODE) for a two layer model in which

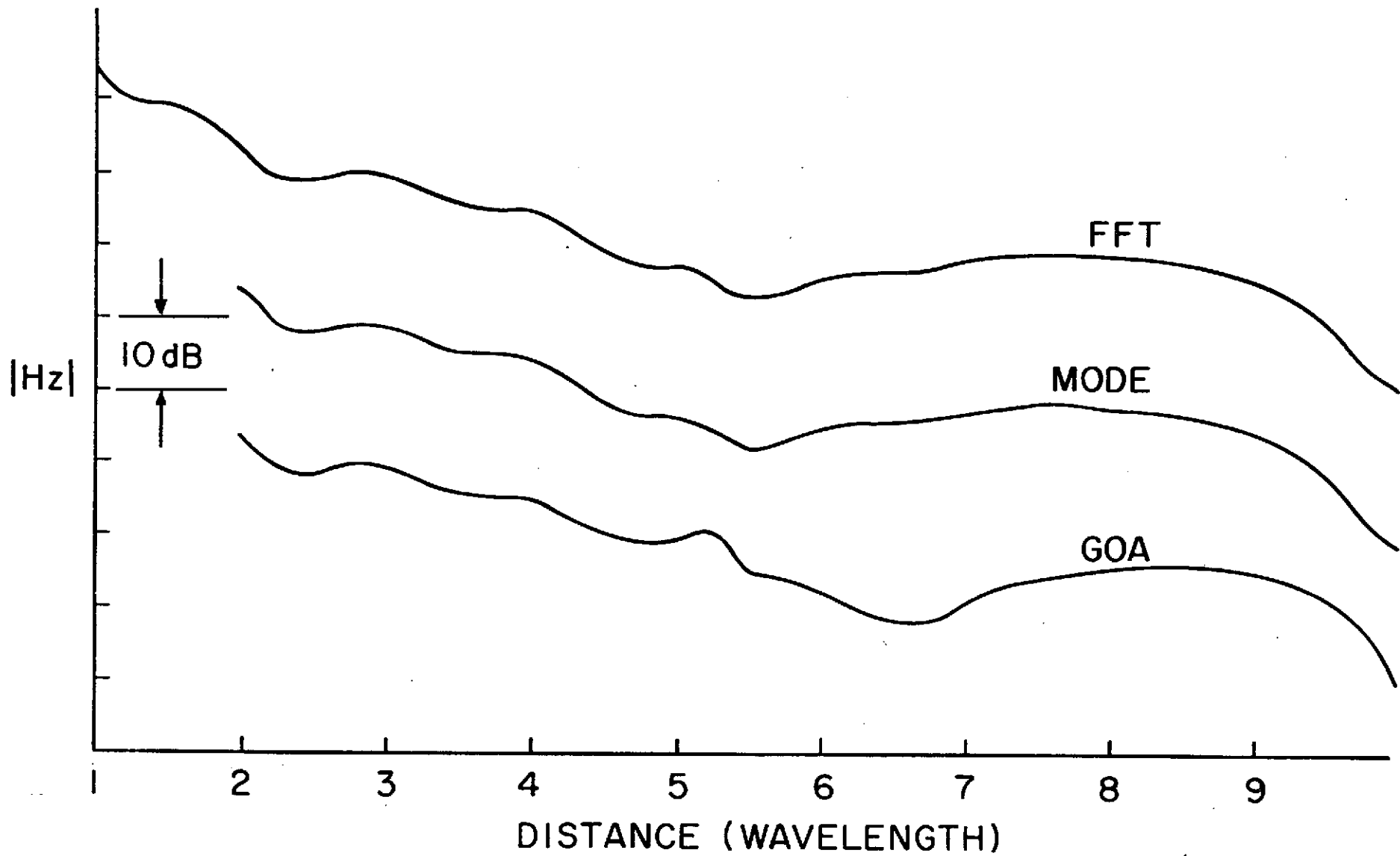
$$\epsilon_1 = 3.3(1 + i0.02)\epsilon_0 \quad d_1 = 4\lambda_0$$

$$\epsilon_t = 6.0(1 + i0.04)\epsilon_0$$

Vertical scale is 10 db per division. The curves have been displaced vertically 20 db for ease of comparison.







The Electromagnetic Response of a Low-loss,
2 Layer, Dielectric Earth for Horizontal
Electric Dipole Excitation.

A.P. Annan¹, W.M. Waller², D.W. Strangway³,
J.R. Rossiter¹, J.D. Redman³.

1. Department of Physics
University of Toronto
Toronto, Ontario
Canada
2. Lockheed Electronics Company
NASA - JSC, Houston
Texas, U.S.A.
3. Department of Geology
University of Toronto
Toronto, Ontario
Canada

Abstract

This paper presents the results of a concentrated theoretical and experimental study into the electromagnetic response of a 2-layer dielectric earth. The side by side analysis of the theoretical response and the results of a scale model experiment demonstrates the fundamental features of electromagnetic wave propagation in such an environment. For layers thick on a wavelength scale the response is readily interpreted from a geometrical optics analysis. For thin layers, the response is best analysed from the normal mode viewpoint. The responses for both depth extremes as well as intermediate depths are presented and interpretations of the observations given. The onset of mode propagation in the model data is very distinctive.

Introduction

The radio interferometry method, previously summarized by Annan (1973) and Rossiter et al (1973), is a useful geophysical method in geologic regions exhibiting extremely high electrical resistivities. In this context, high resistivity implies that displacement currents in the media must be considerably greater than the conduction currents. In terrestrial materials, this situation is encountered in ice-covered regions (glaciers, polar ice caps) for radio frequencies of the order of 1Mhz. and higher. Lunar materials

also behave as low-loss dielectric materials in the Mhz. frequency range (Olhoeft ^{et al} (1973), Katsube and Collett (1971)).

The original papers, mentioned above, presented much of the preliminary work conducted to study the feasibility of the radio interferometry method. Subsequent to this work, a lunar experiment was designed, constructed and carried on Apollo 17 (Simmons et al (1972)). In order to be able to make a coherent interpretation of data from glaciers and the Moon, a much more detailed understanding of the basic features of the radio interferometry method was required. An in-depth computational analysis of the theoretical response of idealized models was made and these responses were simulated with a scale model experiment to check their validity. In addition, full scale experiments were conducted on glaciers in Alberta (Strangway et al (1974) and in Alaska (Rossiter et al ^{see companion paper}).

In this paper, a subset of the theoretical and scale model studies are analysed. The purpose is to present a detailed, documented study of the response of a 2-layer, low-loss dielectric earth for excitation by an electric dipole antenna laid on the surface. Some preliminary results of the scale model and theoretical analysis are given by Rossiter et al (1973). In the course of this study, the theoretical and experimental work were carried out together in order that each could be used to confirm the other. The end product was an in-depth understanding of the intuitively simple, but complex in detail, physical phenomena involved.

Idealized 2-Layer Earth

The idealized model studied is shown in Fig. 1. The 2-layer earth is characterized by the dielectric constants K_i and the loss tangents $\tan \delta_i$. The cartesian coordinates (x_1, x_2, x_3) , the associated unit vectors $(\hat{e}_1, \hat{e}_2, \hat{e}_3)$ and the cylindrical coordinates (ρ, ϕ, z) are shown in the diagram. For the computational analysis, the earth is excited by a point electric dipole located at the origin of the coordinate system with its moment aligned with the \hat{e}_1 axis. In actual experiments, the source is a half wavelength electric dipole antenna. The time variation of the dipole moment is of the form $e^{-j\omega t}$ and in all subsequent mathematical expressions the time dependence is suppressed.

The radio interferometry method measures the field strength about the transmitter primarily along profiles which run radially outward from the dipole. The profiles commonly used are denoted the broadside (B) and the endfire (E) profiles. The B profile is run radially out from the dipole normal to the direction of the dipole moment. The E profile runs radially away from the dipole along the direction of the dipole moment. In Fig. 1, the B profile is along the \hat{e}_2 axis while the E profile is along the \hat{e}_1 axis. The field strength along these profiles exhibits maxima and minima at various spatial positions due to interference of waves propagating

with different horizontal phase velocities. The position of these maxima and minima and the rate of decay of the fields with distance are indicators which can be used to infer the electrical properties of the earth and the layer thickness.

In the following discussions, all spatial dimensions are normalized in terms of the free space wavelength w . All propagation constants and wavenumbers are normalized in terms of the free space propagation constant $k_0 = 2\pi/w$.

Mathematical Formalism

The mathematical formulation of the electromagnetic response of a plane layered earth is well known since it is a standard boundary value problem (Wait (1970), Brekhovskikh(1960)). The difficult part of the analysis occurs when actual numerical computations of the response are required. The fields are expressed as Hankel transforms (or 2 dimensional Fourier transforms) which cannot be evaluated analytically. In all but the simplest case of a whole-space, approximate methods of integration must be used^{to} extract useable results. The most straight forward method of obtaining numerical results is to numerically integrate the Hankel transforms. Other methods involve limiting material properties to special values and reducing the integrand to a sufficiently simple form that an analytical evaluation can be made. The other alternative^{to} is^{to} look at the physical nature of the response by

approximate solutions which can be obtained by manipulation of the integration contour in the complex plane. Two solutions in this class are known ^{as the} geometrical optics and the normal mode solutions.

The details of the applications of these techniques to low-loss dielectric earth models is discussed by Annan (1970, 1973), Tsang et al (1973) for various dipolar excitations. In the following discussions, the geometrical optics and the normal mode solutions are used. The reason for this is that sufficiently accurate results can be obtained in a very economical manner. The computation cost of numerical integration rules out this method for all but very particular cases under consideration. Of the two solutions obtained by contour integration, the normal mode solution is the more correct solution. The only approximations involved here are in the analysis of the branch line contributions which yield lateral and inhomogeneous waves associated with the boundaries. The actual "normal mode" part of the solution is exact within the computational error of evaluating its contribution. The geometrical optics ^{solution} involves asymptotic expansions for each multiple reflection and has built in approximations from the first step of analysis. The main advantage of the geometrical optics solution is that the response has a simple physical interpretation and is economically computed. As pointed out by Annan (1973), this solution can only be used when spatial dimensions are on the order of the wavelengths or attenuation lengths in the media involved.

The electric and magnetic fields at the surface of the 2 layer earth shown in Fig. 1 are summarized in Table 1. The complex radial wavenumber plane and integration contours are shown in Fig. 2. For the expressions in Table 1, the geometrical optics solution is obtained by expanding the expression in the denominators

$$\frac{1}{1 - R_+ R_- \beta} = \sum_{n=0}^{\infty} R_+^n R_-^n \beta^n \quad (1)$$

whereas the mode solution is obtained by solving the transcendental equation

$$R_+ R_- \beta = 1 \quad (2)$$

which yields the TE and TM normal mode wavenumbers of the layered earth. The contour of integration is deformed into a steepest descent contour through a saddle point for each term in the geometrical optics expansion. For the normal mode analysis, the contour is deformed to yield a sum over the normal modes of the system plus integrals along the branch lines.

Scale Model Description

For electromagnetic systems to be similar, the spatial dimensions in free space wavelengths and the loss tangents must be the same. In order to simulate the radio interferometry method in a reasonably sized laboratory, wavelengths

in the centimeter range are necessary; this corresponds to radio frequencies in the GHz range. The 2 layer earth model and associated electronics are shown in Fig. 3 and 4.

The transmitting (TX) and receiving (RX) antennas are tuned half-wavelength electric dipoles. The excitation frequency is 5.9 GHz. which corresponds to a free space wavelength $w = 5.08$ cm. The 2 layer earth is simulated by a tank of dielectric oil with a plane reflector suspended at a depth d in the oil. The effects of the finite size of the tank (30w long x 15w wide x 15w deep at 5.9 GHz) are minimized by lining the inside with a microwave absorbing materials (Eccosorb). This reduces undesired spurious reflections from the walls of the tank. The Tx and Rx antennas are mounted on a track suspended over the tank; the Rx antenna is mounted on a mechanized carriage so that ^{of field strength} profiles versus Tx-Rx separation can be made automatically. The track and associated supports are also covered with microwave absorbing material.

Three sets of electrical properties of the 2-layer models were used in the model. The first set was an oil with dielectric constant $K_1 = 2.16$ and $\tan \delta_1 = 0.0022$, and an aluminum sheet, $\tan \delta_2 = \infty$, acting as a perfectly reflecting substratum. A second set of electrical properties were obtained by doping the oil with benzonitrile to increase its loss tangent. The third layered consisted of oil

(undoped) underlain by a dielectric slab $K_2 = 6.75$ and $\tan \delta_2 = 0.11$. The slab was $2w$ thick and had a sufficiently high loss that it eliminated the possibility of spurious reflections from the bottom of the slab returning to the surface. The thickness of the oil layer was varied from $0.2w$ up to $10w$ and profiles of $\log_{10} |E_\phi|$ versus Tx-Rx separation along the B profile were measured in most instances.

The automatic traverse equipment and associated recording apparatus are sketched in Fig. 4 (Waller (1973)). The field strength versus distance ^{is} displayed on an X-Y recorder and at the same time can be recorded on a two channel analog tape recorder. The recorded data was later digitized in order that data enhancement and automatic interpretation schemes could be tested.

Theoretical and Experimental Results

(a) Half Space Earth: Radiation Pattern Directionality

Before discussing the 2 layer earth in detail the half-space response is briefly reviewed. The interaction of the dipole source with the air-earth interface drastically modifies the directionality of the antenna. This result is important when analysing 2 layer models with the geometrical optics solution. This effect has been discussed by Tsang et al (1973), Annan (1970, 1973), Cooper (1971). The pattern

for E_{ϕ} in the X_2X_3 plane is sketched in Fig. 5; (a) shows E_{ϕ} for the dipole in a whole-space while (b) shows the response of the dipole when placed on a perfectly dielectric half-space. E_{ϕ} in the X_2-X_3 plane for the whole-space is simply given by

$$E_{\phi} = j \omega \mu_0 |d| \frac{e^{j 2\pi R}}{4\pi R W} \quad (3)$$

while for the half space, as $R \rightarrow \infty$,

$$\begin{aligned} E_{\phi} &= T_{10} \left(\frac{|z|}{R} \right) j \omega \mu_0 |d| \frac{e^{j 2\pi R}}{4 R W} & z > 0 \\ E_{\phi} &= T_{01} \left(\frac{|z|}{R} \right) j \omega \mu_0 |d| \frac{e^{j 2\pi \sqrt{K_1^*} R}}{4 R W} & z < 0 \end{aligned} \quad (4)$$

where

$$R = \left(\sum_{i=1}^3 (x_i)^2 \right)^{1/2}$$

$|d|$ = electric dipole moment

μ_0 = free-space permeability

$$n_{ij} = (K_i/K_j)^{1/2}$$

$T(\alpha)$ = TE Fresnel transmission coefficient from region
i to region j.

$$= \frac{2 \alpha}{\alpha + n_{ji} (1 - n_{ij}^2 (1 - \alpha^2))^{1/2}}$$

The modified pattern is highly directional with a strong peak into the earth at the critical angle of the interface. Similar analyses can be carried out for other field components; all show highly directional patterns.

Experimental measurements of the radiation pattern obtained with the scale model with no subsurface reflector confirm the directionality of the source^{in the presence of an interface.} The results of measurements of $|E_{\theta}|$ are shown in Fig. 6. The pattern for E_{θ} was measured at distances of $3w$, $4.5w$, and $6w$ from the source. The "theoretical" pattern for the air-oil-dipole configuration computed by Cooper (1971) is shown with the experimental results. It should be noted that the experimental results are not normalized and that the shape of the patterns, not the magnitudes, should be considered.

The discrepancy between the theoretical response and observed response are primarily explained by the fact that the experimental measurements were made at a finite distance from the source. The theoretical pattern shown is valid only infinitely far from the source by definition. As the Tx-Rx separation is increased, the experimental pattern changes shape and becomes more like the theoretically predicted pattern.

The preceding solution for the theoretical response is obtained from the first term in an asymptotic expansion for the field. At finite source-receiver distances higher order terms in the expansion must become important. At the peak of the pattern, however, alternate solutions must be used since the higher terms of the asymptotic expansion are infinite. Brekhovskikh (1960) has studied the fields in the region of the peak of the pattern in detail and obtained a modified expansion with the first correction term decreasing as $(1/r)^{5/4}$. A rough calculation shows that this term is significant out to distances of tens of wavelengths.

The physical rationale for the lobate pattern is quite simple. The explanation can be seen most easily if the waves radiated by the antenna are examined from the ray theory point of view. In a whole space the source radiates uniformly in all directions. The presence of the half-space modifies this, since rays which propagate horizontally are continually refracted downward at the critical angle of the interface. Combining the whole-space pattern of the antenna with the directional selectivity of the interface yields a complex radiation pattern with high directionality.

To first order, the fields along the interface are zero. If higher terms of the asymptotic expansions are retained, the fields fall off as $(1/r)^2$. There are two components in this second order effect; one which propagates with the phase velocity of the earth and one which travels with the phase velocity of the air. As a result the fields at the surface of the half-space exhibit a regular beating as a function of spatial distance from the antenna. This is discussed by Annan (1970, 1973).

(b) 2 Layer Earth: Perfectly Reflecting Substratum

The 2 layer earth can exhibit a wide variety of responses depending upon the range of electrical properties and layer thickness. In early analysis, the case of a perfectly reflecting substratum was considered as a starting point. In order to demonstrate the general character of the 2 layer earth, a suite^{of} responses for various values of d and a perfectly reflecting substratum obtained with the scale model and computed theoretically using both the normal mode and geometrical optics solution are shown in Fig. 7. The layer thickness ranges from $0.5w$ to 7 . The E_{θ} field strengths in decibels are plotted versus transmitter receiver separation in free-space wavelengths along the B profile. The scale model response is shown along^{with} the mode and geometrical optics solution. The geometrical optics curve is shifted upward from the

experimental curve while the mode solution is shifted downward. This offset of the curves is used to minimize the overlap of the various responses which tends to confuse the visual presentation of the data.

The results in Fig. 7 span most of the important depth ranges and demonstrate most of the features of the 2 layer response. For the shallow depths of $0.5w$, $1.0w$, and $1.5w$, the fields are expressible in terms of one, two, or three guided modes plus the lateral and inhomogeneous waves given by branch line contributions (see Appendix). The fields decay with distance as $(1/r)^{1/2}$ and exhibit a regular beating as the modes move in and out of phase. For $d = 0.5w$, only one mode is guided and the only interference occurs near the source where the branchline and modal contributions are comparable in magnitude. The remainder of the infinite sequence of modes are either not excited or are leaky modes which decay exponentially with distance from the transmitter. As the depth increases more and more modes move into the guided regime and the field strength versus distance becomes more complicated as the various modes move in and out of phase.

Examination of the theoretical responses show that the geometrical optics solution and the model response are in good agreement for layer thicknesses greater than $3.0w$. For shallower depths, the experimental and theoretical

responses diverge from one another. The breakdown in the geometrical optics solution is to be expected from its asymptotic nature. The normal mode solution, however, shows excellent agreement at the shallow depths and becomes the same as the geometrical optics solution at the larger depths.

(c) Thin Layers and Critical Depths

The preceding discussion of the 2-layer earth with a perfectly reflecting substratum illustrates the general nature of the response. At very shallow depths and at various critical depths, the response changes quite drastically with layer thickness. A suite of curves for depths $d < 0.2w$ to $d > 0.8w$ at various depth increments show this behaviour clearly. The critical depths Λ for the ^{in wavelengths} model ^{electrical properties} are given by $d_c = 0.23 (2n + 1) \Lambda$ (TE modes) and $d_c = 0.46n \Lambda$ (TM modes), $n = 0, 1, 2 \dots$ (see Appendix). For $d < 0.23$, (E_θ is composed of TE modes only on B profile), no normal modes are excited since the layer is too thin. As a result, the fields versus distance are described totally by the branchline integrals and fall off as $(\frac{1}{r})^2$. As d increases past 0.23 the first normal mode moves into the guided regime and the field strength versus distance falls off as $(\frac{1}{r})^{1/2}$. The field strength versus distance varies only slightly with depth changes until $d \rightarrow 0.69$.

As $d \rightarrow 0.69$, the field strength versus distance begins to show a weak beating. For d just greater than 0.69, the fields show very deep interference nulls at regular spacing. Two guided modes (TE) are now propagating in the layer for $0.69 < d < 1.16$, the profiles exhibit the regular beating; however, the maxima and minima locations are very sensitive to the layer thickness. As $d \rightarrow 1.16$, the same behaviour as $d \rightarrow 0.69$ is seen and a third normal mode moves from the leaky to the guided regime. (see Appendix.)

The theoretical responses computed by the normal mode method are shown along with experimental results. The mode solutions match the experiment results very well except at the critical depths. At the critical depths, two poles and a branch point merge together in the mathematical solution. The branchline contribution is evaluated approximately by steepest descent integration; the approximate solution fails at the critical depth_A^S. The results of evaluating the branchline contribution by numerical integration are also shown on the profiles. The agreement between experiment and theory is much better at the critical depths with this improvement.

(d) 2 Layer Earth; Dielectric Substratum

The response of a dielectric substratum is not greatly different from the previous responses for a perfectly reflecting substratum. The major difference is that there

are no longer any unattended guided modes; all the modes are leaky since energy can always leak out of the layer into the substratum. As a result, the field shows the same basic behaviour but all responses have a strong attenuation with distance from the Tx.

The data collected with the scale model experiment are shown in Fig. 9. The experimental results are presented along with the theoretically (normal mode) computed responses. The results compare extremely well. (It should be noted that when the experimental field strength falls below the Rx sensitivity the field strength levels off at a constant value. This is noticeable at large distances from the Tx in all the dielectric bottom responses.) The normal modes no longer have a sharp onset as they do for a perfectly reflecting substratum. The modes now move from a very leaky regime to a much less leaky regime with no sharp dividing line present. This improves the accuracy of the theoretical solution since there are no true critical depths and the mathematical approximations in evaluating branchline contributions are greatly improved.

Summary and Conclusions

The results of theoretical and experimental^{work} have led to a clear understanding of the physical mechanisms of wave propagation in a 2 layered dielectric earth. This detailed

understanding of the waves propagations in such a system is necessary for the interpretation of radio interferometry data from geologic environments which can be simulated by a 2 layer model.

and limitations

The practical aspects of constructing scale model experiments at GHz. frequencies are well understood and the reliability of the model makes it an ideal method of examining problems which are not tractable from a theoretical point of view. With such excellent agreement between theory and experiments, the model can be applied analysing more complex problems with confidence.

The scale model has proved to be invaluable in checking out the computer programs which generate the theoretical responses. The mathematical formalism is very complex and its translation into a computational format is difficult; particularly when approximations are made in certain parts of the analysis.

The normal mode approach to analysing moderately to very thin layers has greatly improved the ability to interpret layered structures. The initial analysis of responses was made using the geometrical optics solutions which is invalid for thin layers. The model study confirming the mode analysis has already led to successful interpretation of radio interferometry data obtained in thin layer environments (Rossiter et al. ()).

see accompanying paper

Appendix

TE and TM Mode Critical Depths for a 2-Layer Earth

The radial wave numbers of the normal modes of a plane stratified 2 layer earth are obtained by solving the transcendental equations

$$\text{TE Mode} \quad 1 - R_+^{\text{TE}} R_-^{\text{TE}} e^{j2\pi d \gamma_1} = 0 \quad \text{A-1}$$

$$\text{TM Mode} \quad 1 - R_+^{\text{TM}} R_-^{\text{TM}} e^{j2\pi d \gamma_1} = 0 \quad \text{A-2}$$

The R_{\pm} are the Fresnel reflection coefficients indicated in Fig. A(a) and $\gamma_1 = (K_1 - \lambda^2)^{1/2}$ is the vertical component of the wave vector in the layer. For the dielectric media discussed here

$$R_{\pm}^{\text{TE}} = \frac{\gamma_1 - \gamma_{1\pm 1}}{\gamma_1 + \gamma_{1\pm 1}} \quad R_{\pm}^{\text{TM}} = \frac{\frac{K_2}{\gamma_2} - \frac{K_{1\pm 1}}{\gamma_{1\pm 1}}}{\frac{K_1}{\gamma_1} + \frac{K_{2\pm 1}}{\gamma_{2\pm 1}}} \quad \text{A-3}$$

In general the λ_p^{TE} and λ_p^{TM} are complex and A-1 and A-2 have no pure^{ly} real solutions. Only totally real λ_p^{TE} yield modes which are unattenuated radially.

True guided modes exist only when $|R_+| = |R_-| = 1$ which physically occurs only when the media are lossfree and region 1 is a low velocity region (i.e. $K_1 > K_0$ and K_2) and d is greater than a minimum critical thickness. Analysis of equations A-1 and A-2 in the complex λ plane show that the λ_p^{TE} must lie along a line which intertwines the various Riemann

surfaces defined by the branchlines of the $(K_1^* - \lambda^2)^{1/2}$ functions. The case of a perfectly dielectric slab ($\tan \delta_1 = 0$) overlying a perfectly reflecting ($\tan \delta_2 = \infty$) substratum is sketched in Fig. A(b). The roots of the transcendental equation lie on the ^{line indicated in A(b)} ~~the~~. The solid circles denote roots on the upper Riemann surface ($+ (K_1^* - \lambda^2)^{1/2}$ for branchlines shown) which are excited modes and the open circles indicate roots on the lower Riemann surfaces (any combination of signs for $(K_1^* - \lambda^2)^{1/2}$ other than +). The poles on the real axis between $\sqrt{K_0^*}$ and $\sqrt{K_1^*}$ are guided unattenuated modes while the poles $\lambda_p < \sqrt{K_0^*}$ are leaky modes and have a positive imaginary component.

The behaviour of the λ_p^{TE} with variations in d is twofold; the poles λ_p^{TM} move down the contours and are more closely packed as d increases and the contour, on which the poles lie, swings towards the imaginary axis. As the depth varies, a pair of the poles coincide with the $\sqrt{K_0^*}$ branchpoint at regular depth spacings. These depths are the critical depths for the modes and mark the depth where a mode moves from the leaky to the unattenuated or guided regime.

The critical depths for the case of the perfectly reflecting substratum are obtained by noting that

$$R_-^{\text{TE}} = R_-^{\text{TM}} = -1 \quad \text{A-4}$$

and that for $\lambda = \sqrt{K_0^*}$,

$$R_+^{\text{TE}} = 1 \quad R_+^{\text{TM}} = -1 \quad \text{A-5}$$

Substituting into A-1 and 2 yields.

$$\begin{aligned} \text{TE } d_c^n &= \frac{2n+1}{4(\kappa_0-1)^{1/2}} w \\ \text{TM } d_c^n &= \frac{n}{4(\kappa_1-1)^{1/2}} w \end{aligned} \quad n = 0, 1, 2, \dots \quad \text{A-6}$$

For finite loss tangents, and a dielectric bottom, the contours on which λ_p lie still pass through $\sqrt{\kappa_1}$ but are displaced away from the real λ axis between $\sqrt{\kappa_0}$ and $\sqrt{\kappa_1}$ so that all modes have a finite imaginary component which corresponds to attenuation with distance.

Acknowledgements

This research has been supported by NASA grant no. NAS 9-11540 for model construction and collection of model data and by the Canadian Department of Energy, Mines and Resources grant no. 1135-D13-4-16/73 for analysis and preparation of this manuscript. We wish to thank Mr. J. Proctor for his able assistance in the computational aspects of this work.

Bibliography

- Annan, A.P., 1973, Radio Interferometry Depth Sounding:
Part I - Theoretical Discussion, Geophysics, v. 30,
no. 3, p. 557-580.
- Annan, A.P., 1970, Radio Interferometry Depth Sounding, M.Sc.
Thesis, University of Toronto, Toronto, Ontario,
Canada.
- Brekhovskikh, L.M., 1960, Waves in Layered Media: New York,
Academic Press.
- Cooper, W.W., 1971, Patterns of Dipole Antenna on Stratified
Medium, Technical Report TR71-3, MIT Centre for Space
Research.
- Katsube, T.J., and Collett, L.S., 1971, Electrical properties
of Apollo 11 and 12 lunar samples, in Proceedings of
the Second Lunar Science Conference, Houston, Texas,
edited by A.A. Levinson: Cambridge, Mass. Inst. Tech.
- Olhoeft, G.R., Strangway, D.W., and Frisillo, A.L., 1973,
Lunar Sample Electrical Properties, Proc. Fourth
Lunar Sci. Conf., (Suppl. 4, Geochim. Cosmochim.
Acta), v. 3, p. 3133-3149.
- Rossiter, S.R., LaTorraca, G.A., Annan, A.P., Strangway, D.W.,
and Simmons, G., 1973, Radio Interferometry Depth
Sounding, Part II - Experimental Results, Geophysics,
v. 38, no. 3, p. 581-599.

- Rossiter, J.R., Strangway, D.W., Annan, A.P., Watts, R.D.,
and Redman, J.D., Detection of Thin Layers by Radio
Interferometry, submitted to Geophysics, 1974.
- Simmons, G., Strangway, D.W., Bannister, L., Baker, R.,
Cubley, D., LaTorraca, G., and Watts, R., 1972, The
Surface Electrical Properties Experiment, in Kopal, Z.
and Strangway, D., eds., Lunar Geophysics, Proceedings
of a Conference at the Lunar Science Institute,
Houston, Texas, 18-21, October, 1971, D. Reidel,
Dor drecht, p. 258-271.
- Strangway, D.W., Simmons, G., LaTorraca, G.A., Watts, R.D.,
Bannister, L., Baker, R., Redman, J.D., Rossiter, J.R.,
1974, Radio-Frequency Interferometry - A New Technique
for Studying Glaciers, J. of Glaciology, in press.
- Tsang, L., Kong, J.A., and Simmons, G., Interference Patterns
of a Horizontal Electric Dipole over Layered Dielectric
Media, J. Geophys. Res., v. 78, pp. 3287-3300, 1973.
- Wait, J.R., 1970, Electromagnetic Waves in Stratified Media,
2nd Edition: New York, The Macmillan Co.
- Waller, W.M., 1973, Surface Electrical Properties of
Simulation Model, Lockheed Electronics Co. Final
Report. LEC/PESD 634-TR-139 for contract NAS 9-122200,
NASA-JSC, Houston, 1973.

Figure Captions

- Fig. 1. Sketch of 2-layer earth geometry and the associated cartesian and cylindrical coordinate systems.
- Fig. 2 Complex radial wavenumber plane illustrating integration contours and location of singular points;
- ◆ branch points
 - TE pole, lower Riemann surface
 - TE pole, upper Riemann Surface
 - △ TM pole, lower Riemann surface
 - ▲ TM pole, upper Riemann surface
- Fig. 3 Schematic drawing of scale model 2-layer earth.
- Fig. 4 Schematic diagram of scale model electronics, display and recording system.
- Fig. 5 (a) sketch of radiation pattern for (E_{θ}) in X_2 - X_3 plane in a whole-space,
 (b) sketch of radiation pattern for (E_{θ}) in X_2 - X_3 plane for dipole on surface of a half-space.
- Fig. 6 Scale model experimental measurements of (E_{θ}) pattern in X_2 - X_3 plane compared with the theoretical pattern computed by Cooper (1971).
- Fig. 7 Suite of 2-layer earth responses where the substratum is a perfect reflector; — scale model response, -----normal mode theoretical response, geometrical optics theoretical response.

- Fig. 8 Suite of 2-layer earth responses for a perfectly reflecting substratum and shallow reflector depths.
—scale model response ----- normal mode theoretical response.
- Fig. 9 Suite of 2-layer earth responses for a dielectric substratum.
- Fig. A (a) Sketch of multiple reflections in thin layer.
(b) Illustration of pole positions in complex λ plane as a function of d .

Table Captions

Table 1: Cylindrical components of the E and H fields about a Horizontal Electric Dipole (HED) on the surface of a 2-layer earth in Hankel transform notation.

Table 1

10-27

(a)

$$E_r = \int_0^\infty \left\{ E_r^{TM} J_1(\lambda r) + E_r^{TE} J_1(\lambda r) \right\} d\lambda$$

$$E_\phi = \int_0^\infty \left\{ E_\phi^{TM} J_1(\lambda r) + E_\phi^{TE} J_1(\lambda r) \right\} d\lambda$$

$$E_z = \int_0^\infty E_z^{TM} J_0(\lambda r) d\lambda$$

$$H_r = \int_0^\infty \left\{ H_r^{TM} J_1(\lambda r) + H_r^{TE} J_1'(\lambda r) \right\} d\lambda$$

$$H_\phi = \int_0^\infty \left\{ H_\phi^{TM} J_1'(\lambda r) + H_\phi^{TE} J_1(\lambda r) \right\} d\lambda$$

$$H_z = \int_0^\infty H_z^{TE} J_0(\lambda r) d\lambda$$

$$J_1'(z) = \frac{\partial J_1(z)}{\partial z}$$

(b)

	TE	TM
E_r	$-\frac{j\omega\mu_0 Idl}{4\pi} \frac{\cos\phi}{j\gamma_0 r} \left[e^{\pm j\gamma_0(z-h)} + R e^{\pm j\gamma_0(z+h)} \right]$	$\frac{j\omega\mu_0 Idl}{4\pi \kappa_0^2} \cos\phi j\gamma_0 \lambda \left[e^{\pm j\gamma_0(z-h)} - R e^{\pm j\gamma_0(z+h)} \right]$
E_ϕ	$\frac{j\omega\mu_0 Idl}{4\pi} \frac{\sin\phi \lambda}{j\gamma_0} \left[e^{\pm j\gamma_0(z-h)} + R e^{\pm j\gamma_0(z+h)} \right]$	$\frac{j\omega\mu_0 Idl}{4\pi \kappa_0^2} \sin\phi \left(-\frac{\gamma_0}{\rho w} \right) \left[e^{\pm j\gamma_0(z-h)} - R e^{\pm j\gamma_0(z+h)} \right]$
E_z	0	$\frac{j\omega\mu_0 Idl}{4\pi \kappa_0^2} \cos\phi \lambda^2 \left[\pm e^{\pm j\gamma_0(z-h)} - R e^{\pm j\gamma_0(z+h)} \right]$
H_r	$-\frac{Idl}{4\pi w^2} \sin\phi \lambda \left[\pm e^{\pm j\gamma_0(z-h)} + R e^{\pm j\gamma_0(z+h)} \right]$	$-\frac{Idl}{4\pi w^2} \frac{\sin\phi}{\rho} \left[\pm e^{\pm j\gamma_0(z-h)} - R e^{\pm j\gamma_0(z+h)} \right]$
H_ϕ	$-\frac{Idl}{4\pi} \frac{\cos\phi}{\rho w^2} \left[\pm e^{\pm j\gamma_0(z-h)} + R e^{\pm j\gamma_0(z+h)} \right]$	$-\frac{Idl}{4\pi w^2} \cos\phi \lambda \left[\pm e^{\pm j\gamma_0(z-h)} - R e^{\pm j\gamma_0(z+h)} \right]$
H_z	$-\frac{Idl \sin\phi}{4\pi w^2} \frac{\lambda^2}{j\gamma_0} \left[\pm e^{\pm j\gamma_0(z-h)} + R e^{\pm j\gamma_0(z+h)} \right]$	0

$\pm = \text{sign}(z-h)$

(c) Parameters λ Radial wavenumber γ_i Vertical wavenumber in region $i = (k_i^* - \lambda^2)^{1/2} \cdot 2\pi$ $k_i^* = k_i (1 + j \tan \delta_i)$ complex dielectric constant $k_i = 2\pi (k_i^*)^{1/2} = (k_i)^{1/2} (1 + j \frac{\tan \delta_i}{2})$ normalized propagation constant in region i $w =$ free space wavelength $h =$ elevation of dipole above surface in wavelengths(d) TE and TM Reflection Coefficients and Transmission at Plane Boundaries

$$R_{ij}^{TE} = \frac{\gamma_i - \gamma_j}{\gamma_i + \gamma_j}$$

$$R_{ij}^{TM} = \frac{k_i^* \gamma_j - k_j^* \gamma_i}{k_i^* \gamma_j + k_j^* \gamma_i}$$

$$T_{ij}^{TE} = 1 + R_{ij}^{TE}$$

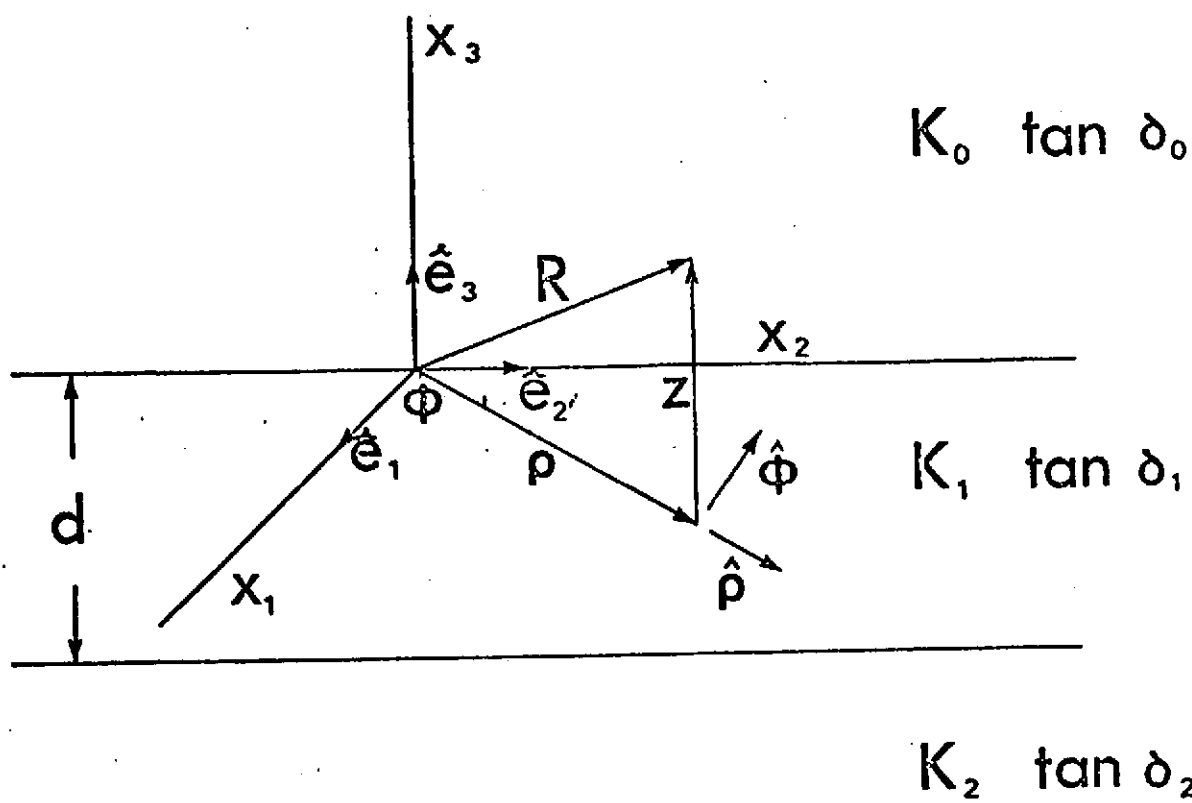
$$T_{ij}^{TM} = 1 + R_{ij}^{TM}$$

(e) 2 layer Earth Reflection Coefficient

$$R_{TM}^{TE} = R_{01}^{TE} + \frac{\frac{R_{01}^{TE} R_{10}^{TE}}{T_{01}^{TE} T_{10}^{TE}} R_{12}^{TE} \beta}{1 - R_{10}^{TE} R_{12}^{TE} \beta}$$

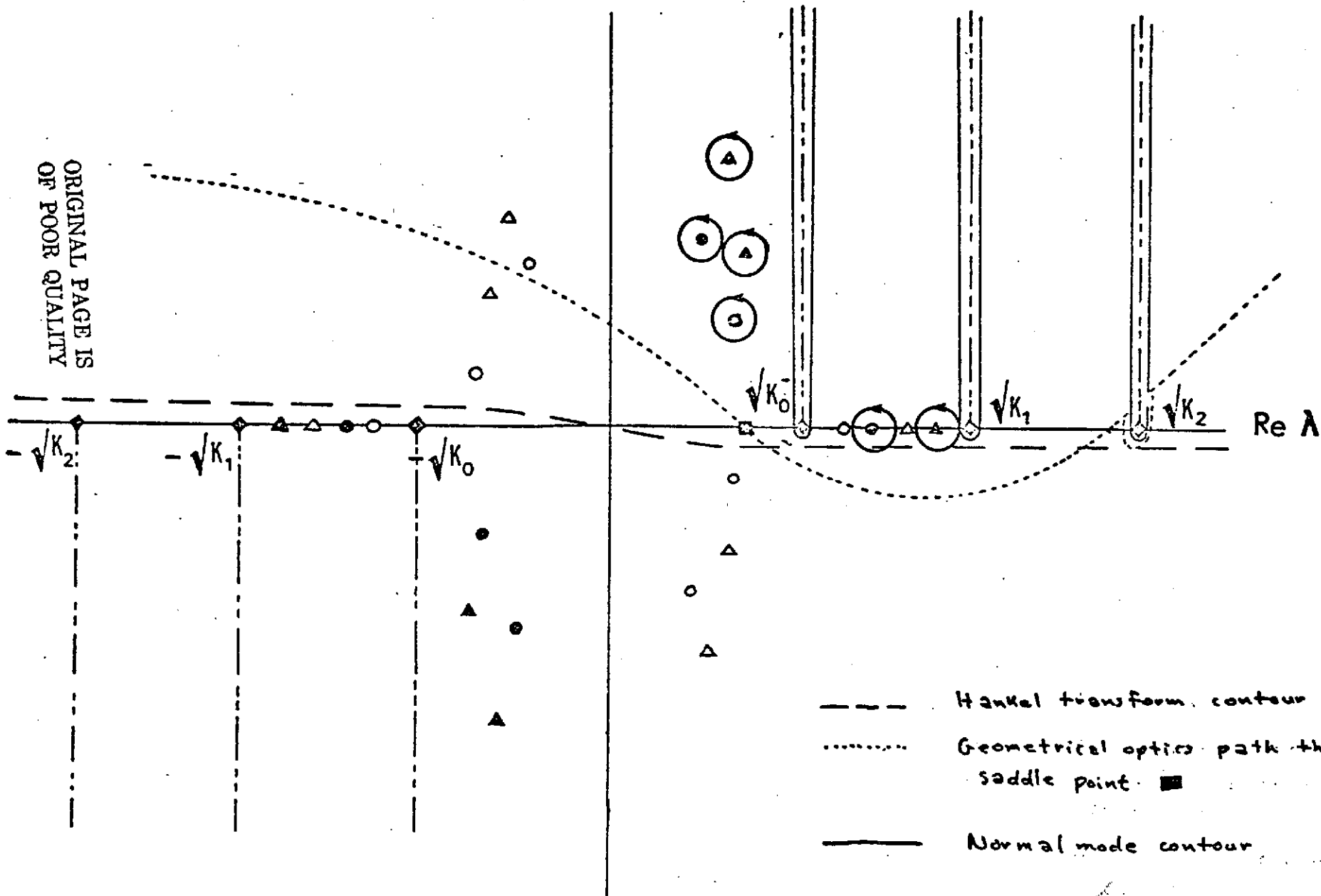
$$\beta = e^{j\gamma_1 d}$$

2 way phase shift in layer

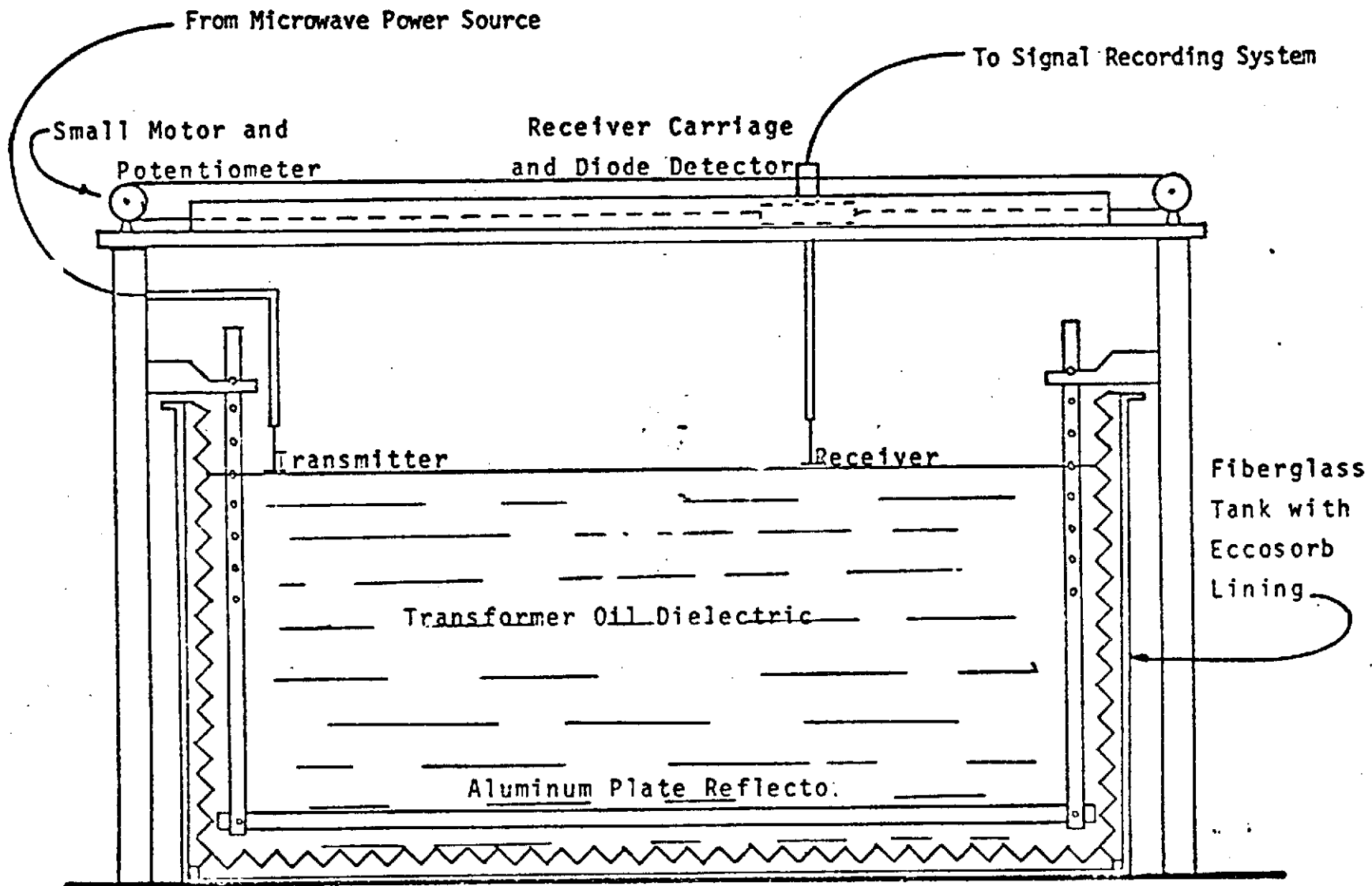


Im λ

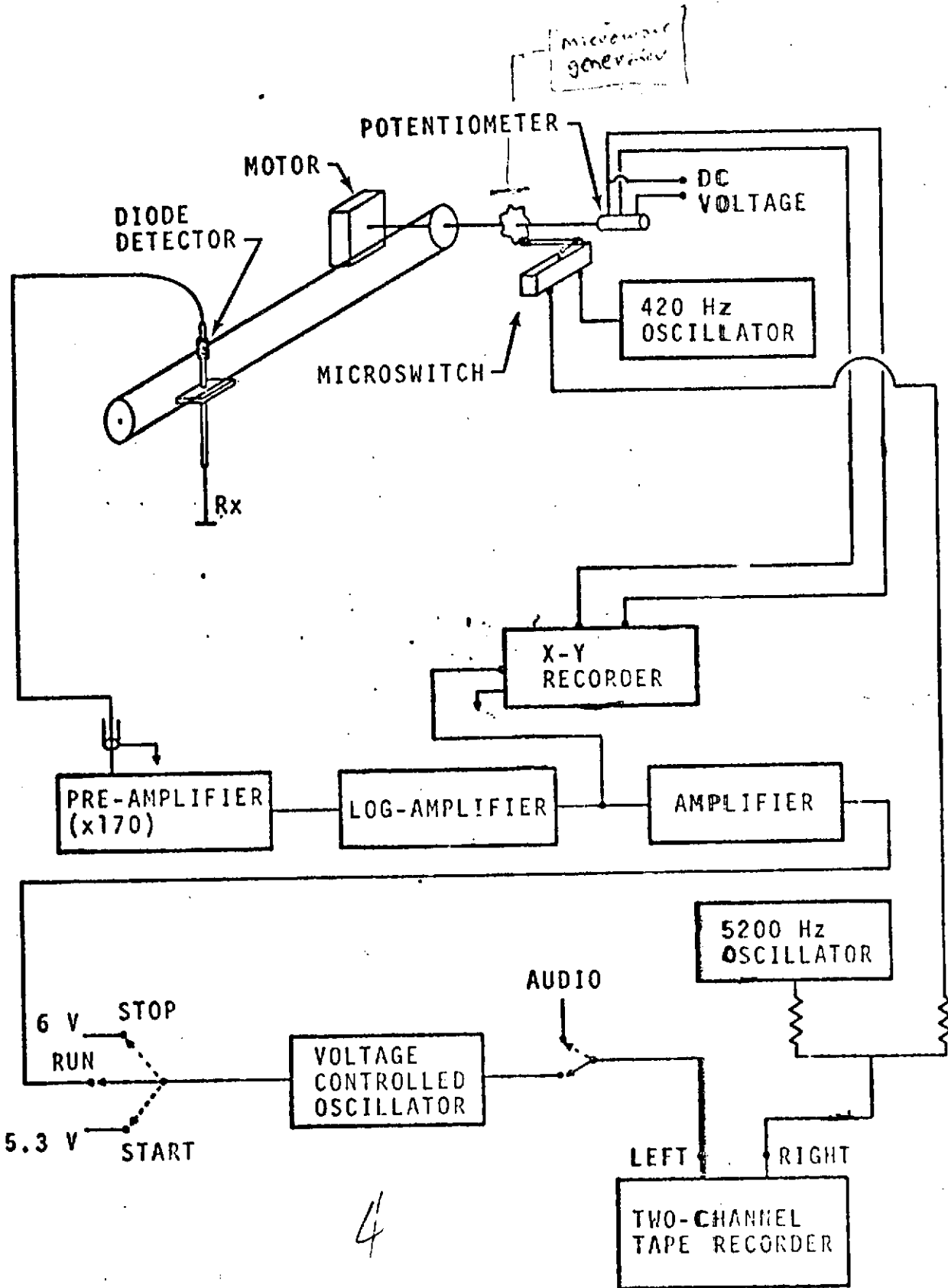
ORIGINAL PAGE IS
OF POOR QUALITY



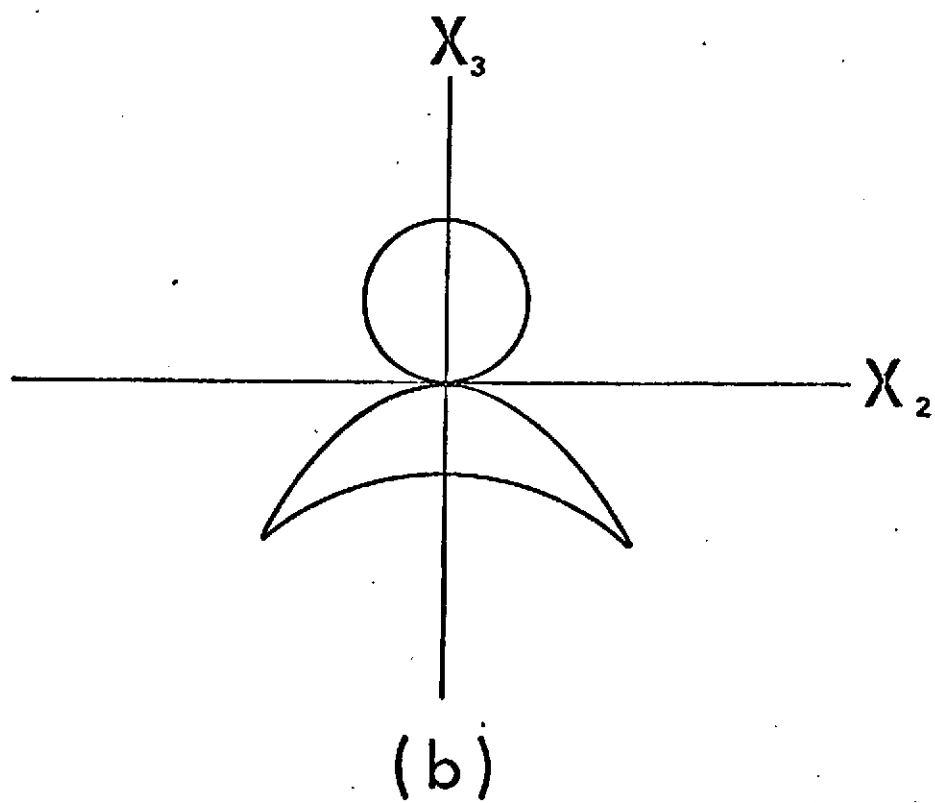
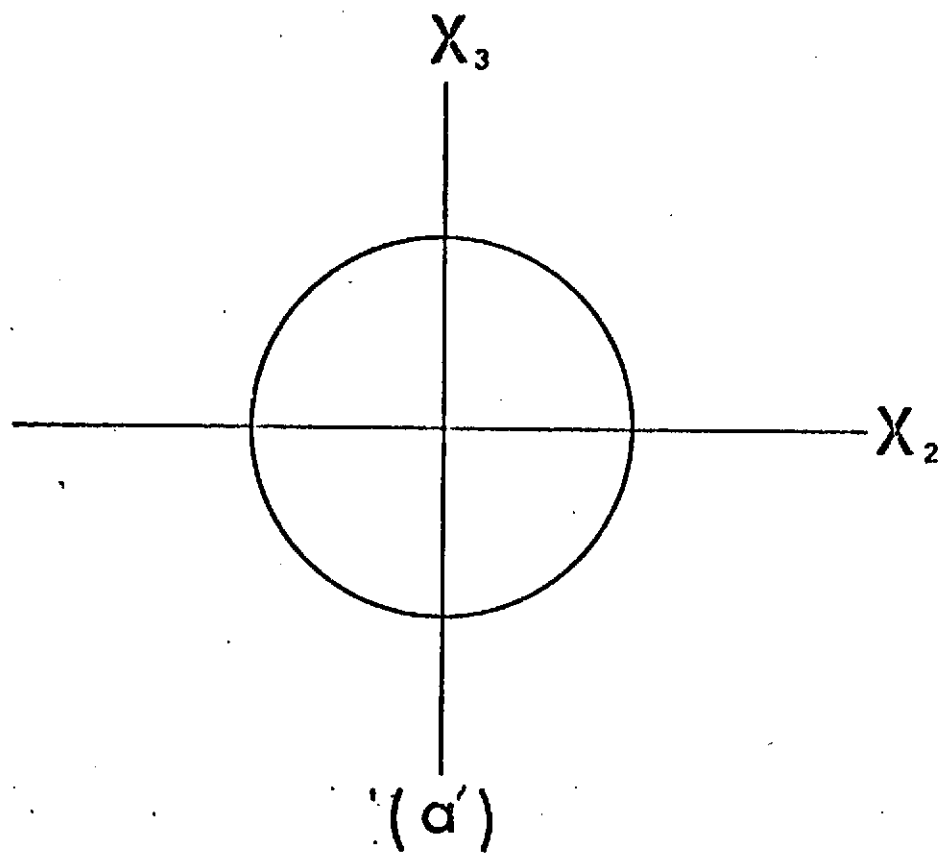
- Hankel transform contour
- Geometrical optics path through saddle point
- Normal mode contour
- · - · Branch-cuts



ORIGINAL PAGE IS
OF POOR QUALITY



ORIGINAL PAGE IS
OF POOR QUALITY



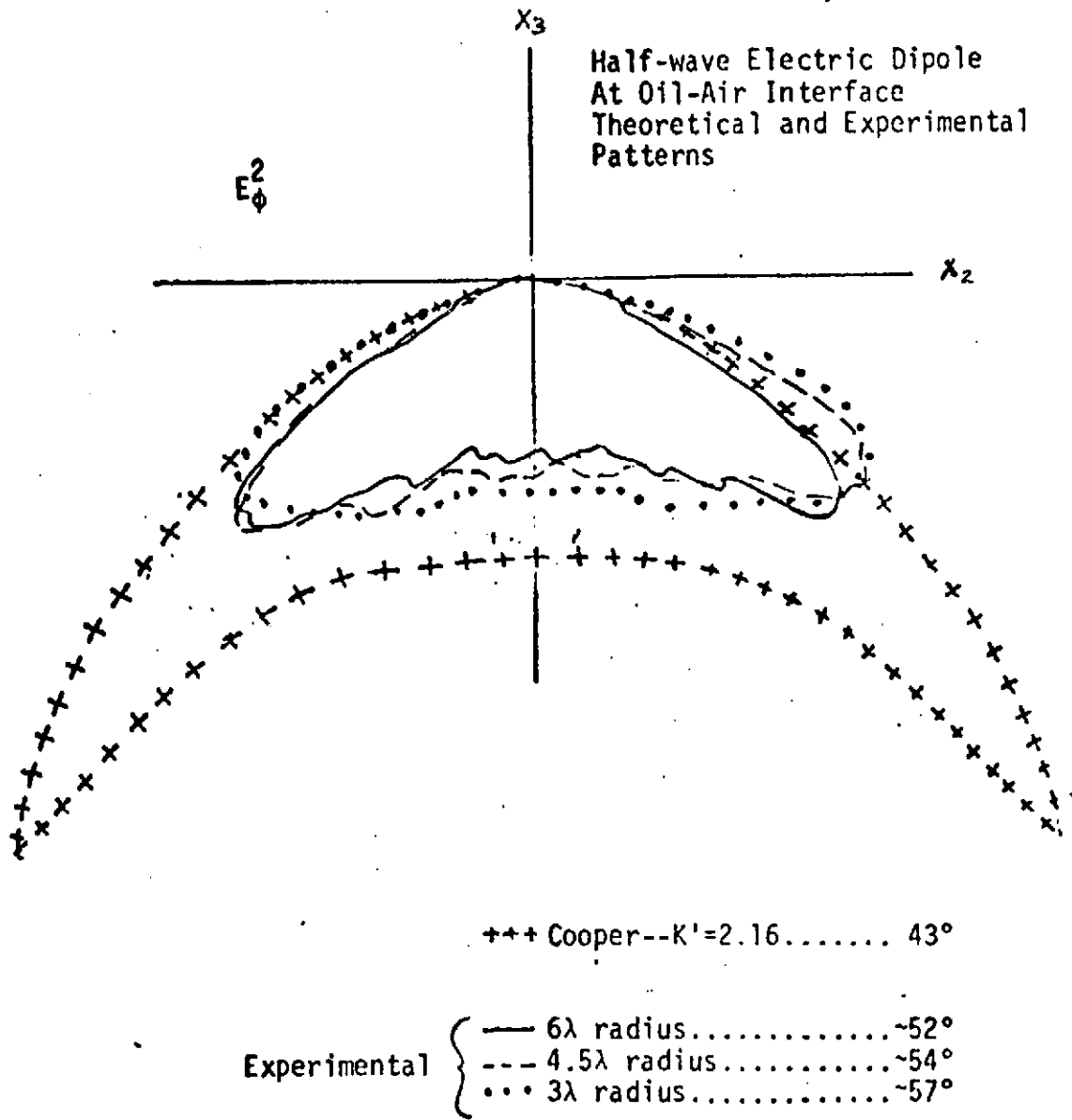
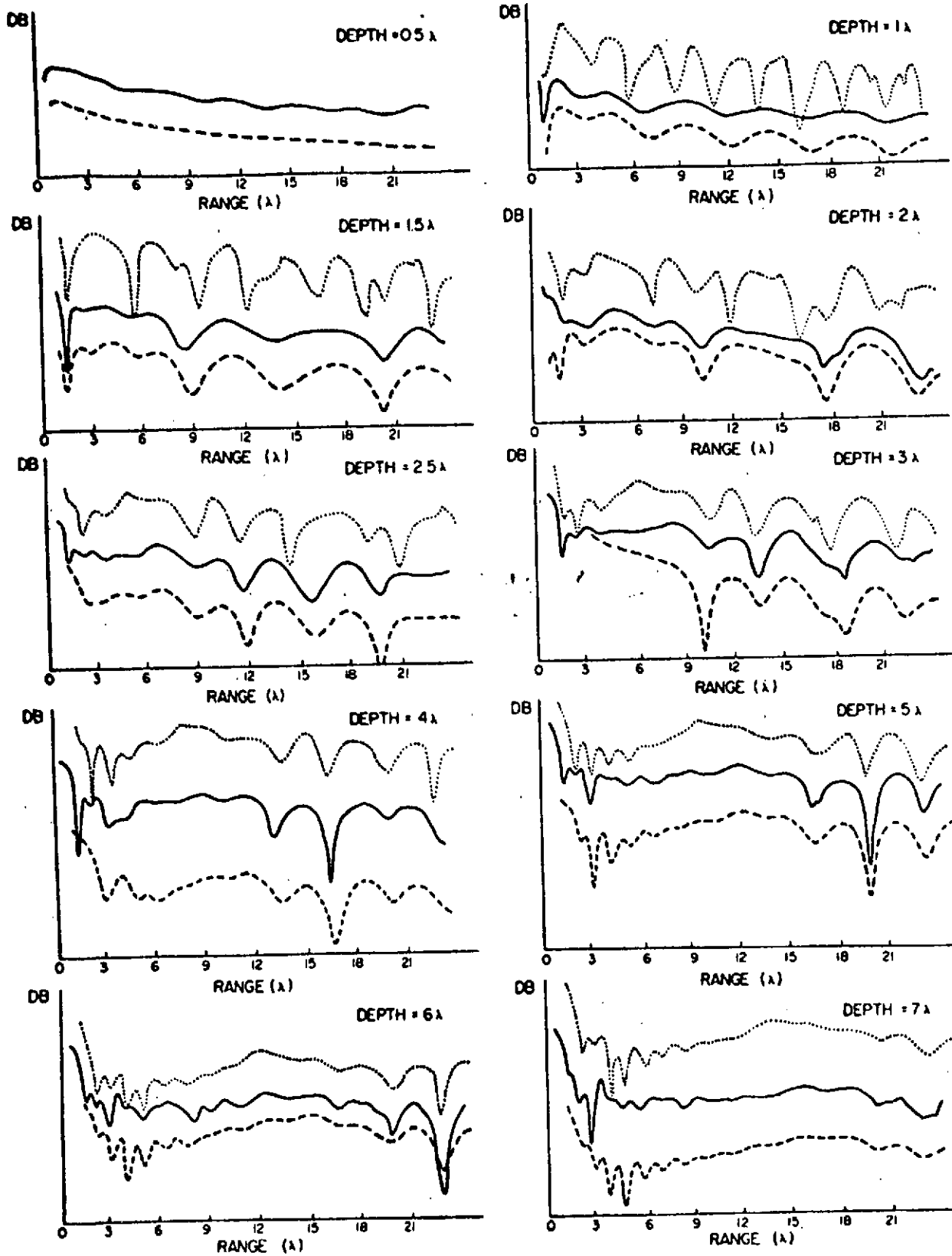


Figure 6 - Antenna pattern at various radii.

ORIGINAL PAGE IS
OF POOR QUALITY

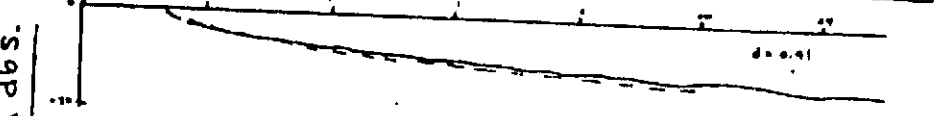
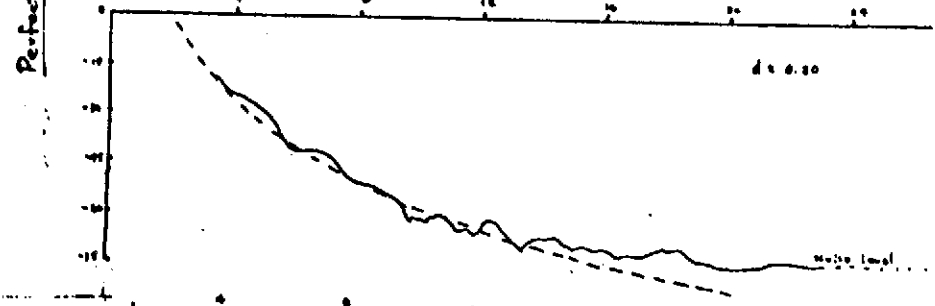
THEORETICAL SOLUTIONS AND SCALE - MODEL RESULTS
PLANE LAYERED GEOMETRY, VARIOUS DEPTHS TO REFLECTOR



SCALE - MODEL ———
 THEORETICAL
 GEOMETRICAL OPTICS ———
 NORMAL MODES - - - - -

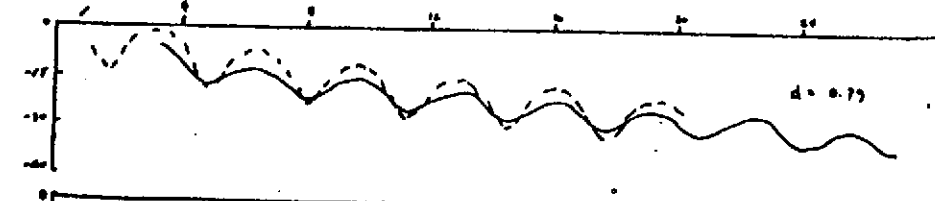
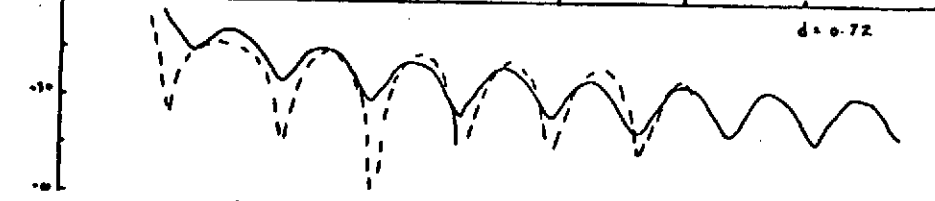
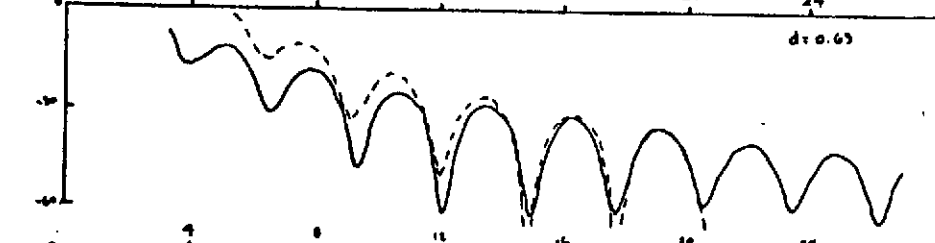
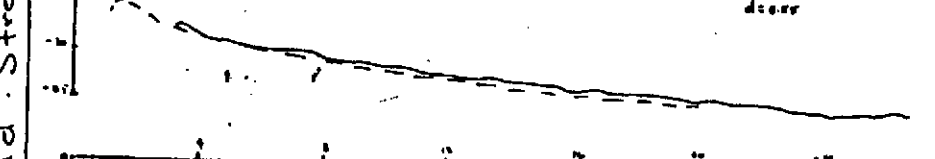
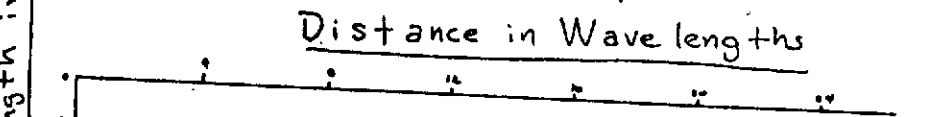
$n = 2.16$
 $\tan \delta = 0.0022$

Fig. 7



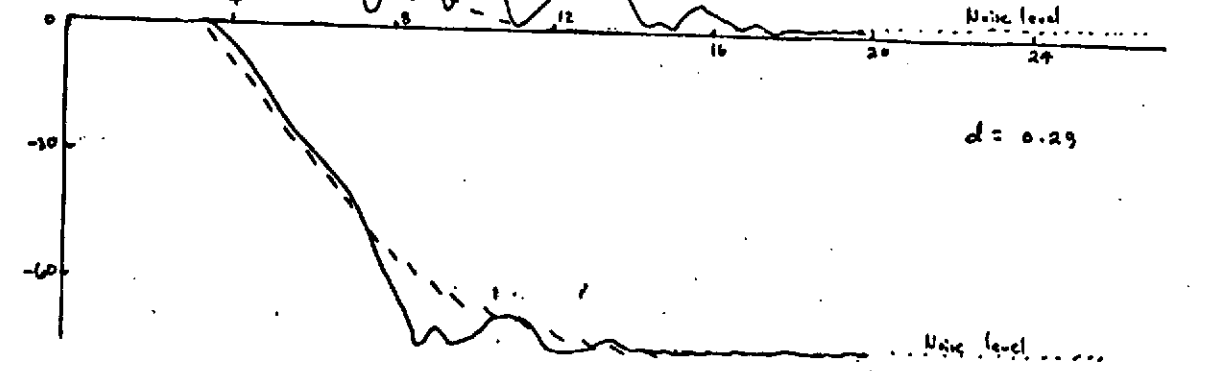
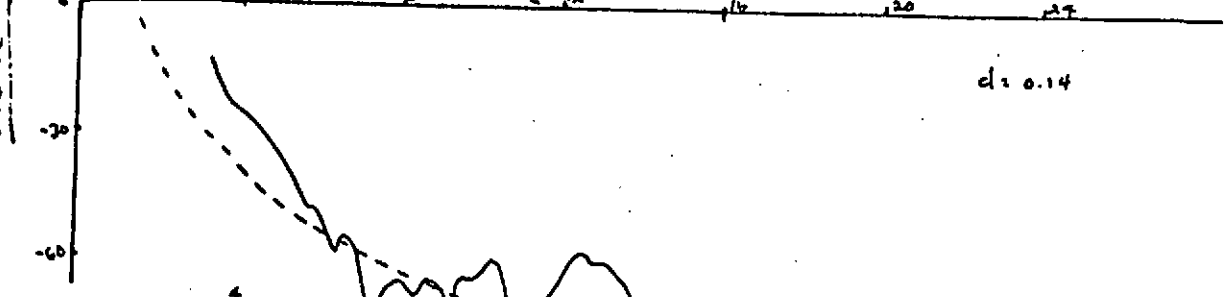
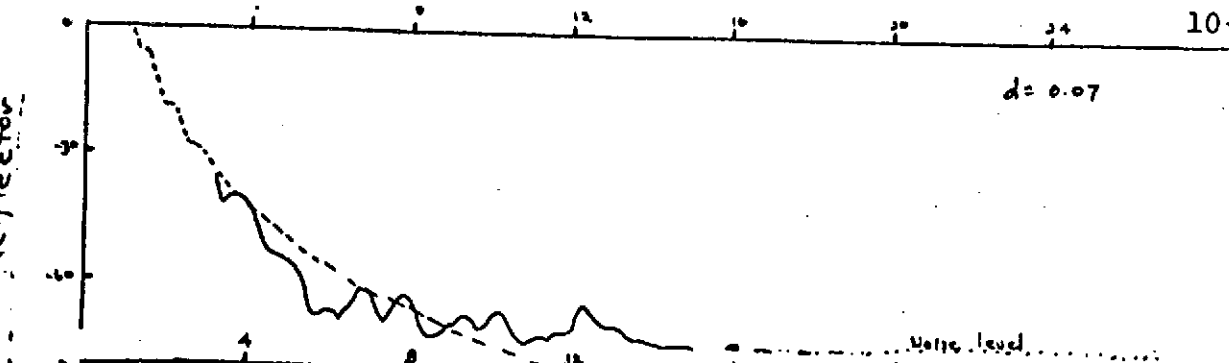
Field Strength in dbS.

Distance in Wave lengths

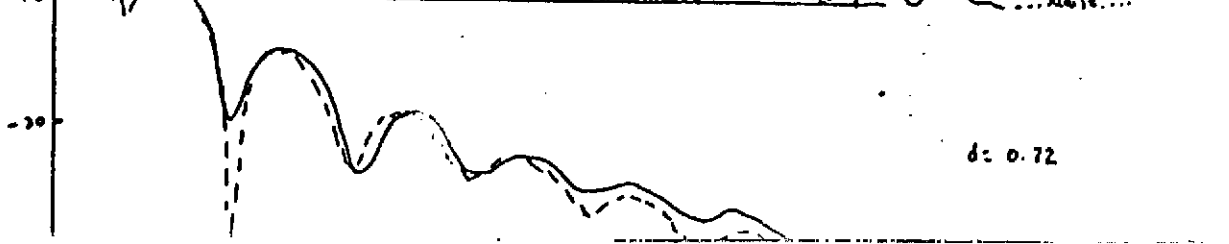
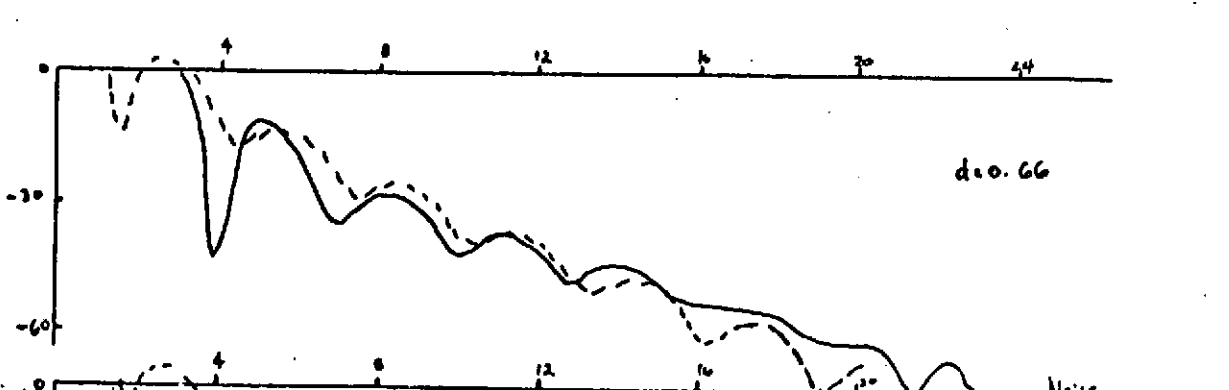
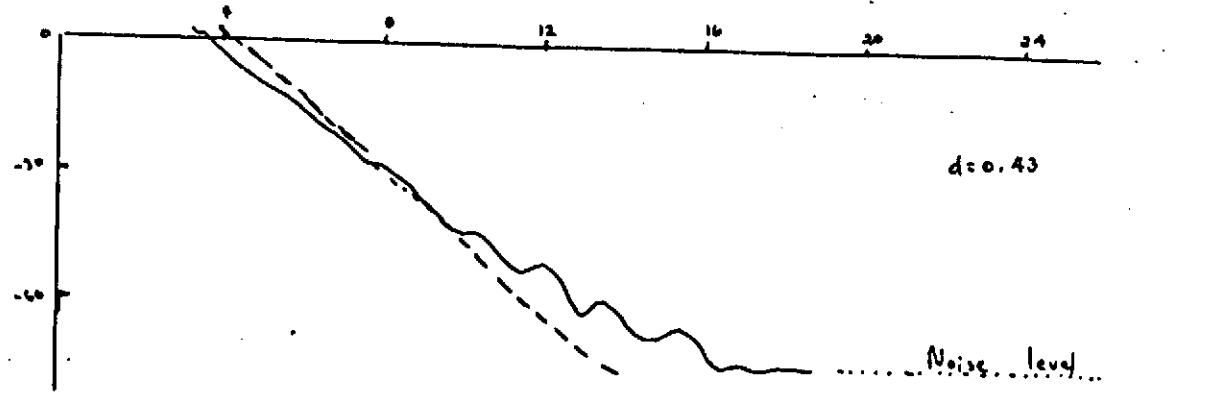


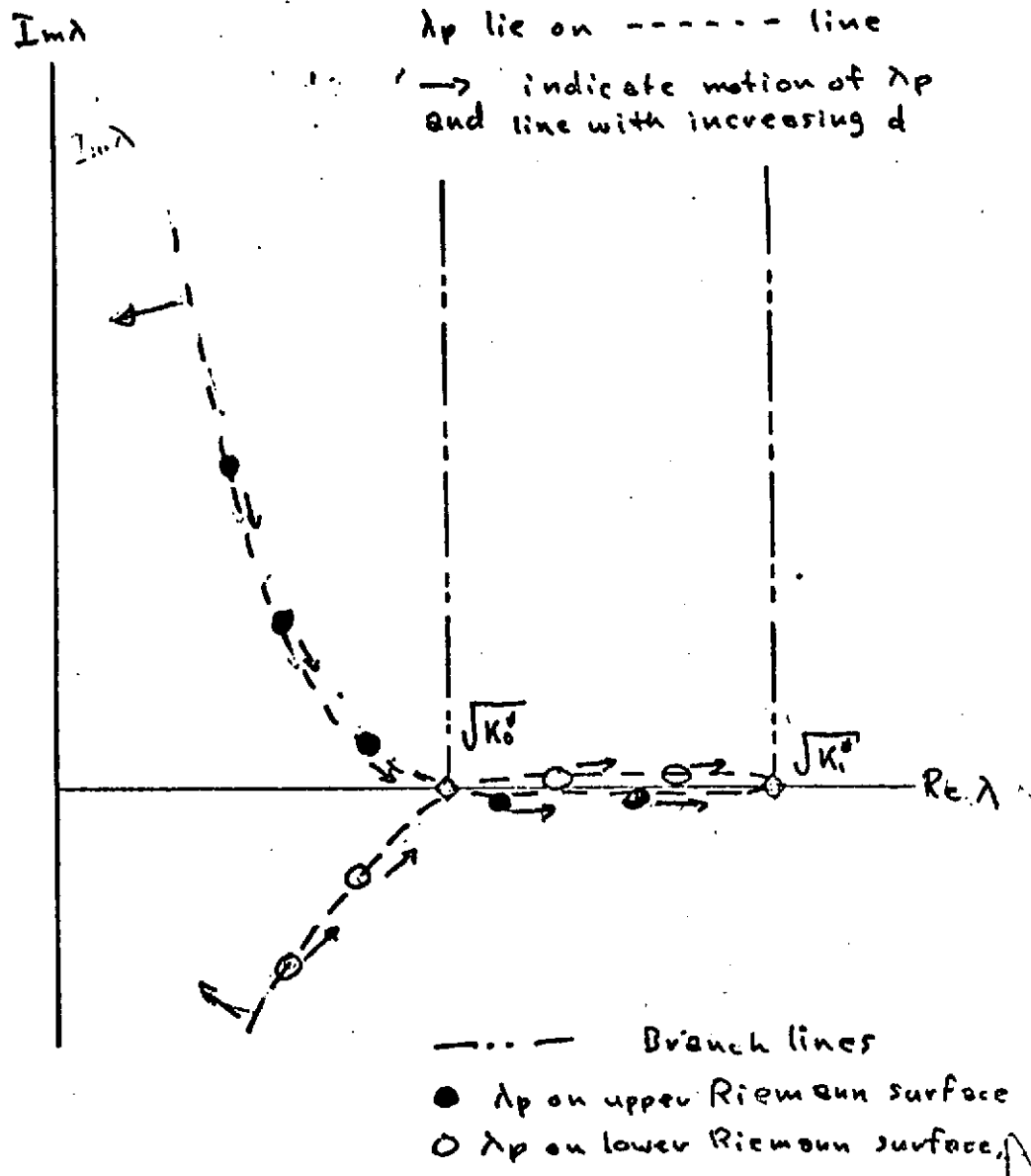
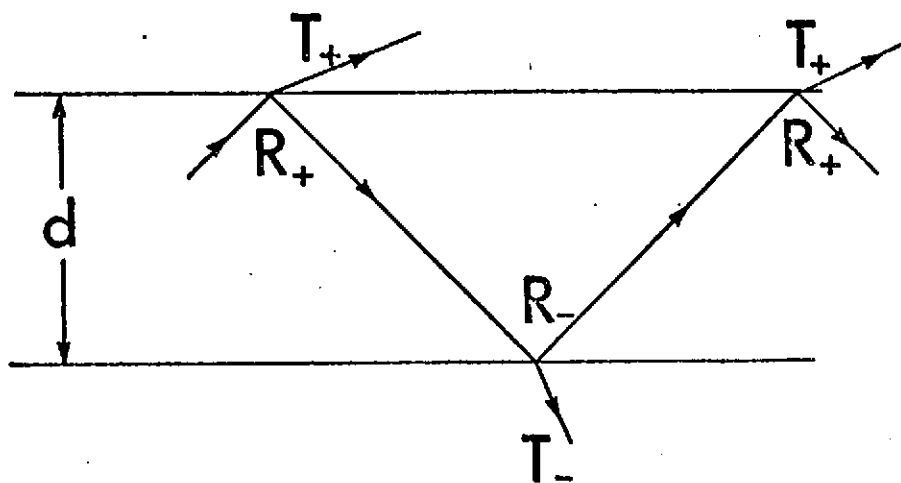
ORIGINAL PAGE IS OF POOR QUALITY

Dielectric Reflector



Field strength in db.





ORIGINAL PAGE IS
OF POOR QUALITY

DETECTION OF THIN LAYERS BY RADIO INTERFEROMETRY

J.R.Rossiter¹, D.W.Strangway², A.P.Annan¹
R.D.Watts,³ and J.D.Redman².

1. Department of Physics
University of Toronto
Toronto, M5S 1A7
Canada
2. Department of Geology,
University of Toronto,
Toronto, M5S 1A1
Canada
3. Presently at U.S.G.S.
Denver, Colorado, U.S.A.

February 22, 1974

ABSTRACT

Recent theoretical work on the radio interferometry technique for dielectric layers of less than one free space wavelength thick, has indicated that there is ^a thickness for which no interference is observed. This thickness is about 0.2 wavelengths, ^{for ice} and it lies between the thickness that allows one single mode to propagate in the layer (> 0.2) and a thickness (< 0.2) that is essentially transparent to the wavelength being used.

Field work was done on the Juneau Icefield using frequencies from 1 to 32 MHz. At 1 and 2 MHz, an interference pattern typical of a half space of ice (dielectric constant of 3.3) is observed, while at 4 MHz essentially no interference is seen. At higher frequencies, the interference observed is typical of that of a layer overlying a half space. These results can be interpreted to be the result of a dielectric layer of depth 15 to 20 m (0.2 wavelengths at 4 MHz) with a dielectric constant of 2.4. The layer of snow overlies a half space of ice. The technique is therefore of potential interest in interpreting the nature of a snow layer overlying a glacier.

INTRODUCTION

Radio frequency interferometry depth sounding was originally developed to measure the dielectric properties and structure of highly resistive geological regions (Annan, 1970, 1973). It has been used successfully for sounding glaciers (Rossiter et al., 1973; Strangway et al., 1974), and on the moon (Simmons et al., 1972; SEP Team, 1974). The technique consists of setting a radio transmitter on the surface to be sounded, and measuring the field strength as a function of distance from the transmitter. Several waves propagate from the transmitter to the receiver, generating an interference pattern that is indicative of both the dielectric properties and the structure of the medium.

Theoretical studies have determined the fields to be expected over dielectric layers (Annan, 1973; Kong, 1972, Tsang et al., 1973). Early work used geometrical optics approximations in order to evaluate the integral expressions, but it can be shown that the method is highly inaccurate for layers less than about 2 free space wavelengths (abbreviated "wl" throughout) thick. In more recent work, a normal model approximation has been used that is particularly suitable for calculating the fields in the presence of a thin layer. In a companion paper (Annan et al., 1974), theoretical and experimental data from an analogue scale model are compared. In the present paper, we will examine the particular case of a thin dielectric layer (0 to 1 wl thick) overlying a thick dielectric layer (see Fig.1), using mode theory and field data collected on the Juneau Icefields, Alaska.

THEORY OF THIN LAYERS

Radio interferometry data show three distinct types of behaviour as the upper layer increases from being very thin and transparent, through a critical thickness, to being thick enough to allow propagating modes. We will examine each of these three cases.

(a) Very thin transparent upper layer

When the upper layer is very thin (less than about $0.2 w_l$ thick), it is essentially transparent. Therefore, the observed interference pattern is independent of the properties of the upper layer, and looks like that of a half space with the properties of the lower layer (see Figures 2 and 3).

(b) Transition thickness - decoupled layer

As the upper layer becomes approximately $0.2 w_l$ thick (depending on its dielectric constant), it effectively decouples any signal from the lower layer. However, if it is still too thin to allow free propagation within itself, the observed patterns will show no interference at all (see Figure 4). Since this transition band is very narrow (and may be non-existent for very low losses), it is extremely diagnostic of upper layer thickness.

(c) Modal propagation in the upper layer

As the upper layer becomes thick enough to support freely propagating modes, the interference patterns again show clear beating (see Figures 5 and 6). Since the interference is generated by modes propagating along the thin layer guide, the spatial frequency of the

beats is relatively low, and dependent on the properties of the upper layer (although occasionally a higher spatial frequency ripple, due to the lower layer, can be seen).

ORIGINAL PAGE IS
OF POOR QUALITY

JUNEAU ICEFIELD DATA

During the summer of 1972, measurements were made at various locations on the Juneau Icefields (see Figure 7). We will examine two runs - Run 36 made from Site 6 on the Taku Glacier, and Run 92 made from Site 25, in ^{the} accumulation zone of the Matthes Glacier. At Site 6, the thickness of ice has been determined seismically to be approximately 350 m. (Miller, 1950). The thickness of the ice at Site 25 is uncertain, but it is probably about 200 m.

Measurements were made at six frequencies - 1, 2, 4, 8, 16, and 32 MHz, so that the free space wavelength varied from 300 m to about 10 m. Six components of the magnetic field were measured - three from each of two transmitting antenna orientations. Of these components, we presently have theoretical solutions for two of them - the vertical (H_z) and radial (H_ρ) magnetic fields from a broadside transmitting antenna. These two components were compared to suites of theoretical curves and a best fit that gave consistent results for all frequencies was found.

For both runs, the data at 32 MHz were so scattered that interpretation was not possible. The scattering is seen slightly at 16 and 8 MHz, and seems typical of glacier data (Strangway et al., 1974). We attribute this scattering to random reflections from crevasses and other irregularities in the ice with typical sizes of about 10 m.

The parameters deduced from each frequency for the two runs are listed in Table 1, and the best fit is illustrated in Figures 8 and 9.

In each case, the two components gave similar results. From the 1 and 2 MHz data, the dielectric constant and loss tangent of the lower layer can be estimated. From the 4 MHz curves, very tight limits can be put on the thickness of the upper layer. From 8 and (to some extent) 16 MHz data, the properties of the upper layer can be determined.

Runs 36 and 92 differ in two basic respects. For Run 36, the loss tangents are typical for ice - $0.2/f$, where f is frequency in MHz (Evans, 1965). The values obtained for the thickness of the upper layer are very consistent from frequency to frequency. For Run 92, it was not possible to obtain a consistent thickness without letting the loss tangent drop to at least $0.1/f$. Even then, the depths obtained for the lower frequencies (especially 4 MHz) were less than 15 m while for 8 and 16 MHz a depth of about 20 m was required.

DISCUSSION

We interpret the thin upper layer at both sites as being snow about 15 to 20 m thick, with a dielectric constant of 2.4, overlying thick glacial ice, with a dielectric constant of 3.3. The loss tangent at Site 6 (Run 36) is about $0.2/f$, while at Site 25 (Run 92), it is $0.1/f$.

These dielectric properties are typical for ice and snow (Evans, 1965). Since snow is a mixture of air and ice, its dielectric constant is somewhat lower than that of ice, although its loss tangent is not greatly different. We attribute the lower loss tangent at Site 25 to the lower temperature of the ice and snow at the higher site. It is interesting that although the measurements were made in summer with

runoff water abundant on the surface, the losses were not very high. Presumably, the water is too thin or too well disseminated to be noticeable at the frequencies used.

The inconsistency of the depth determinations between frequencies at Site 25 could possibly be due to a grading of the snow-ice boundary at that altitude. Since Site 25 is in the accumulation zone of the glacier, snow may be compacting in that area.

CONCLUSION

Using radio-frequency interferometry, a thin layer can be detected and estimates of the thickness of the layer to within a few meters can be made. By using a range of frequencies, the dielectric parameters of both the upper and the lower layer can be obtained.

Acknowledgements

Field work, data collection and reduction was done under NASA Contract No. NAS 9-11540 to MIT and a subcontract to the University of Toronto for the Apollo Surface Electrical Properties Experiment. We thank Messrs. G. LaTorraca, R. Baker, and L. Bannister, and Dr. G. Simmons.

Support for the analysis and interpretation of the data from the Department of Energy, Mines and Resources, under Research Agreement 1135-D13-4-16/73, is gratefully acknowledged.

References

- Annan, A.P., "Radio Interferometry Depth Sounding", M.Sc. thesis, Department of Physics, University of Toronto, 1970.
- Annan, A.P., "Radio Interferometry Depth Sounding: Part I - theoretical discussion", Geophysics, v. 38, pp. 557-580, 1973.
- Annan, A.P., Waller, W.M., Strangway, D.W., Rossiter, J.R., and Redman, J.D., "The electromagnetic response of a low-loss two-layer dielectric earth for horizontal electric dipole excitation", submitted to Geophysics, 1974.
- Evans, S., "Electrical properties of ice and snow - a review", J. Glaciology, v. 5, pp. 773-792, 1965.
- Kong, J.A., "Electromagnetic fields due to dipole antennas over stratified anisotropic media", Geophysics, v. 37, pp.985-996, 1972.
- Miller, M.M., "Preliminary Report of field operations, Juneau Icefield Research Project, 1949", J.I.R.P., no.2, American Geographical Society, New York, 1950.

- Rossiter, J.R., LaTorraca, G.A., Annan, A.P., Strangway, D.W., and Simmons, G., "Radio interferometry depth sounding: Part II - experimental results", Geophysics, v. 38, pp. 581-599, 1973.
- Simmons, G., Strangway, D.W., Bannister, L., Baker, R., Cubley, D., LaTorraca, G., and Watts, R., "The Surface Electrical Properties Experiment", Lunar Geophysics, Proceedings of a conference at the Lunar Science Institute, Houston, Texas, 18-21 October, 1971, D. Reidel, Dordrecht, pp. 258-271, 1972.
- Strangway, D.W., Simmons, G., LaTorraca, G., Watts, R., Bannister, L., Baker, R., Redman, D., and Rossiter, J., "Radio-frequency interferometry - a new technique for studying glaciers", J. Glaciology, in press, 1974.
- Surface Electrical Properties Team, "The Surface Electrical Properties Experiment", Apollo 17 Preliminary Science Report, in press, 1974.
- Tsang, L., Kong, J.A., and Simmons, G., "Interference patterns of a horizontal electric dipole over layered dielectric media", J. Geophys. Res. v. 78, pp. 3287-3300, 1973.

TABLE 1: INTERPRETATION OF JUNEAU RUNS 36 AND 92 BY COMPARISON TO THEORY

RUN 36

<u>Frequency (MHz)</u>	<u>\bar{d}_1 wl (m.)</u>	<u>k_1</u>	<u>$\tan \delta_1$</u>	<u>k_2</u>	<u>$\tan \delta_2$</u>
1	$< 0.075 (< 23)$	-	-	3.3 ± 0.1	0.20 ± 0.10
2	.100-.150(15-23)	-	-	3.3 ± 0.1	0.10 ± 0.05
4	0.2-0.3 (15-22)	-	-	-	0.05 ± 0.03
8	0.45-0.60 (17-22)	2.4 ± 0.1	$.02 \pm .01$	-	-
16 (1)	0.9 -1.2 (17-22)	2.4 ± 0.2	0.010 ± 0.005	-	-
<u>Interpretation:</u>	19 ± 4 m.	2.4 ± 0.1	$0.2 \pm 0.1/f^{(2)}$	3.3 ± 0.1	$0.2 \pm 0.1/f^{(2)}$

RUN 92

ORIGINAL PAGE IS
OF POOR QUALITY

1	$< 0.1 (< 30)$	-	-	3.3 ± 0.1	0.10 ?
2	$< 0.125 (< 20)$	-	-	3.3 ± 0.1	0.05-0.10
4	.100-175(7-13) .125-200(9-15)	@ 2.4	-	-	@ .05 @ .02
8	0.5 - 0.7(19-26)	2.4 ± 0.1	$.02 \pm .01$	-	-
16 ⁽¹⁾	$1.2 \pm 0.1(22 \pm 2)?$	2.4 ± 0.2	$< .02$	-	-
<u>Interpretation:</u>	18 ± 8 m.	2.4 ± 0.2	$0.10/f^{(2)}$	3.3 ± 0.1	$0.10 \pm 0.05/f^{(2)}$

- 16 MHz data are fairly scattered (see text).
- f in MHz. Because of its dielectric mechanism, the loss tangent of ice essentially behaves as $f \cdot \tan \delta = \text{constant. (Evans, 1965)}$.

FIGURE CAPTIONS

- Fig. 1. Configuration of a thin dielectric layer overlying an infinite dielectric half space. By varying the frequency, the thickness of the upper layer in wavelengths can be changed.
- Fig. 2. Theoretical curves for a very thin upper layer, with the dielectric constant of the lower layer varying. The spatial frequency of the pattern increases with increasing k_2 .
(a) H_{ρ} broadside component; (b) H_z broadside component.
- Fig. 3. Theoretical curves for a very thin upper layer with the loss tangent of the lower layer varying. The sharpness of the interference drops off with increasing $\tan \delta_2$. (a) H_{ρ} broadside component, (b) H_z broadside component.
- Fig. 4. Theoretical curves for the region of no interference showing the transition from a transparent upper layer to an upper layer that propagates freely. (a) H_{ρ} broadside component, (b) H_z broadside component.
- Fig. 5. Theoretical curves for a propagating upper layer, with the dielectric constant of the upper layer varying. (a) H_{ρ} broadside component, (b) H_z broadside component.
- Fig. 6. Theoretical curves for a propagating upper layer, with the loss tangent of the upper layer varying. (a) H_{ρ} broadside component, (b) H_z broadside component.

Fig. 7 Map of the Juneau Icefield near Camp 10. Radio interferometry was conducted at "R.F.I.Sites". Seismic depths are indicated where known. Run 36 was made at Site 6. Run 92 was made high on the Matthes Glacier (not on the map) near Camp 18.

Fig. 8 Radio interferometry data, H_{ρ} and H_z broadside components, 1 to 16 MHz for Run 36, Site 6 (Solid lines). The best fit theoretical curves are also shown (dashed lines).

Fig. 9 Radio interferometry data, H_{ρ} and H_z broadside components, 1 to 16 MHz, for Run 92, Site 25 (solid lines). The best fit theoretical curves are also shown (dashed lines).

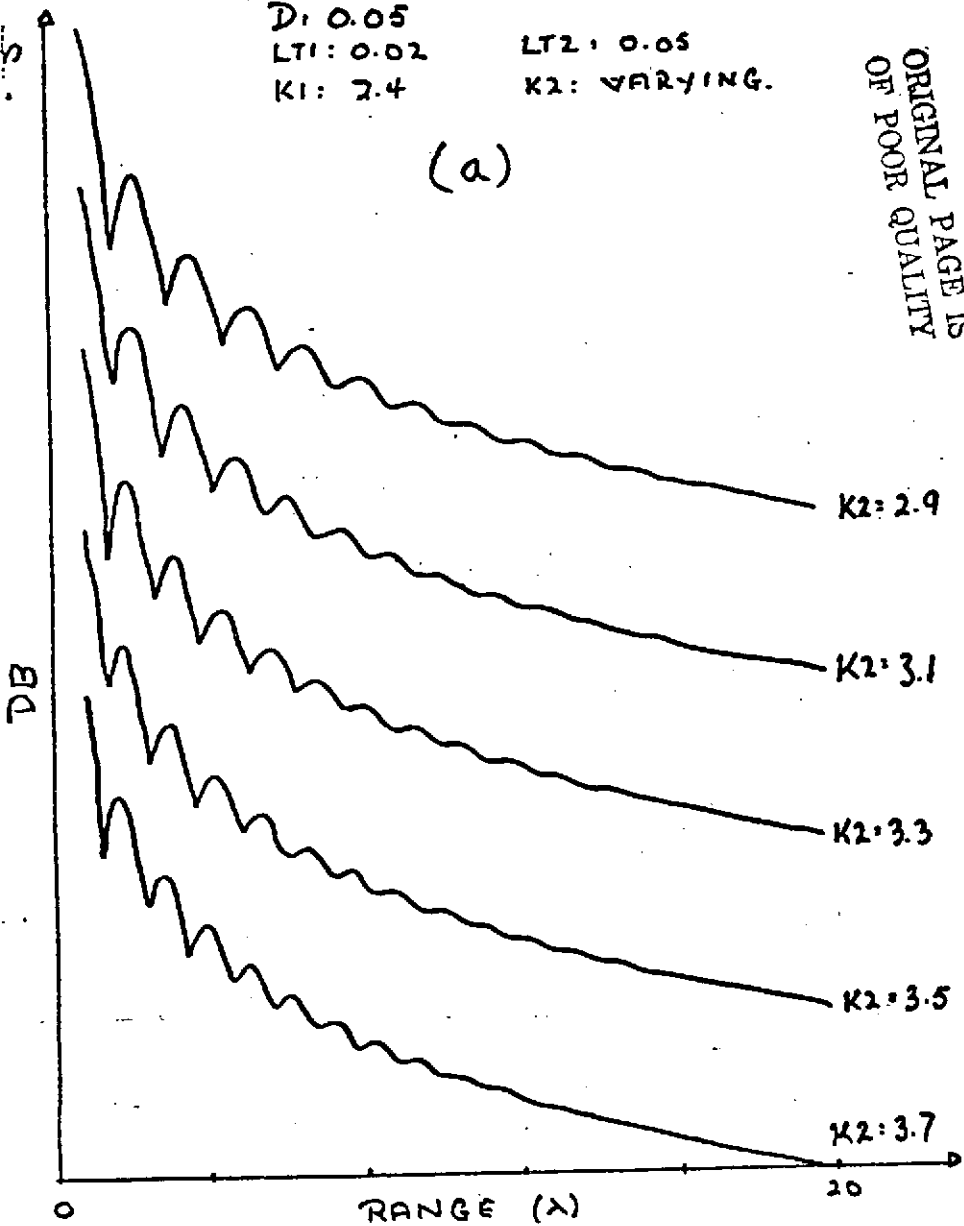
	Air	$k_1 = 1$	$\tan \delta_0 = 0$	
d_1	Thin layer	k_1	$0 < \tan \delta_1 < .2$	$0 < d_1 < 1 \text{ wl}$
	Thick layer	$k_2 > k_1$	$\tan \delta_2 \approx \tan \delta_1$	$d_2 \rightarrow \infty$
d_2				

Fig. 1: Configuration of a thin dielectric layer overlying an infinite dielectric half-space.

D: 0.05
LT1: 0.02
K1: 2.4

LT2: 0.05
K2: VARYING.

(a)

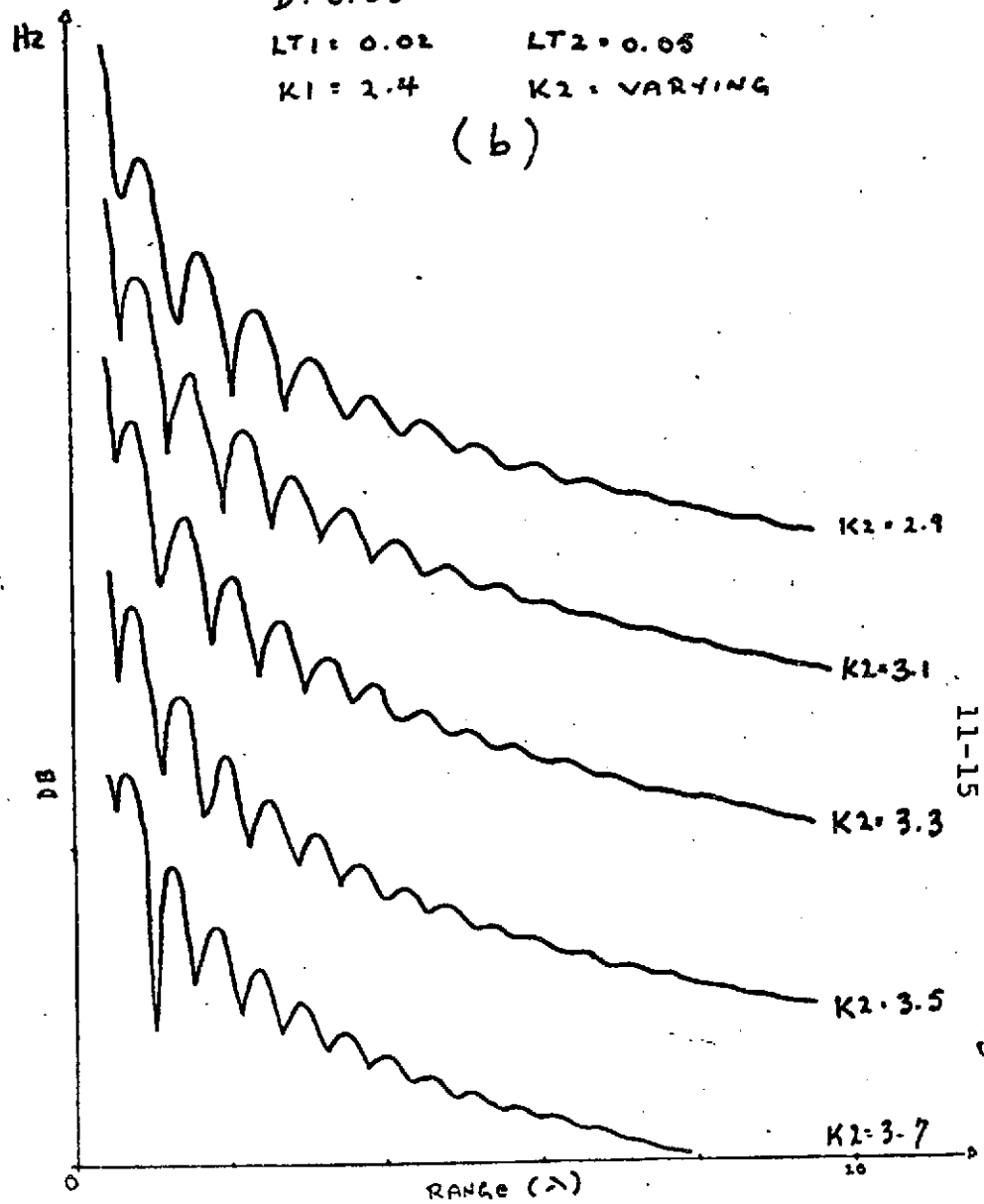


ORIGINAL PAGE IS
OF POOR QUALITY

D: 0.05
LT1: 0.02
K1: 2.4

LT2: 0.05
K2: VARYING

(b)



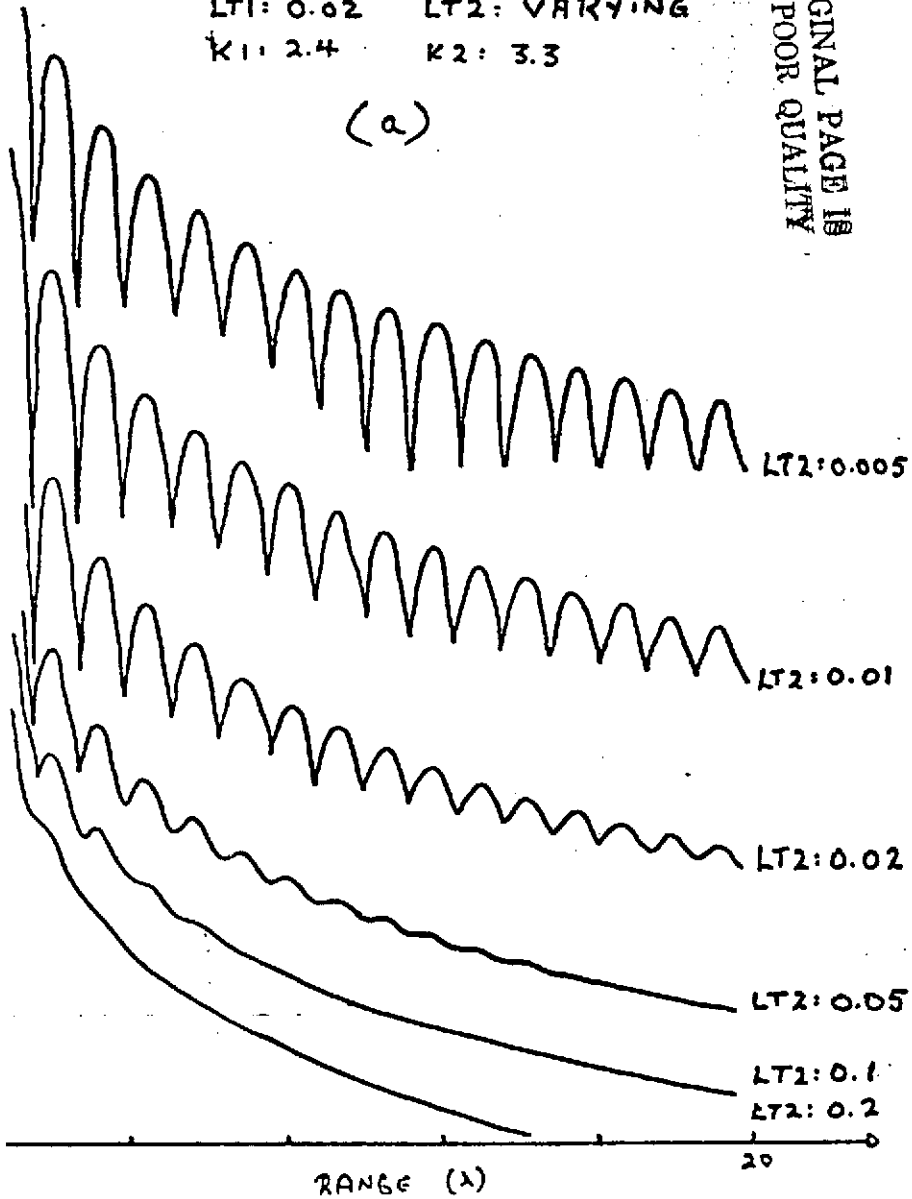
11-15

1.5

D: 0.05
LT1: 0.02 LT2: VARYING
K1: 2.4 K2: 3.3

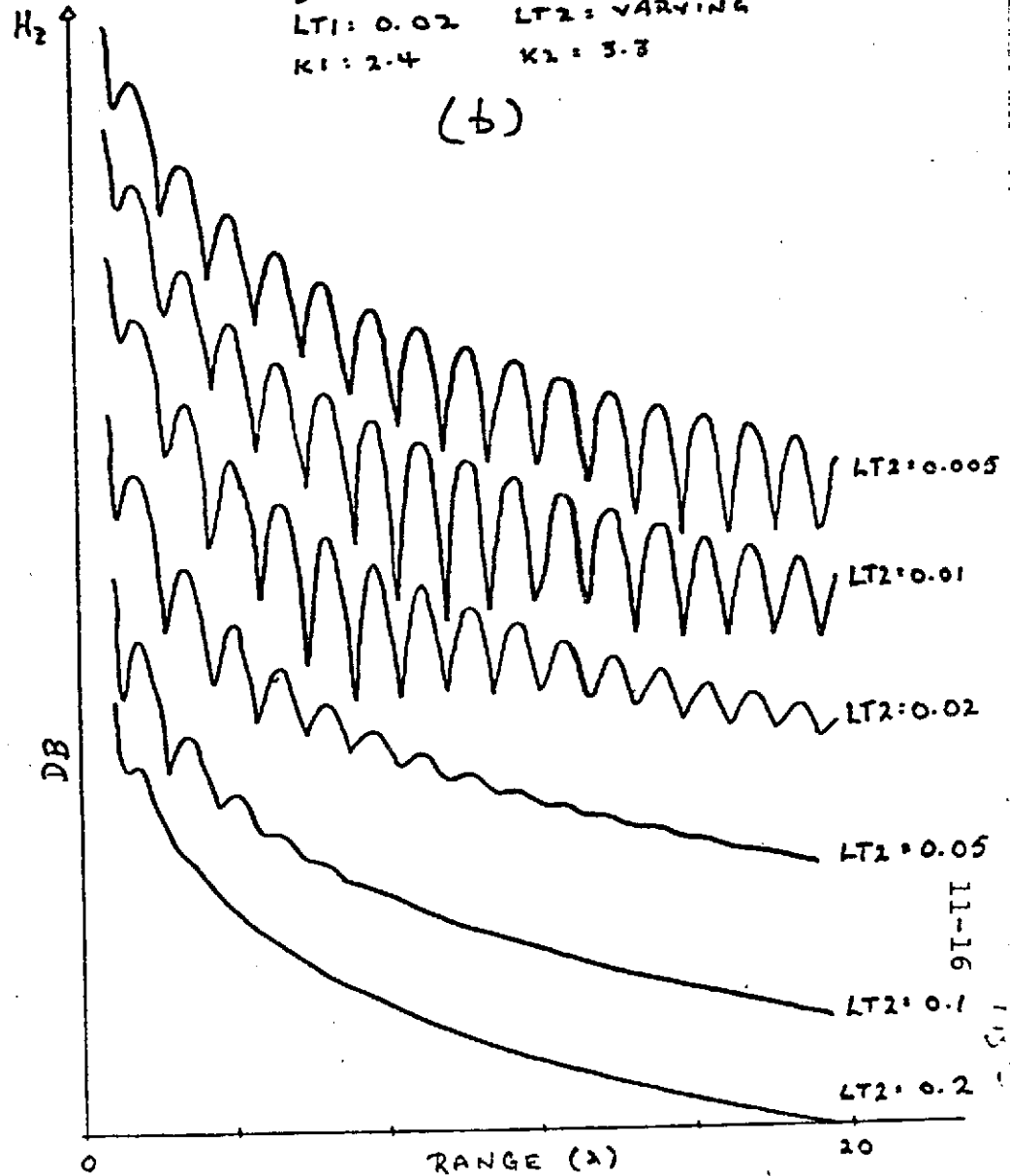
ORIGINAL PAGE IS
OF POOR QUALITY

(a)



D: 0.05
LT1: 0.02 LT2: VARYING
K1: 2.4 K2: 3.3

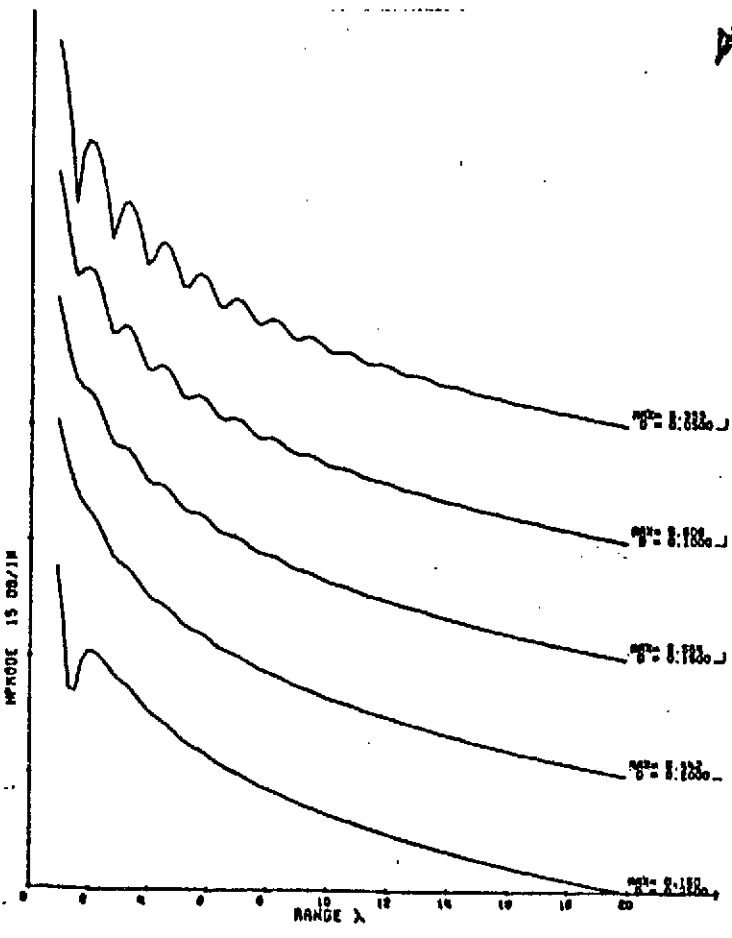
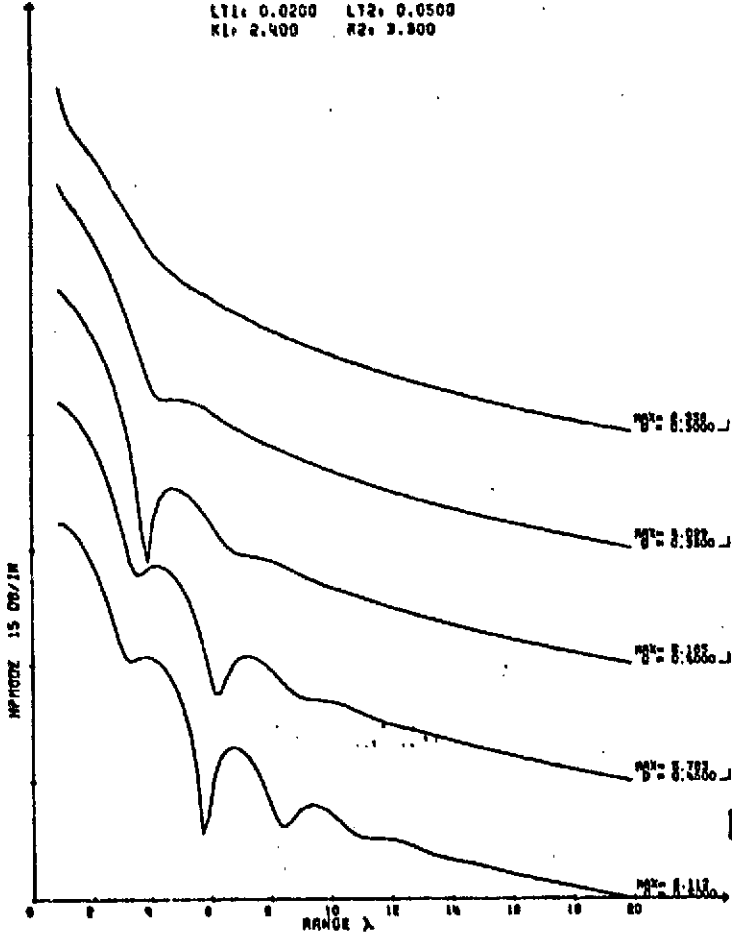
(b)



11-16

(a)

DEPTH: VARYING
LT1: 0.0200 LT2: 0.0500
K1: 2.400 K2: 3.300

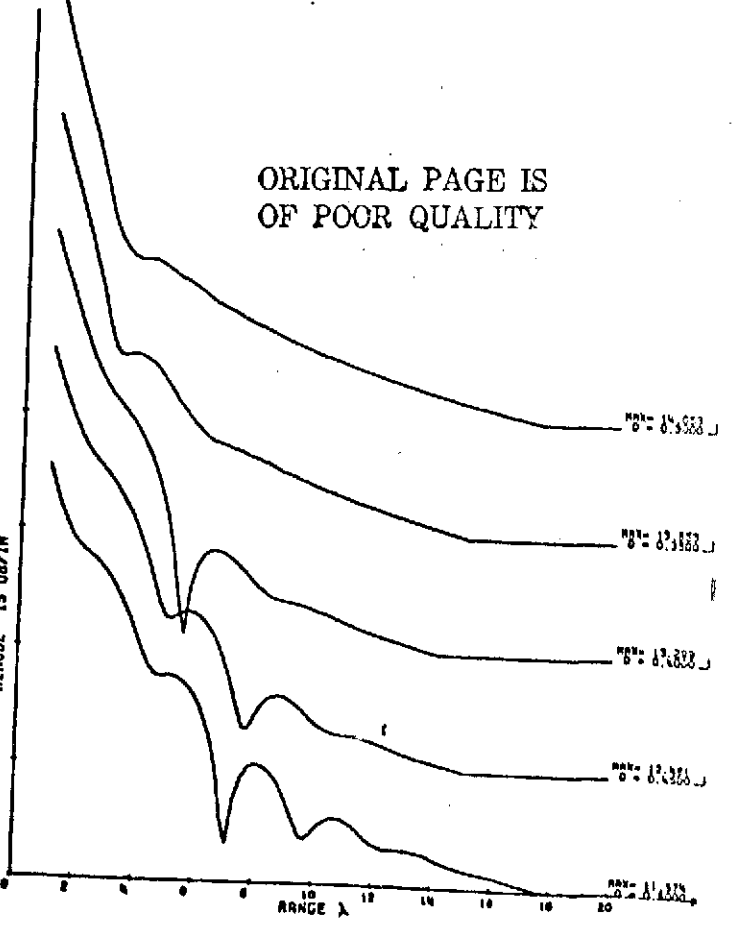
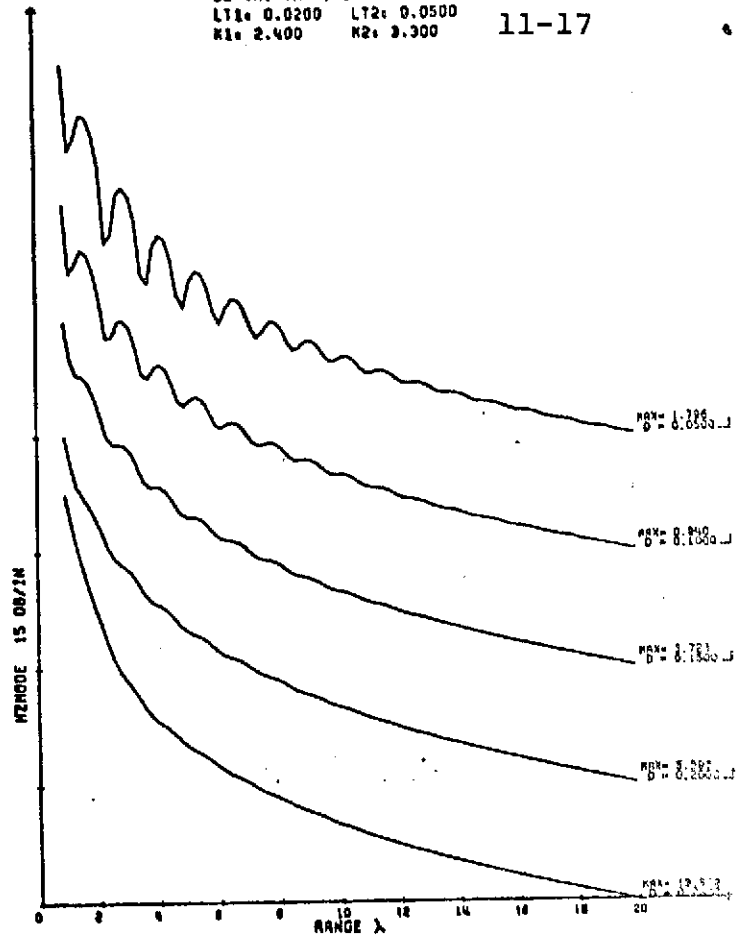


(b)

DEPTH: VARYING
LT1: 0.0200 LT2: 0.0500
K1: 2.400 K2: 3.300

Fig 4

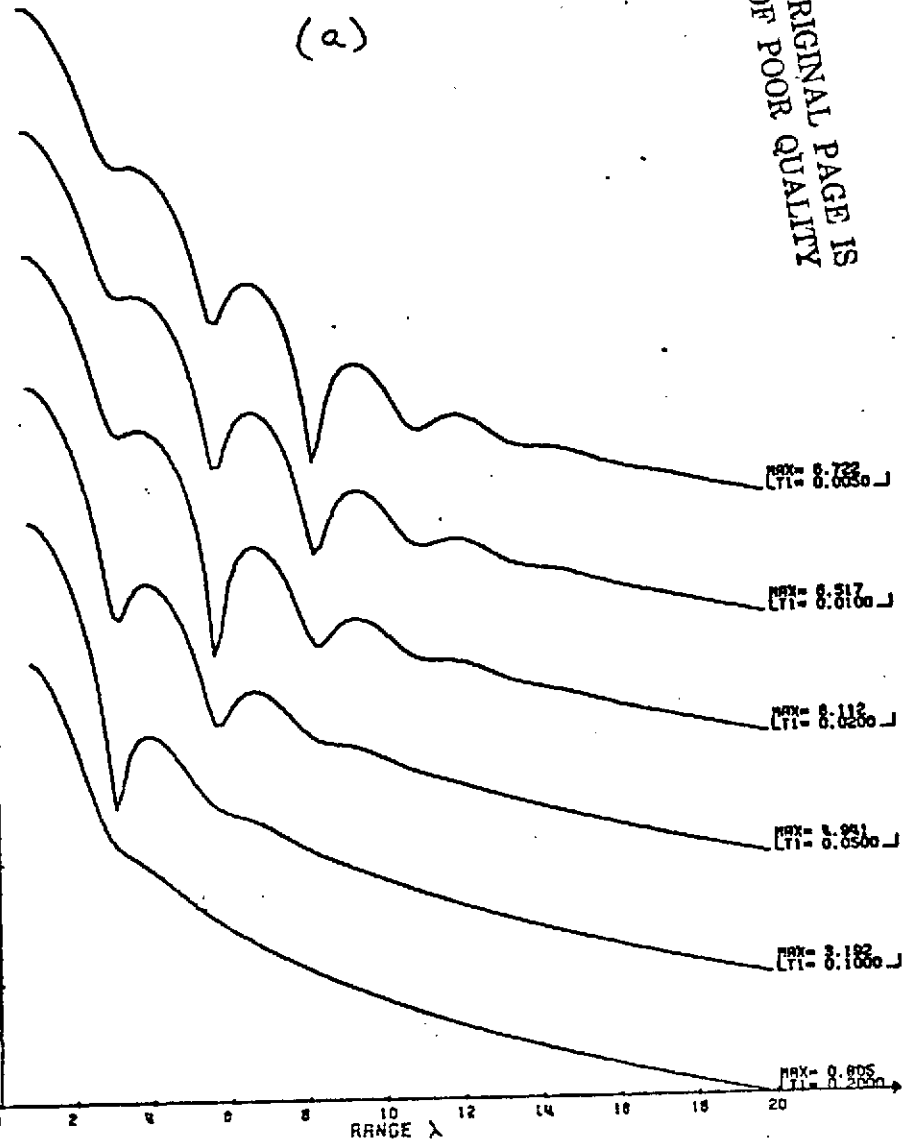
11-17



ORIGINAL PAGE IS
OF POOR QUALITY

DEPTH: 0.500λ
 LT1: VARYING LT2: 0.0500
 K1: 2.400 K2: 3.300

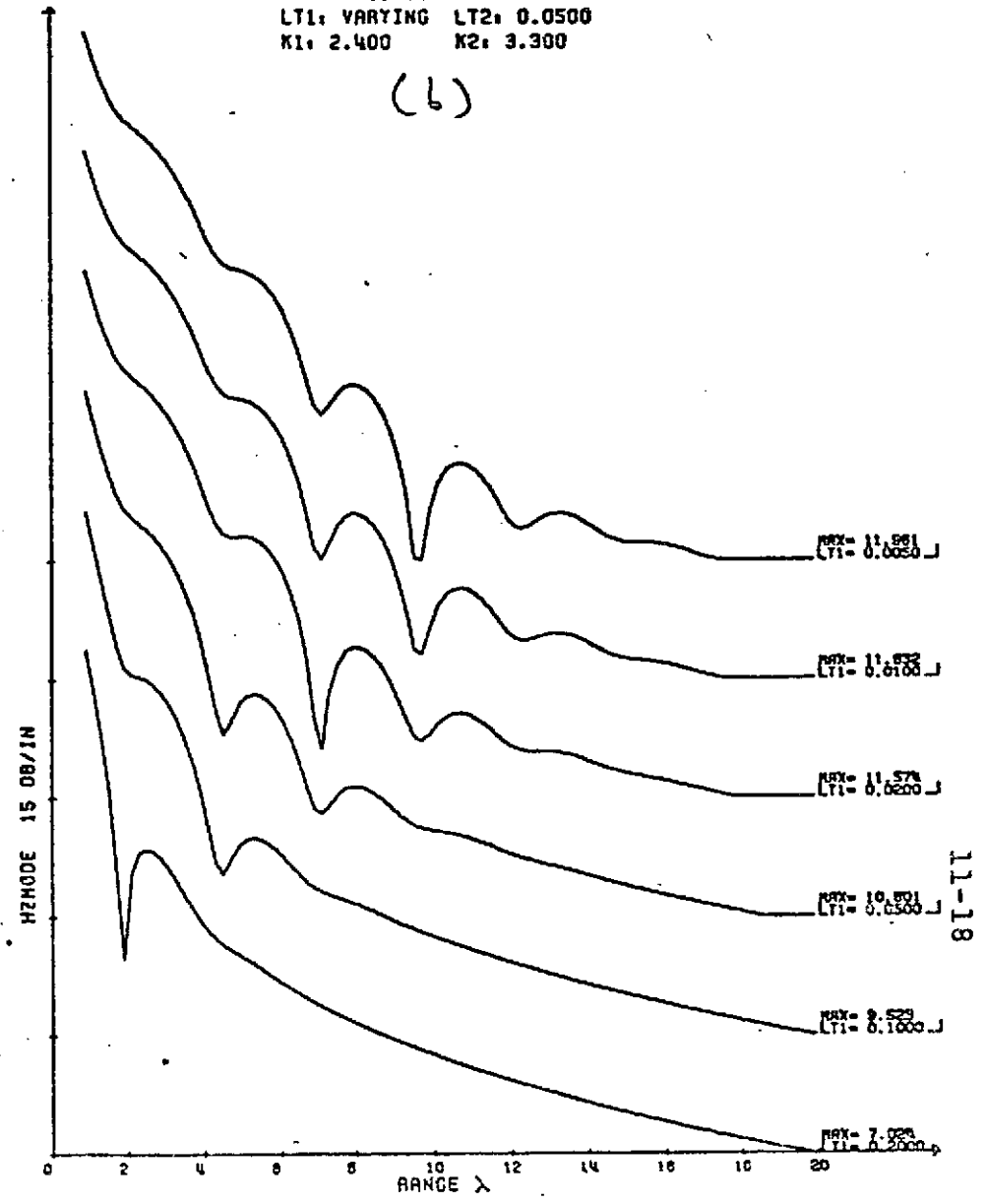
(a)



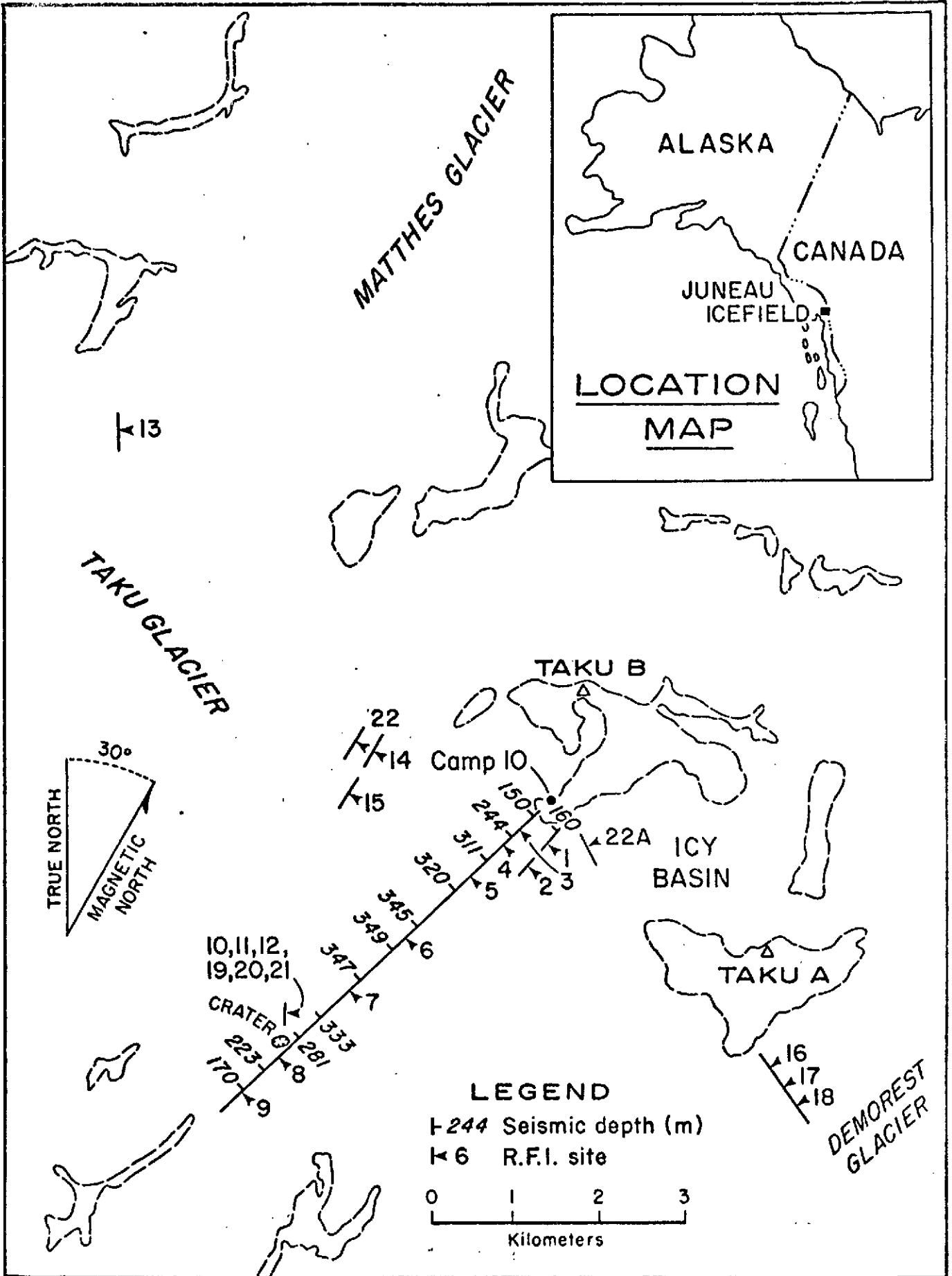
ORIGINAL PAGE IS
 OF POOR QUALITY

DEPTH: 0.500λ
 LT1: VARYING LT2: 0.0500
 K1: 2.400 K2: 3.300

(b)



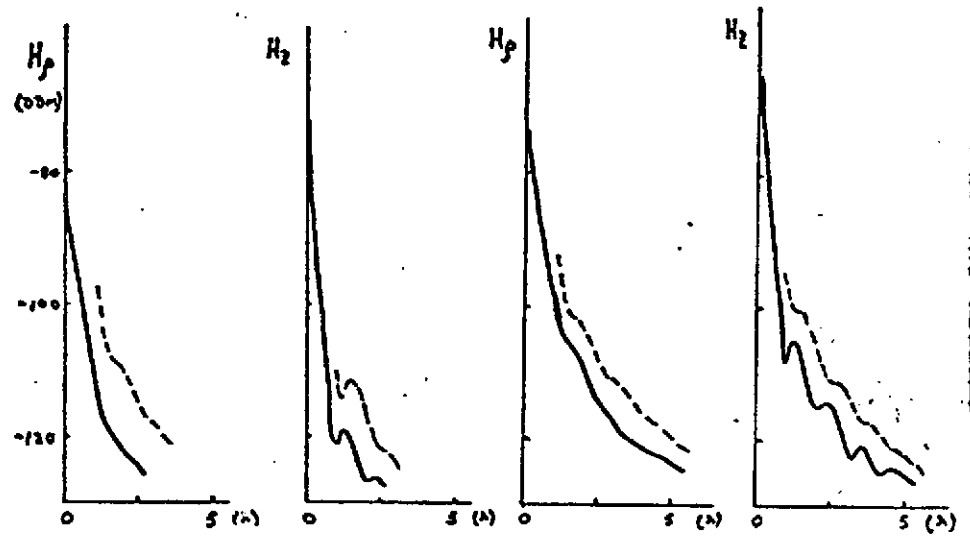
11-18



JUNGAU ICEFIELD - Run 36

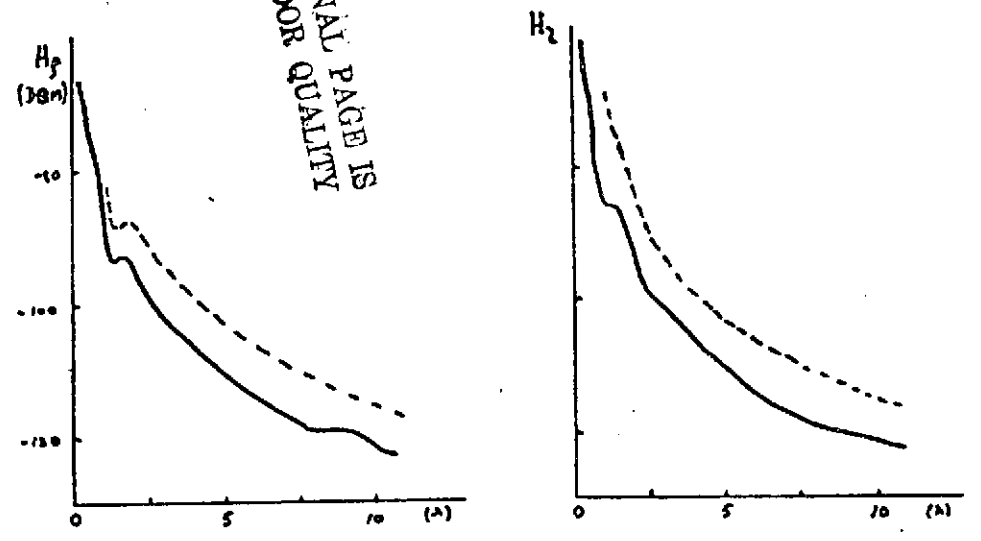
Fig 5

ORIGINAL PAGE IS
OF POOR
QUALITY

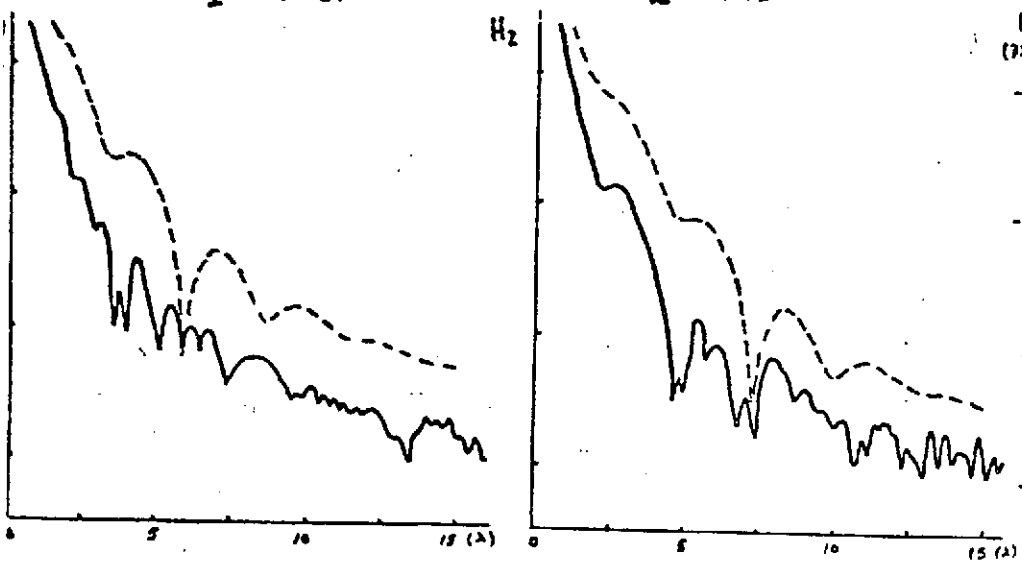


1 MHz.

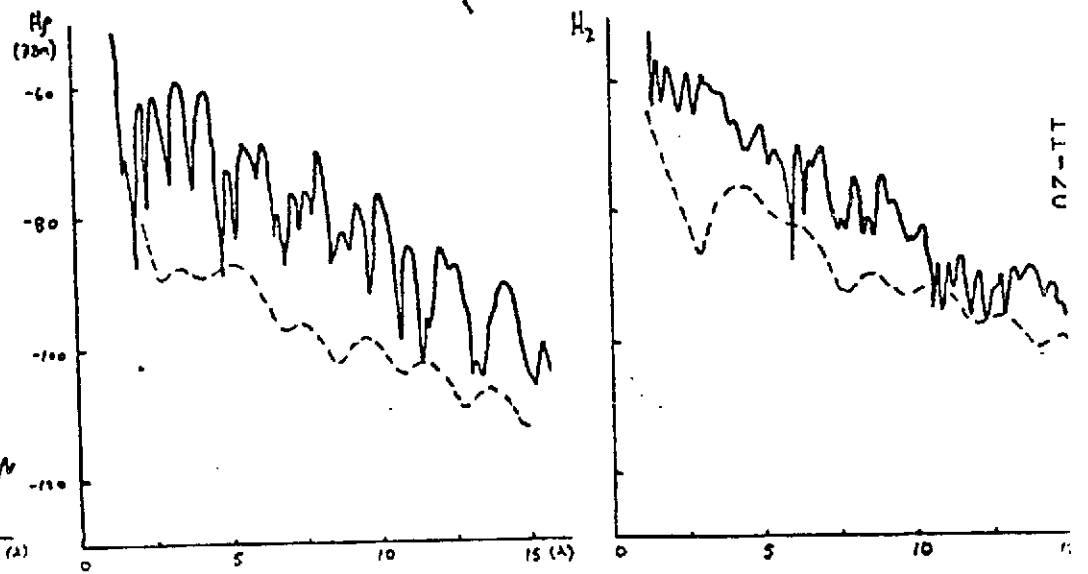
2 MHz



4 MHz



8 MHz

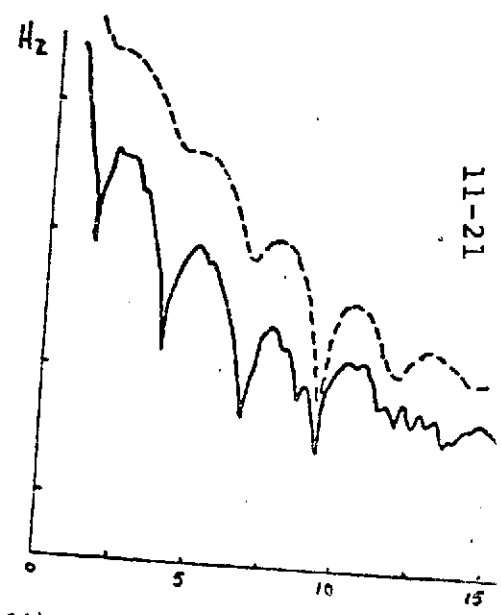
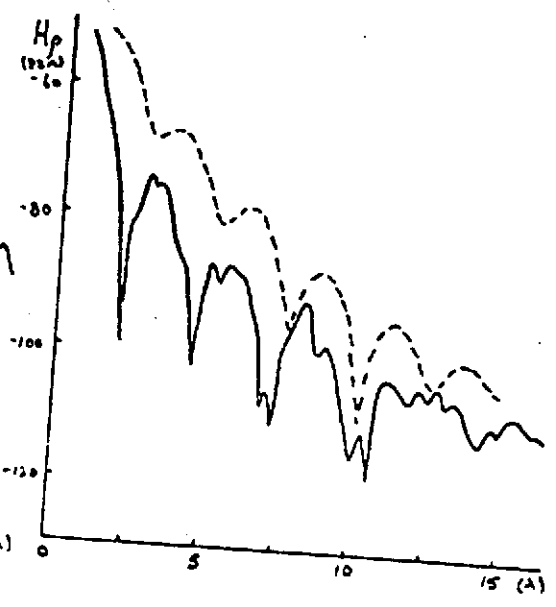
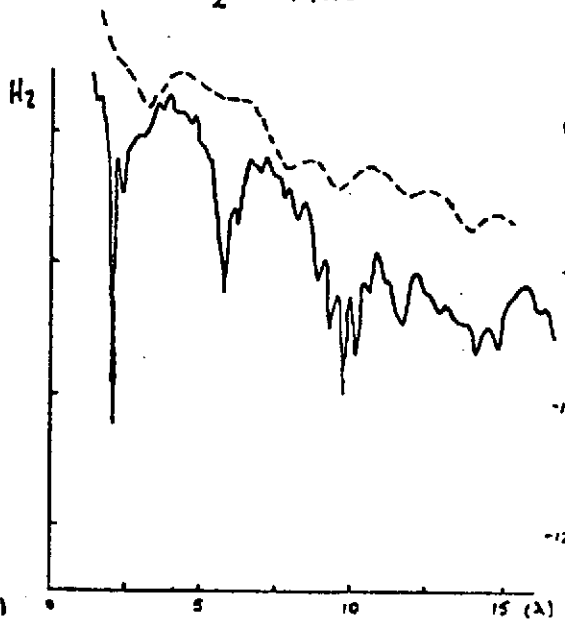
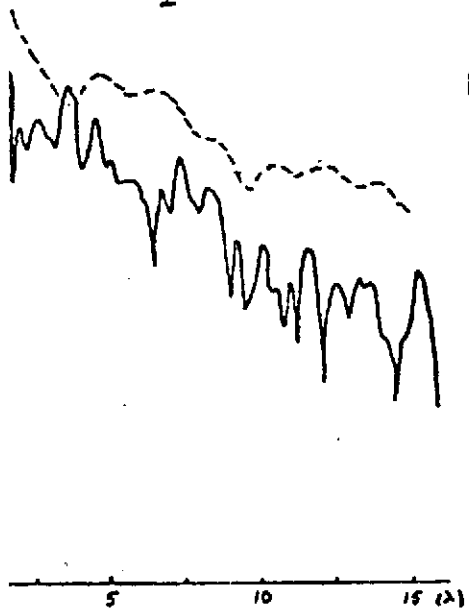
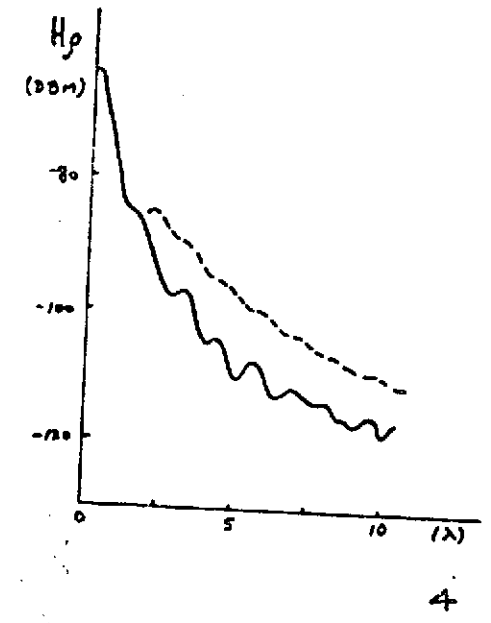
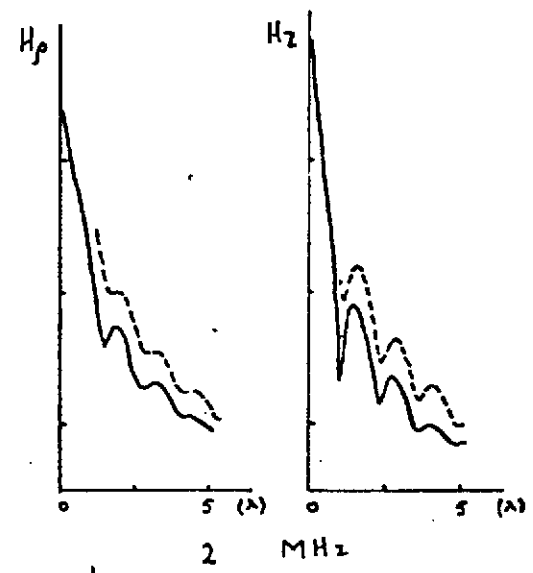
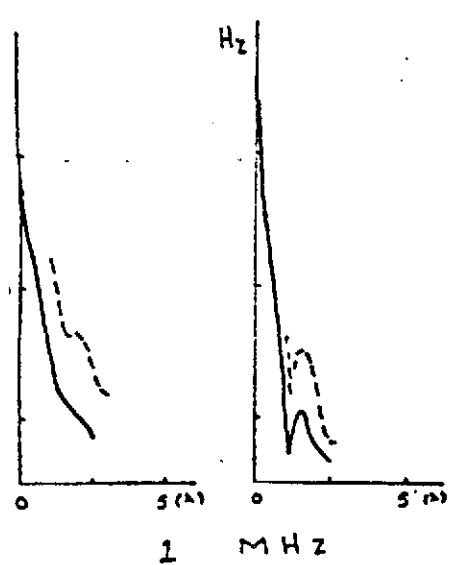


16 MHz

07-11

JUNEAU ICEFIELD 5 Run 092

Fig 7



11-21